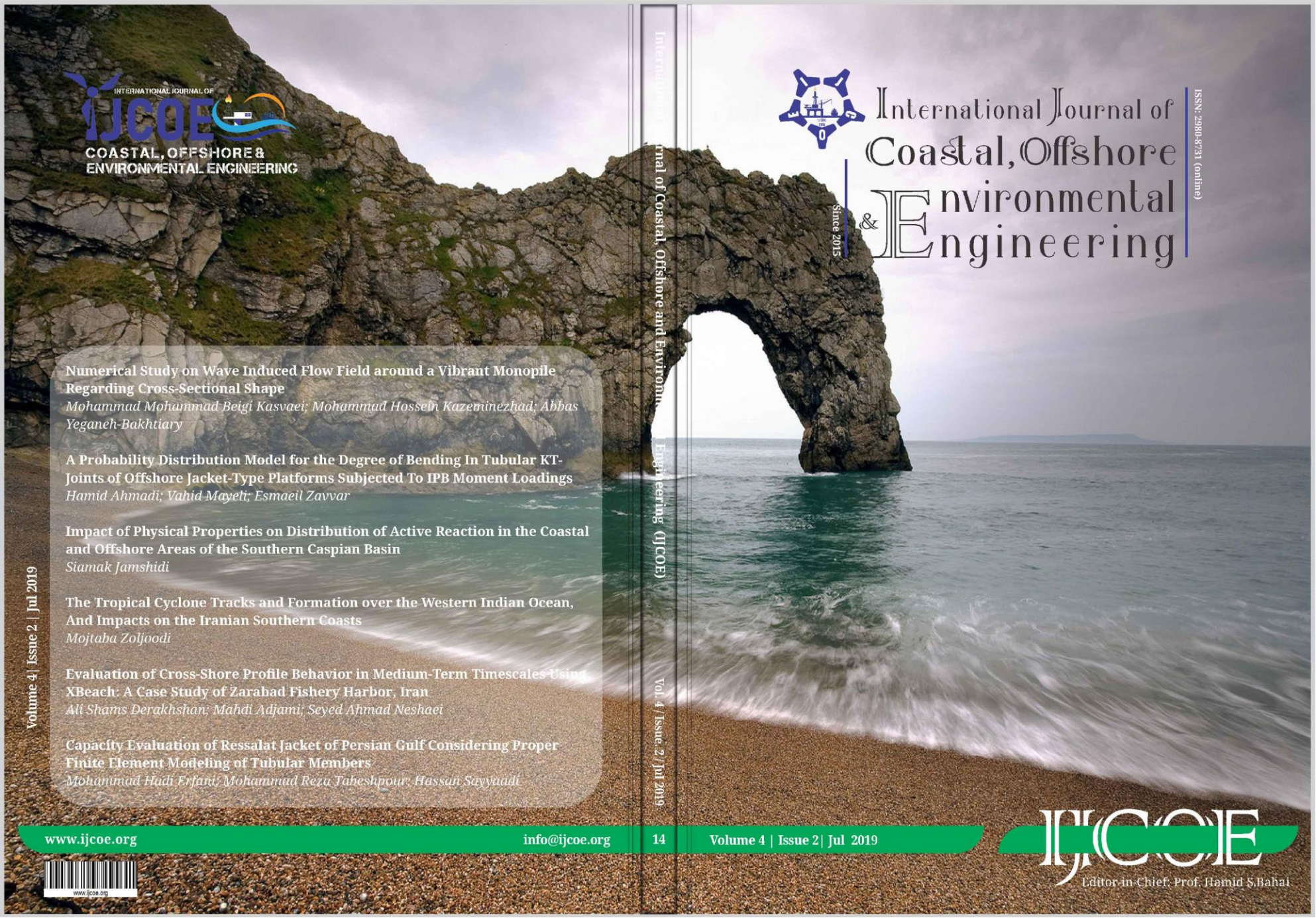

INTERNATIONAL JOURNAL OF
IJCOE
COASTAL, OFFSHORE & ENVIRONMENTAL ENGINEERING

Volume 4| Issue 2 | Jul 2019

www.ijcoe.org

International Journal of Coastal, Offshore and Environmental Engineering (IJCOE)

Vol. 4, Issue. 2, Jul 2019

Volume 4 | Issue 2| Jul 2019

International Journal of Coastal, Offshore & Environmental Engineering

ISSN: 2980-8731 (online)

Since 2015

IJCOE

International Journal of Coastal, Offshore & Environmental Engineering
Since 2015
ISSN: 2980-8721 (online)

In The Name of God

Message from the Editor-in-Chief

The IJCOE journal office was established in 2015,and its first issue was published in 2016. TheIJCOE covers a wide range of research in thefields of oceanography & ocean technology, aswell as marine industries & marine engineering.The editorial board of IJCOE consists of nearly130 of the greatest scientists and researchersfrom over 30 countries worldwide, and thejournal's review board comprises 1,000 membersfrom all five continents. The membership andapplication process for joining the editorial andreview boards of this journal is ongoing. IJCOE isa research-academic quarterly journal that haspublication and distribution permissions fromthe Press Organization and permission topublish scientific-research articles from theMinistry of Science, Research, and Technology(MSRT) with an "A" rating. It also holds a "Q1"rating from the ISC institute with an impactfactor (IF) of approximately 0.43 and isconsidered a "core journal" (prestigious andoutstanding journal). IJCOE is an open-accessjournal and allows the download and receipt ofaccepted articles in full text for free. It respectsand adheres to copyright and COPE regulations.The journal's office operates 24/7, providingservices to researchers. In addition to publishinga regular quarterly journal, IJCOE has 16 specialissues on specific topics in preparation. It alsoprovides conditions for publishing specializedbooks, references, and handbooks. Moreover, itis ready to cooperate with the secretariats ofreputable international conferences to publishtheir selected and outstanding articles. IJCOEevaluates, appraises, and publishes books,articles, and the scientific achievements andfindings of esteemed researchers and scientistsworldwide who are innovating and conductingin-depth research in the "important and strategicfield of the maritime technology & Oceanengineering." It welcomes any form of jointcooperation with universities, research institutes,and related research centers at the national,regional, and international levels, and extends ahand for collaboration.

Classification of Editorial Board in IJCOE

Editor-in-Chief

Director-in-Chief

Deputy Editor

Executive Managers

English Text Editor

Technical Editor

International Editorial Board

National Editorial Board

Editorial Board Associate

Editorial Board Assistant

Guest Editorial Board

Advisory Board

Administrative Coordinator

Honorary Board Member

Methodology Advisor

Author Benefits

- Open Access
- Rapid Publication
- Thorough Peer-Review
- No Copyright Constraints
- Coverage by Leading Indexing Services
- Discounts On Article Processing Charges (APC)
- No Space Constraints, No restriction on the maximum length of the papers, number of figures or colors

INTERNATIONAL JOURNAL OF IJCOE COASTAL, OFFSHORE & ENVIRONMENTAL ENGINEERING

Aims of IJCOE

Hydrodynamics

Marine equipment

Structural mechanics

Ocean environmental predictions

Stochastic calculations Experimental

Automatic Control of Marine Systems

Scope of IJCOE

Marine Hazards

Ocean Acoustics

Naval Architecture

Ocean Engineering

Coastal Engineering

Marine Meteorology

Marine Earth Sciences

Underwater Technology

Marine Renewable Energy

Polar & Arctic Engineering

Marine Renewable Energy

Marine Geography & Geodesy

Marine Environmental Engineering

Automatic Control of Marine Systems

Hydro Physics & Physical Oceanography

Type of papers

- Case Studies
- Book Reviews
- Review Article
- Letters to the Editor
- Methodology Papers
- Editorials and Commentaries
- Response or Rejoinder Papers
- Perspective or Opinion Papers
- Conceptual or Theoretical Papers
- Meta-Analysis and Systematic Reviews
- Short Communications or Brief Reports
- Research Articles (Original Research Papers)

Scientific Research Journal

Ministry of Science, Research And Technology (MSRT)

Jurnal Ranking 2023: A

Ministry Of Science, Research And Technology (ISC)

Citation Impact 2022: 0.429

Quartile 2022 : Q1

Core Collection

IJCOE is a Member of

Cantact Us

Office 1 | Research Institute of Meteorology and Atmospheric Science

Address | Tehran, Shahid Kharrazi Highway, Pajoohesh Blvd, Research Institute of Meteorology and Atmospheric Science, Sand and Dust Storm International Research Center (SDS-IRC), No. 13, 1st floor.

Phone | +982144787652

Postal code | 13611-14977

website | www.rimac.ac.ir

Office 2 | Iranian National Institute for Oceanography and Atmospheric Science

Address | Tehran, Dr. Fatemi Gharbi St., Shahid Etemadzade St., No. 3, third floor.

Phone | +982166944873

Postal code | 13389 – 14118

website | www.inio.ac.ir

Email | Info@ijcoe.org

Website | www.ijcoe.org

Follow Us

www.ijcoe.org

INTERNATIONAL JOURNAL OF IJCOE COASTAL, OFFSHORE & ENVIRONMENTAL ENGINEERING

Volume & Issue:

Volume 4, Issue 2, July 2019

Number of Articles: 6

Content

INTERNATIONAL JOURNAL OF
COASTAL & OFFSHORE ENGINEERING
IJCOE Vol.4/No. 2/Summer 2019 (1-9)

Available online at: http://ijcoe.org/browse.php?a_code=A-10-89-2&sid=1&slc_lang=en

Numerical Study on Wave Induced Flow Field around a Vibrant Monopile Regarding Cross-Sectional Shape

Mohammad Mohammad Beigi Kasvaei[1], Mohammad Hossein Kazeminezhad[2*], Abbas Yeganeh-Bakhtiary[3]

[1] *PhD Candidate, Iranian National Institute for Oceanography & Atmospheric Science, Tehran, Iran; mmbeigi@inio.ac.ir*
[2*] *Corresponding Author: Assistant Professor, Iranian National Institute for Oceanography & Atmospheric Science, Tehran, Iran; mkazeminezhad@inio.ac.ir*
[3] *Associate Professor, School of Civil Engineering, IUST, Tehran, Iran; yeganeh@iust.ac.ir*

ARTICLE INFO

Article History:
Received: 8 Jul. 2019
Accepted: 24 Aug. 2019

Keywords:
OpenFOAM®
RANS Equations
Vortex Induced Vibration (VIV)
Lock-in
Mesh deformation

ABSTRACT

A three-dimensional numerical simulation of regular waves passing over a monopile with square and circular cross-sectional shape was carried out to investigate flow field and vortex induced vibration. The rectangular wave flume and monopile are modeled with a solver; available in the open-source CFD toolkit OpenFOAM®. This solver applies the Reynolds-Averaged Navier-Stokes (RANS) equations with the volume of fluid technic (VOF) for tracking free surface. The motion equation together with mesh deformation was applied to capture monopile displacement. To validate the numerical model, results were compared to experimental data, and an admissible agreement was seen.

Computations were conducted for four cases with two different wave characteristics and different Keulegan-Carpenter (KC) numbers for square and circular cross-sectional shape. Vorticity field and *Q* criterion around the square and circular pile were depicted. It was seen that when KC increased, the difference in vortices around the square and the circular pile was more distinct. Investigations continued on transverse force coefficient and its oscillations. It was seen that by increasing KC, this coefficient and its frequency increased. When KC=20, the lift coefficient is larger for square pile compared to the circular pile. For both square and circular cross-sectional shape, the number of pile oscillation increased by increasing KC number. Also, the Strouhal number and vortex shedding frequency were larger for the circular pile compared to that of the square pile in vortex shedding regime. However, cross-flow vibration frequencies of the square and circular pile were close together.

1. Introduction

Wind turbines are nowadays one of the most used offshore structures in renewable energy equipment. A significant part of the wind turbine design process is related to its foundation design. A large number of marine structures such as offshore wind turbine are supported by a monopile foundation. Because of the presence of the pile, the wave-induced flow field around the pile changes and some vortices are generated. Dynamics of vortices depends on the cross-sectional shape of the pile and also on the wave characteristics, which can be stated by Keulegan-Carpenter number (KC):

$$\mathrm{KC} = \frac{U_m T}{D} \tag{1}$$

where the U_m is the maximum of the wave orbital velocity, T is the wave period, and D is the pile equivalent diameter. In addition to KC number, the cross-sectional shape of the pile influences on vortices pattern and its magnitude. Moreover, oscillating forces act on the pile due to the generated vortices around it when a pile is subjected to ocean waves. Elastically mounted pile subjected to the oscillating forces leads to so-called vortex induced vibration (VIV) of the pile. This vibration may lead to

increasing the fatigue loads and that is why it has been constantly considered in wave pile interaction issues.

A wide range of studies has been carried out in wave-pile interaction in a stationary or dynamic state of the pile. Sarpkaya and Rajabi [1], Zedan et al. [2], Angrilli and Cossalter [3], Bearman [4], Griffin [5], And Blevins [6] investigated extensively on the interaction of steady current and wave with pile during recent decades. Sumer and Fredsoe [7] carried out vast experimental studies of flow passing over vertical cylinders as well as wave-induced vortex shedding around the vertical pile. They used a range of different KC number to investigate its influence on different parameters around the pile such as vortices or force coefficients. Downes and Rockwell [8] studied the vibration of cylinders in wave experimentally. Many numerical studies on this subject have been implemented in recent years as well. Mo et al. [9], Jacobson et al. [10] and kasvaei et al. [11] simulated wave and a stationary pile interaction. Lou et al. [12] carried out a numerical study on vortex induced vibration of a marine riser. Zhao and Cheng [13] conducted a numerical investigation on vortex induced vibration of a circular cylinder of finite length subjected to uniform steady currents. Short literature review revealed that many studies have been conducted on VIV. Most of them, however, were about too slender cylindrical members such as marine risers. Also KC number, as an influencing parameter in wave-pile interaction problems, has not been purposefully considered.

The main aim of this paper is to investigate cross-sectional shape and KC number impact on the flow field around a vibrant monopile and on its dynamic response. Due to that, simulation of non-breaking regular waves passed over the vibrant monopile is carried out. Simulations have been performed for two different KC numbers to consider varying vortex shedding regimes.

The robust open source CFD code of OpenFOAM® with a multiphase, Eulerian solver (interDyMFoam) is applied. Mesh deformation is a capability of the solver to consider the pile displacement during vibration. Governing equations of the flow field and pile displacement are solved by finite volume discretization schemes in the code. Dynamics of vortex around the pile and vortex-induced vibration of the pile is investigated objectively regarding the influence of cross-sectional shape and KC number.

2. Numerical Model

2.1. Governing Equations

The incompressible fluid flow can be expressed by the 3D Reynolds averaged Navier-Stokes (RANS) equations with the continuity equation. These equations were used in the Cartesian coordinate system as the governing equations to find the flow field.

$$\frac{\partial U_i}{\partial t}+\frac{\partial\left(U_i U_j\right)}{\partial x_i} = -\frac{1}{\rho}\frac{\partial P}{\partial x_i}+\frac{\partial}{\partial x_i}\left[\frac{\mu_{eff}}{\rho}\left(\frac{\partial U_i}{\partial x_j}+\frac{\partial U_j}{\partial x_i}\right)\right]+g_i-\frac{\partial\left(\overline{u_i' u_j'}\right)}{\partial x_j} \quad (2)$$

$$\frac{\partial U_i}{\partial x_i}=0 \quad (3)$$

where U_i denotes the mean fluid velocity component in the i-th direction, P is the pressure, ρ is the fluid density, g_i denotes the acceleration of gravity, u' denotes the fluctuating velocity component, $\mu_{eff}=\mu+\mu_t$, μ is the molecular viscosity, and μ_t is the turbulent eddy viscosity.

To close the equations the Shear Stress Transport (SST) k-ω turbulence model was employed [14]. k as the turbulent kinetic energy with ω as the specific dissipation rate are expressed as:

$$\frac{\partial(\rho k)}{\partial t}+\frac{\partial\left(\rho U_j k\right)}{\partial x_j}=P_k-\beta^*\rho\omega k+\frac{\partial}{\partial x_j}\left[\left(\mu+\sigma_k\mu_t\right)\frac{\partial k}{\partial x_j}\right] \quad (4)$$

$$\frac{\partial(\rho\omega)}{\partial t}+\frac{\partial\left(\rho U_j\omega\right)}{\partial x_j}=\frac{\gamma}{\upsilon_t}P_k-\beta\rho\omega^2+\frac{\partial}{\partial x_j}\left[\left(\mu+\sigma_k\mu_t\right)\frac{\partial\omega}{\partial x_j}\right]+2\left(1-F_1\right)\frac{\rho\sigma_{\omega 2}}{\omega}\frac{\partial k}{\partial x_j}\frac{\partial\omega}{\partial x_j} \quad (5)$$

where F_1 is a harmonic function that is expressed as:

$$F_1=\tanh\left\{\min\left[\max\left(\frac{\sqrt{k}}{\beta^*\omega d},\frac{500\nu}{d^2\omega}\right),\frac{4\rho\sigma_{\omega 2}k}{CD_{k\omega}d^2}\right]\right\}^4 \quad (6)$$

$$CD_{k\omega}=\max\left(2\rho\sigma_{\omega 2}\frac{1}{\omega}\frac{\partial k}{\partial x_j}\frac{\partial\omega}{\partial\omega j},10^{-10}\right) \quad (7)$$

and $\nu_t=\mu_t/\rho$ is the turbulent kinematic viscosity, μ_t is computed as:

$$\mu_t=\frac{\rho a_1 k}{\max\left(a_{1\omega},\Omega F_2\right)} \quad (8)$$

$$F_2=\tanh\left[\max\left(2\frac{\sqrt{k}}{\beta^*\omega d},\frac{500\nu}{d^2\omega}\right)\right]^2 \quad (9)$$

where d is the distance between the field point and the nearest wall, and Ω is the vorticity magnitude.

Turbulence model constants are as following $\sigma_{k1} = 0.85034, \sigma_{k2} = 1.0, \sigma_{\omega 1} = 0.5, \sigma_{\omega 2} = 0.85616$, $\beta_1 = 0.075$, $\beta_2 = 0.0828$, $\beta^* = 0.09$, $a_1 = 0.31$, $\gamma_1 = 5/9$ and $\gamma_2 = 0.4403$ [15, 16].

Displacement of the pile is estimated by the equation of motion which is expressed as:

$$m\frac{d^2Z}{dt^2} + c\frac{dZ}{dt} + kZ = F_z \quad (10)$$

where Z is the displacement of the cylinder in cross-flow direction, F_z is the lift force on the cylinder, m, c and k are the mass, damping coefficient and the spring constant of the system, respectively. The added mass is taken into account when calculating the pile mass. Damping (c) and pile stiffness (k) are considered based on the study of Angrilli and Cossalter [3].

The free surface is traced by the VOF technique [17]. The Finite Volume Method was employed to solve the governing equations of the flow and transport equation for the volume fraction of water, in which the equations are integrated on the control volume and time.

2.2. Computational Domain and Boundary Conditions

To simulate the wave-pile interaction in a wave flume, the computational domain was a rectangular box which is occupied by water, air and the pile. The dimensions of the wave flume at the horizontal plane were 26.5 × 0.6 m and 0.8 m high so that free surface of the waves could easily pass through the flume without colliding with the ceiling. The diameter of both piles was 4 cm with square and circular cross-sectional shape. Figure 1 shows a schematic view of the wave flume with a circular pile as well as boundary conditions which were selected in the simulation. As seen, in the bed of the flume, the boundary condition is assumed to be no-slip as all components of the flow velocity are nil. The ceiling of the wave flume and its lateral walls (front and back in OpenFOAM modelling) are considered as the slip wall boundaries [10].

The wave inlet is to the left of the flume where regular waves are generated and propagated. At the outlet, a wave attenuation technique (relaxation zone) was applied that sufficiently prevented the reflection of the waves in the wave flume [16]. The pile was set 14 meters from the inlet boundary and the non-slip wall boundary condition was applied with a smooth hydraulic surface. The wave2Foam toolbox was applied to generate and propagate free surface water waves. Waves2Foam uses the VOF technique for free surface tracking [10]. It also prevents the reflection of waves in the flume by creating a relaxation zone (active sponge layers). This toolbox was created using the above in a multi-phase "InterDyMFoam" solver with dynamic mesh functionality. In this study, the pile is free to vibrate in the transverse direction of flow (cross-flow) and it was restrained from in-line vibration. To do so, the dynamic mesh was applied in the simulation.

Mesh generation in the computational domain was performed using the "blockMesh" tool. In this process, the computational domain was divided into 12 blocks and 476,800 hexagonal computing cells. As the pile and bed approached, smaller computational cells were applied to capable the model to account for the full impact of the wall boundary on the simulation. Numerical modelling was performed with different forms of meshing to obtain the optimum state. The results of the present model are not very sensitive to the form and dimensions of the computational cells. Figure 2 shows a view of the applied mesh for both circle and square cross-sectional shape pile.

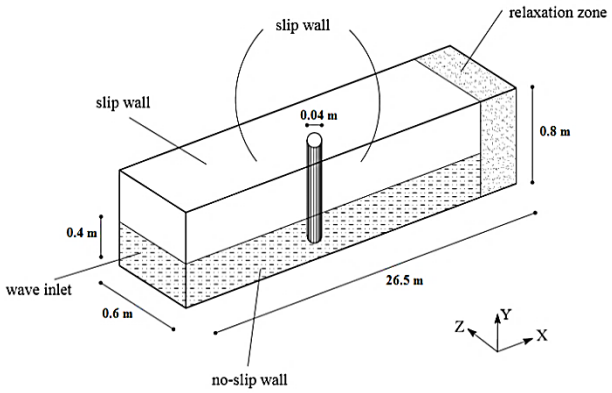

Figure 1. Computational domain and boundary conditions (not scale)

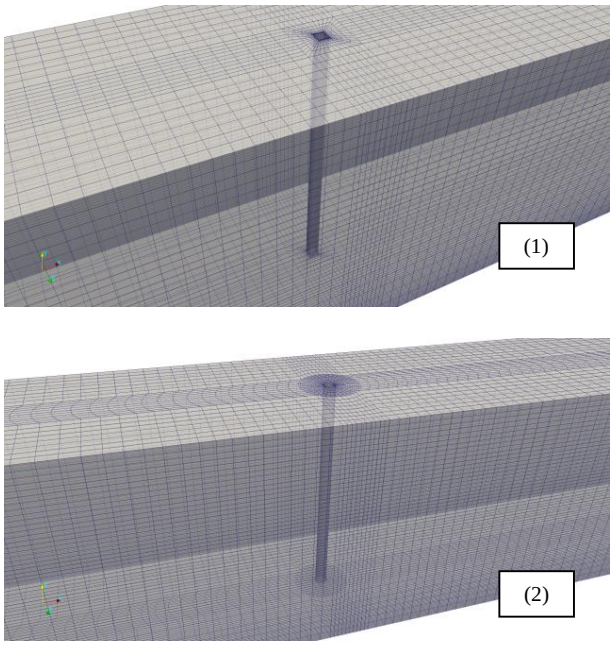

Figure 2. A view of the 3D applied mesh around the pile, (1) square cross-section, (2) circle cross-section

3. Model Validation

The numerical model validated by comparison of results against experimental data of Mo et al. [8]. These experiments conducted in the Large Wave Flume (GKW), with an effective length of 309 m and a width of 5 m, belonged to the Coastal Research Centre (FZK) in Hannover, Germany. A steel circular cylinder with a diameter of 70 cm was installed in 40 m away from the wave maker (left boundary). All the experimental conditions were numerically modelled but the wave flume length was considered equal to 77 m to reduce the computational costs. The experiment characteristics are shown in Table 1.

Table 1: The experiment characteristics

Wave Type	Water depth (*d*) [m]	Wave Height (*H*) [m]	Wave period (*T*) [sec]	KC Number [-]
Regular	4.76	1.20	4	6.13

The mesh generation was carried out by using the "blockMesh". The computational domain was discretized by eight-node hexahedron cells. Finer cells were used at the edge of the cylinder in order to simulate the large velocity gradients there. A total number of 433000 cells were used in computational domain. Boundary conditions were as they were in the section 2. Calculations were carried out for physical duration of 40 sec (10 waves passed over the pile), and then the outcomes were evaluated. Several model outcomes were compared to the experimental data to validate the numerical model.

The time history of the horizontal component of water particle velocity at points along the side wall of the flume along the pile at two different depths (y/d= -0.32 and y/d= -0.57, y is the distance from still water level and d is the water depth) have been plotted against the corresponding values measured in the experiment in Figure 3. As can be seen at both depths, there is an acceptable agreement between the model results and the experimental data.

Figure 4 shows the time history of the total in-line force applied to the pile against the corresponding experimental results. The force has been obtained from the sum of the pressure and viscous stresses on the wetted surface of the pile at each time step. As can be seen, there is an excellent agreement between the results of the simulation and those of the experiment. This means that the numerical model can predict well the hydrodynamic forces exerted on the pile.

The dynamic pressure was extracted at six points with different angles at a specific depth (y/d= -0.11) around the pile during the simulation and was plotted against the corresponding experimental data in Figure 5. The agreement between the experimental data and the numerical results for this case are extremely good. Given that the vortices generated around the pile affect the pressure field, by obtaining the correct values of the pressure field, it is expected that the numerical model can predict the vortex dynamics well.

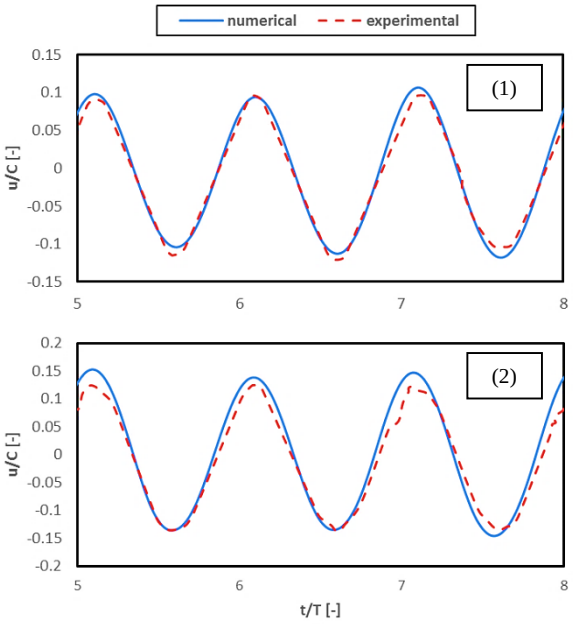

Figure 3. The horizontal component of water particle velocity at points along the side wall of the flume along the pile at two different depths (1) y/d= -0.57 (2) y/d= -0.32

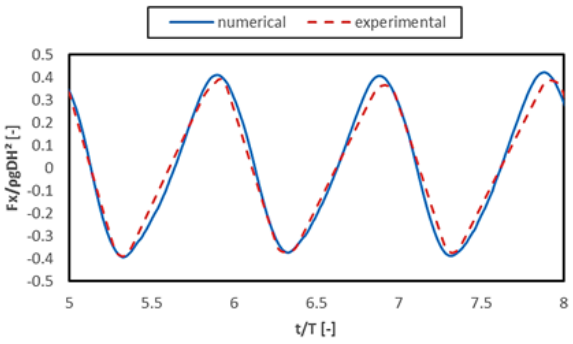

Figure 4. Time history of the total in-line force applied to the pile against the corresponding experimental results

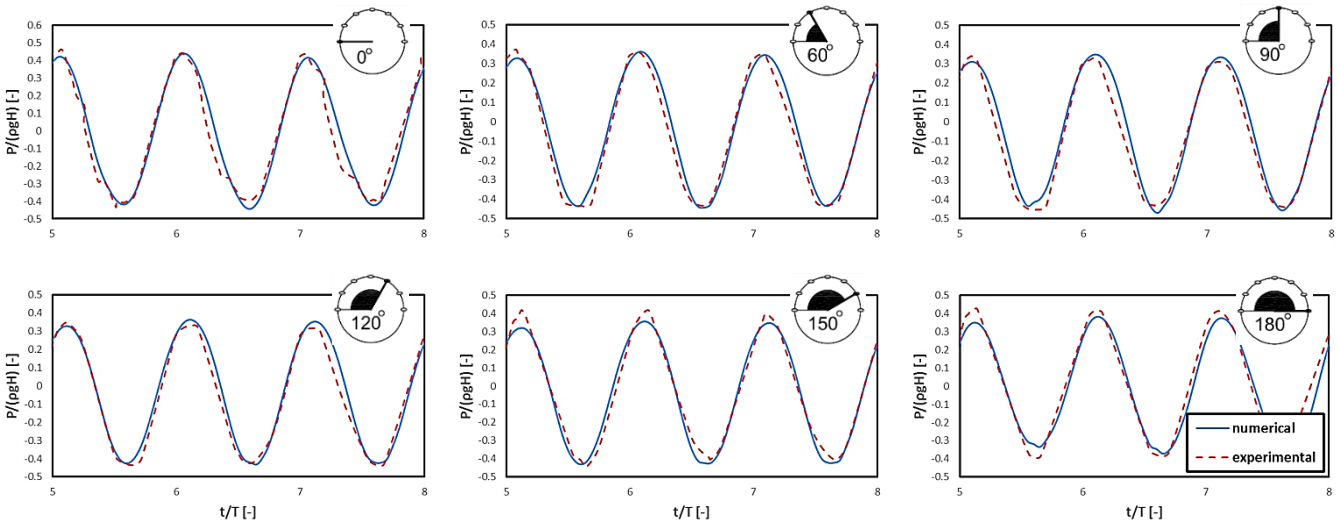

Figure 5. The dynamic pressure at six points with different angles at the depth of *y/d*= -0.11 around the pile

4. Results and Discussion

To investigate the impact of cross-sectional shape on vortex shedding and pile vibration, wave characteristics of two experimental studies [19, 20] were selected to consider varying vortex shedding regimes. Each wave characteristics was modelled with circular and square pile separately. In order to obtain the dynamic behavior of the pile, simulations were continued for the physical duration of 20 wave period. All aspects of numerical method including consistency, stability, convergence, accuracy and mesh dependency on the results were considered during the simulations.

Wave and pile characteristics which were applied in the numerical model are presented in Table 2. As seen, the pile and wave characteristics belong to KC=6.1 and KC=20.1 regimes. When KC=6.1 vortex shedding is in its early stage for the circular pile. In this regime, one vortex is shed in each half-period of the waves and the attached vortices are washed around the pile when the flow reverses. In the case of square pile no vortex shedding occurs when KC<11 [21]. For another case, when KC=20.1, vortex shedding is completely developed for both cross-sectional shapes. In this regime, two vortices are shed in each half-period of the waves. The attached vortices are washed around the pile when the flow reverses, in the same way as in the previous regimes [19].

Q criterion is a method that can be applied to investigate vortex shedding [22]. Figure 3 shows *Q* criterion for circular and square pile when KC=6.1. In the figure, wave-induced flow is from left to right which is called crest half period and ωt=90º. As seen, when KC=6.1 vortex shedding was in its early stage for circular pile but for the square pile only lee wake vortices were generated and no shedding occurred.

Table 2: Wave and pile characteristics applied in the numerical model

Pile Section *D*=4 [cm]	Water depth (*d*) [m]	Wave Height (*H*) [m]	Wave period (*T*) [sec]	KC Number [-]	Pile Reynolds Number [-]
D	0.4	0.023	4.4	6.1	2200
	0.4	0.126	2.6	20.1	12400
D	0.4	0.023	4.4	6.1	2200
	0.4	0.126	2.6	20.1	12400

Figure 4 and 5 show vorticity magnitude around circular and square pile when KC=6.1 and KC=20.1 respectively. The figure was depicted when pile is in the crest half period (ωt=90º). According to figure 4, some concentration in vorticity was seen in front of the sharp edges of the square pile. Also, the magnitude of vorticity was diminished over the side surfaces of the square pile between sharp edges. In circular Pile case, vorticity distribution was on the two lateral edges of the pile and also its magnitude was larger compared to that of the square pile.

As seen in figure 5 (when KC=20.1), vorticity pattern around the circular pile and square pile varies entirely. In square pile case, vorticity concentration in front of the sharp edges of the pile caused that vorticity magnitude and distribution of that would be quite different compared to those of the circular pile. Since the adverse pressure gradient generated in front of the square pile is larger than that generated in front of the circular pile. These results are in line with experimental observations [19].

Figure 6 illustrates the lift force coefficient (C_l) for square and circular pile when KC=20.1 and KC=6.1 during two wave periods. Lift force is acting on the pile in the transverse direction of flow and its coefficient is obtained by:

$$C_l = \frac{F_z}{0.5\rho U^2 D} \quad (11)$$

where ρ is the water density, U denotes the flow velocity and D is the pile diameter. F_z is the lift force which is predicted by integrating the pressure and viscous stresses in cross-flow direction along the pile in a discretized manner. The pressure and viscous forces from each cell face on the surface of the pile are summed to find the total pressure and viscous forces, respectively. As seen in Figure 6, when KC=20.1 for square pile lift coefficient was quite larger than that of the circular pile. Whereas, for KC=6.1 small difference of lift coefficient between square and the circular pile was seen which can be attributed to asymmetry in vortices around the pile. Consequently, the cross-sectional shape has an influence on the resulting force.

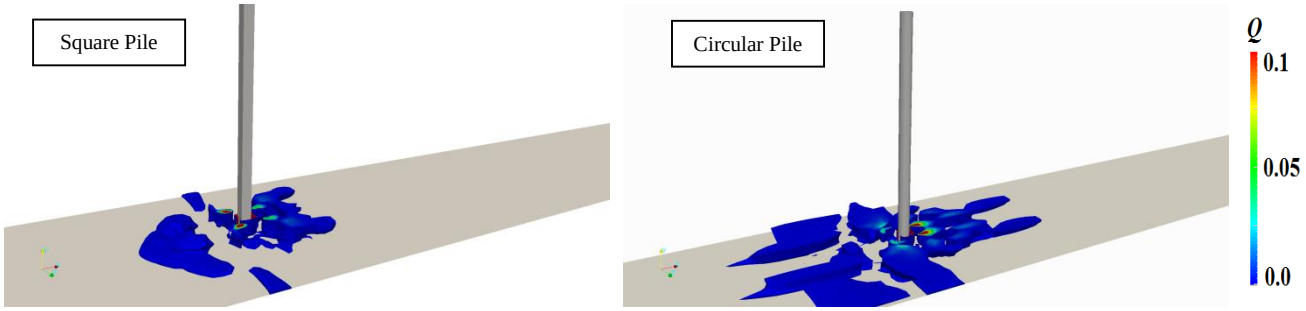

Figure 3. *Q* criterion around the square and circular pile in crest half period (ωt=90°) for KC=6.1

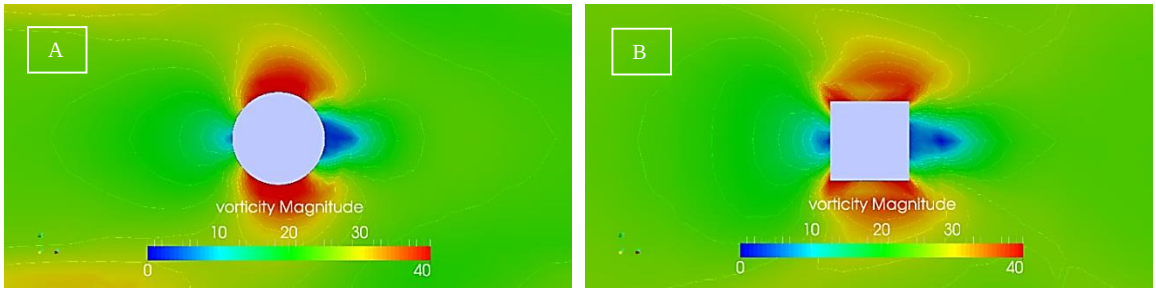

Figure 4. Vorticity magnitude contour around circular (a) and square (b) pile in crest half period (ωt=90°) for KC=6.1

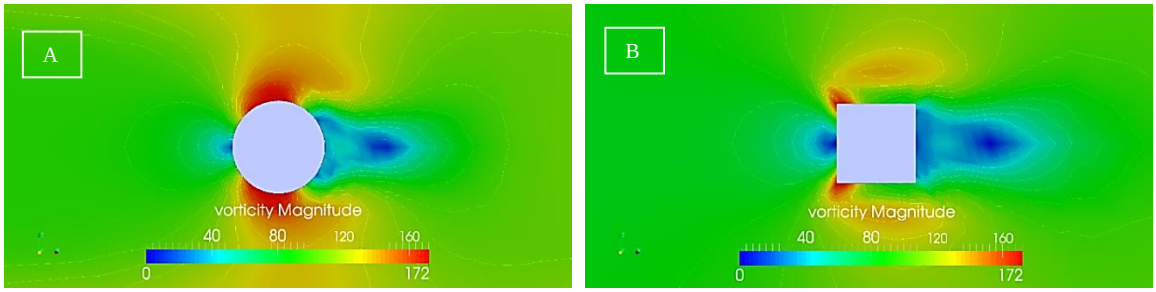

Figure 5. Vorticity magnitude contour around circular (a) and square (b) pile in crest half period (ωt=90°) for KC=6.1

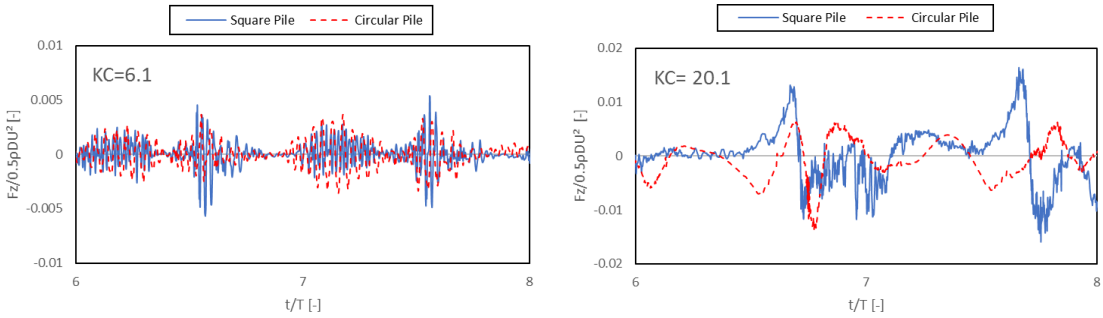

Figure 6. Time series of lift coefficient (c_l) for square and circular pile when KC=6.1 and KC=20 during two wave periods

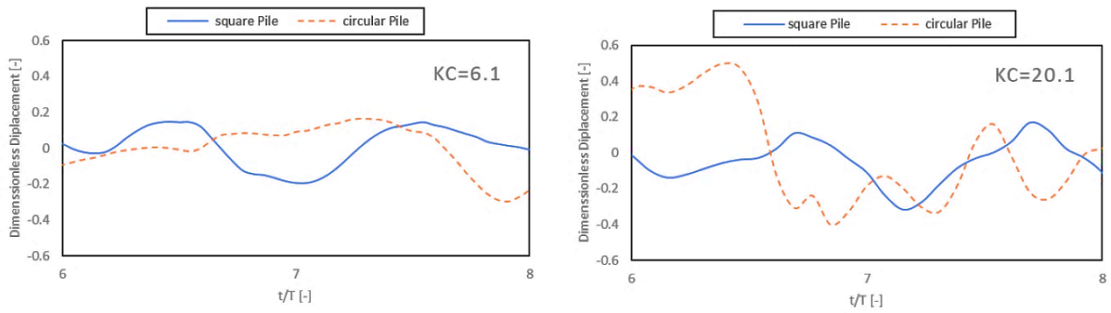

Figure 7. Time series of pile displacement for square and circular pile when KC=6.1 and KC=20 during two wave periods

The fluctuation of lift force can be attributed to the vortex shedding or asymmetry in vortices generated around the pile [7]. When KC=20.1 vortex shedding pattern is different between square and circular cross-section pile. Consequently, a phase difference was seen in the lift force between square and circular cross-section shapes. The difference in the lift coefficient between the square and the circular pile for each of the cases when KC=6.1 or KC=20.1 can be justified by the difference in vortex dynamics around the pile, which was explained above. In addition, the fluctuation of the lift coefficient differs between these two cross-sectional shapes. It was seen that when KC=20.1 lift force frequency of circular pile case is quite larger than that of square pile case. It must be noted that in this study the flow is due to wave which is a complicated flow field around the pile. In wave-induced flow around the pile, the lift force frequency is not the same as vortex shedding frequency [7].

Displacement of both pile during two wave periods for KC=6.1 and 20.1 is depicted in Figure 7. As seen, for both square and circular cross-section, the number of pile oscillation increased by increasing KC number. This may be due to that by increasing of KC number lift force frequency increases, causing the pile to oscillate [7]. In addition, the amplitude of pile oscillation increased by increasing KC number for both cross-sectional shapes. This can be the result of increasing the lift force magnitude by increasing the KC number.

Figure 8 shows power spectral density (PSD) from lift coefficient, which is obtained by Fourier transform of that, versus Strouhal number (St) for square and circular pile when KC=20. Strouhal number (St) is a dimensionless number describing oscillating flow mechanisms which is stated by the following equation:

$$\mathrm{St} = \frac{f_v D}{U} \tag{11}$$

where U is the fluid velocity, f_v is the vortex shedding frequency, and D is the pile diameter. The pick of PSD for square and circular pile denotes the Strouhal number. This method is applied to obtain vortex shedding frequency [21]. As seen from the figure, Strouhal numbers (St) are 0.19 and 0.2 for the square pile and circular pile, respectively. It was concluded that the frequency of the vortex shedding for circular pile was 1 percent larger than that of the square pile in this regime of KC. The frequency of the lift force can depend on the vortex shedding frequency (f_v). Therefore, it can be expected that the vortex shedding frequency in the circular pile case should be larger compared to the square pile case.

In this study pile is free to vibrate in the transverse direction of flow; hence, vortex-induced vibration (VIV) of the pile is probable. In pile-structure problems, VIV has been always of great interest. In this condition, Reduced Velocity (V_r) would be important which is stated by the following equation:

$$\mathrm{V_r} = \frac{U}{f_m D} \tag{12}$$

where f_m is the Eigen frequency of the pile and other parameters are the same as mentioned above. When f_m is close to f_v, the lock-in or synchronization occurs, which means that $V_r \approx 1/\mathrm{St}$. In this case, the vortex shedding frequency becomes equal to the Eigen frequency of the pile. The vibration amplitude is the maximum, and the correlation between the excitation forces along the span increases dramatically [23].

Figure 9 and 10 illustrate power spectral density (PSD) of the pile displacement over the frequency of vibration when KC=20.1 and KC=6.1 respectively. In this case, the frequencies of vibration for square and circular pile were quite close together. According to figure 9 and 10, by calculating V_r of each case, it was concluded that none of the cases were in the lock-in region.

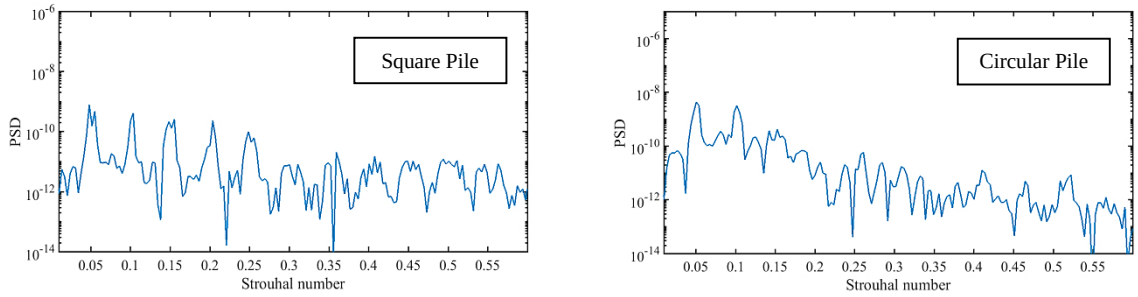

Figure 8. Power spectral density (PSD) of lift coefficient versus Strouhal number (St) for square and circular pile when KC=20.1

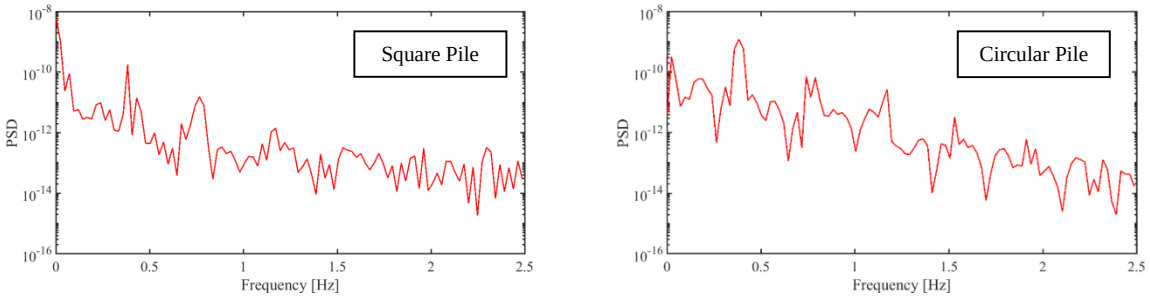

Figure 9. Power spectral density (PSD) of pile displacement over frequency for the square and circular pile when KC=20.1

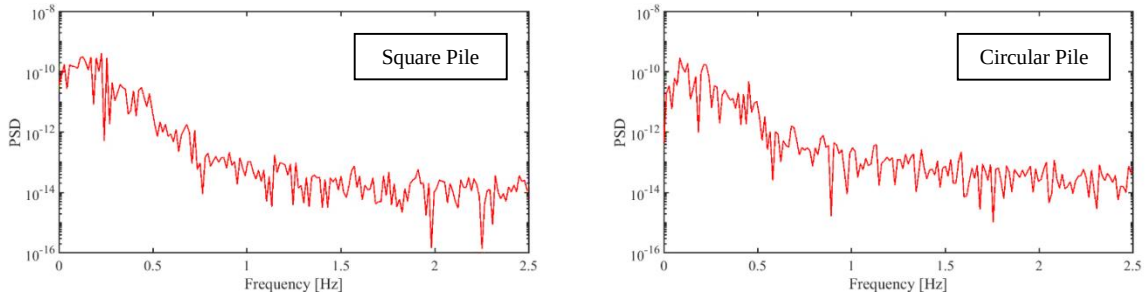

Figure 10. Power spectral density (PSD) of pile displacement over frequency for square and circular pile when KC=6.1

5. Conclusions

Three-dimensional numerical simulation of regular waves passing over a square and circular pile has been carried out in order to investigate vortex dynamics as well as vortex-induced vibration. OpenFOAM was employed as an open source tool of computational fluid dynamics (CFD) involving a solver capable of modeling the multi-phase Eulerian method for simulating rectangular wave flume and monopile. RANS equations to solve flow field together with motion equation to capture structure response were applied. The free surface was traced by the VOF method. Meshes are totally hexahedral and were created using the "blockMesh" utility. Mesh deformation was applied to capture the pile displacement due to cross-flow vibration.

Some numerical model results were compared to the experimental data to validate model e.g. the time history of the horizontal component of water particle velocity at at points along the side wall of the flume along the pile at two different depths, the time history of the total in-line force applied to the pile and the time history of the dynamic pressure at six points with different angles at a specific depth around the pile.

Computations were done for 4 cases with two numbers of Keulegan-Carpenter (KC) and two of the cross-sectional shape. Every model was run for the physical duration of 20 wave period to converge. Investigations were carried out on the vorticity, *Q* criterion and lift force coefficient and the following results were obtained:

- Vorticity magnitude around the pile was depicted and it was seen that when KC=6.1 concentration of vorticity was increased in sharp edges of the square pile.
- When KC=20.1 the vortex pattern was completely different between the square pile and the circular pile, which may be due to the difference of the adverse pressure gradient created against the square pile compared to the circular pile.
- When KC=20, the lift coefficient is larger for square pile compared to the circular pile. When KC=6.1 small difference of lift coefficient between square and the circular pile was seen.

- By observing the pile displacement it was seen that for both square and circular cross-sectional shape, the number of pile oscillation increased by increasing KC number.

From the Fourier transform and power spectral density (PSD) from lift force coefficient and pile displacement it was concluded that:

- Strouhal number for the circular pile was a bit larger and consequently, vortex shedding frequency was larger too compared to the square pile.
- Pile displacement over frequency was investigated and it was seen that when KC=20.1, vibration frequency of square and circular pile were close together.

8. References

1- Sarpkaya, T. and Rajabi, F. (1979), *Dynamic response of piles to vortex shedding in oscillating flows*, Offshore Technology Conference.

2- Zedan, M.F., Yeung, J.Y., Salane, H.J. and Fischer, F.J. (1981), *Dynamic response of a cantilever pile to vortex shedding in regular waves*, Journal of Energy Resources Technology, Vol. 103(1), p. 32-40.

3- Angrilli, F., Cossalter, V. (1982), *Transverse oscillations of a vertical pile in waves*, Journal of Fluids Engineering, Vol. 104(1), p. 46-52.

4- Bearman, P.W., 1984. *Vortex shedding from oscillating bluff bodies*, Annual review of fluid mechanics, Vol. 16(1), p. 195-222.

5- Griffin, O.M. (1985), *Vortex shedding from bluff bodies in a shear flow: a review*, Journal of Fluids Engineering, Vol. 107(3), p. 298-306.

6- Blevins, R.D. (1990), *Flow-induced vibration*. Van Nostrand Reinhold. New York, Vol. 199(0).

7- Sumer, B.M. (2006), *Hydrodynamics around cylindrical strucures* (Vol. 26), World Scientific.

8- Downes, K. and Rockwell, D. (2003), *Oscillations of a vertical elastically mounted cylinder in a wave: imaging of vortex patterns*, Journal of Fluids and Structures, Vol. 17(7), p. 1017-1033.

9- Mo, W., Irschik, K., Oumeraci, H. and Liu, P.L.F. (2007), *A 3D numerical model for computing non-breaking wave forces on slender piles*, Journal of Engineering Mathematics, Vol. 58(1-4), p. 19-30.

10- Jacobsen, N.G., Fuhrman, D.R. and Fredsøe, J. (2012), *A wave generation toolbox for the open-source CFD library: OpenFoam®*, International Journal for Numerical Methods in Fluids, Vol. 70(9), p. 1073-1088.

11- Kasvaei, M.M.B., Kazeminezhad, M.H. and Yeganeh-Bakhtiary, A. (2017), *Numerical Investigation on Wave Induced Vortex Dynamics Around Cylindrical Pile with Considering Varying Keulegan-Carpenter Number*, In ASME 2017 36th International Conference on Ocean, Offshore and Arctic Engineering (pp. V07AT06A059-V07AT06A059).American Society of Mechanical Engineers.

12- Lou, M., Dong, W. and Guo, H. (2011), *A vortex induced vibration of marine riser in waves*, Acta Oceanologica Sinica, Vol. 30(4), p. 96.

13- Zhao, M. and Cheng, L. (2014), *Vortex-induced vibration of a circular cylinder of finite length*, Physics of Fluids, Vol. 26(1), p. 015111.

14- Menter, F.R. (1994). *Two-equation eddy-viscosity turbulence models for engineering applications*, AIAA journal, Vol. 32(8), p. 1598-1605.

15- Wilcox, D.C. (1988), *Reassessment of the scale-determining equation for advanced turbulence models*, AIAA journal, Vol. 26(11), p. 1299-1310.

16- Amini Afshar, M. (2010), *Numerical wave generation in Open FOAM®*, PhD thesis, Chalmers University of Technology.

17- Hirt, C. W., & Nichols, B. D. (1981), *Volume of fluid (VOF) method for the dynamics of free boundaries*, Journal of computational physics, Vol.39(1), p. 201-225.

18- Mohammad Beigi Kasvaei, M., Kazeminezhad, M.H. and Yeganeh-Bakhtiary, A. (2018), *Numerical Study on Hydrodynamic Force and Wave Induced Vortex Dynamics around Cylindrical Pile*, International Journal of Coastal and Offshore Engineering, Vol.2(4), p. 1-11.

19- Sumer, B.M., Christiansen, N. and Fredsøe, J. (1997), *The horseshoe vortex and vortex shedding around a vertical wall-mounted cylinder exposed to waves*, Journal of Fluid Mechanics, Vol.332, p. 41-70.

20- Dey, S., Sumer, B.M. and Fredsøe, J. (2006), *Control of scour at vertical circular piles under waves and current*, Journal of Hydraulic Engineering, Vol. 132(3), p. 270-279.

21- Sumer, B. M., Christiansen, N., & Fredsøe, J. (1993), *Influence of cross section on wave scour around piles*, Journal of waterway, port, coastal, and ocean engineering, Vol.119(5), p. 477-495.

22- Chen, Q., Zhong, Q., Qi, M., and Wang, X. (2015), *Comparison of vortex identification criteria for planar velocity fields in wall turbulence*, Physics of Fluids, Vol. 27(8), p. 085101.

23- Le Cunff, C., Biolley, F., Fontaine, E., Etienne, S. and Facchinetti, M.L. (2002), *Vortex-induced vibrations of risers: theoretical, numerical and experimental investigation*, Oil & Gas Science and Technology, Vol. 57(1), p. 59-69.

INTERNATIONAL JOURNAL OF
COASTAL & OFFSHORE ENGINEERING
IJCOE Vol.4/No. 2/Summer 2019 (11-29)

Available online at: http://ijcoe.org/browse.php?a_code=A-10-72-2&sid=1&slc_lang=en

A Probability Distribution Model for the Degree of Bending In Tubular KT-Joints of Offshore Jacket-Type Platforms Subjected To IPB Moment Loadings

Hamid Ahmadi[1*], Vahid Mayeli[2], Esmaeil Zavvar[3]

[1] *Faculty of Civil Engineering, University of Tabriz; h-ahmadi@tabrizu.ac.ir*
[2] *Faculty of Civil Engineering, University of Tabriz; mayeli.vahid@gmail.com*
[3] *Faculty of Civil Engineering, University of Tabriz; esmaeilzavvar@gmail.com*

ARTICLE INFO

Article History:
Received: 5 Mar. 2019
Accepted: 1 Sep. 2019

Keywords:
Tubular KT-joint
Fatigue
Degree of bending (DoB),
Probability density function (PDF)
Kolmogorov-Smirnov test

ABSTRACT

The objective of present research was the derivation of probability density functions (PDFs) for the degree of bending (DoB) in tubular KT-joints commonly found in jacket-type platforms. A total of 243 finite element (FE) analyses were carried out on 81 FE models of KT-joints subjected to three types of in-plane bending (IPB) moment loading. Generated FE models were validated using experimental data, previous FE results, and available parametric equations. Based on the results of parametric FE study, a sample database was prepared for the DoB values and density histograms were generated for respective samples based on the Freedman-Diaconis rule. Thirteen theoretical PDFs were fitted to the developed histograms and the maximum likelihood (ML) method was applied to evaluate the parameters of fitted PDFs. In each case, the Kolmogorov-Smirnov test was used to evaluate the goodness of fit. Finally, the Generalized Extreme Value model was proposed as the governing probability distribution function for the DoB. After substituting the values of estimated parameters, nine fully defined PDFs were presented for the DoB at the crown, toe, and heel positions of the central and outer braces in tubular KT-joints subjected to three types of IPB moment loading.

1. Introduction

Circular hollow section members, also called tubulars, are the primary structural components of jacket-type offshore platforms widely used for the oil/gas production. The intersection among tubulars, in which the prepared ends of branch members (braces) are welded onto the undisturbed surface of a main member (chord), is called a tubular joint (Fig. 1). As a result of the formation and propagation of cracks due to wave induced cyclic loads, tubular joints are susceptible to fatigue-induced damage during their service life.

The stress-life (S-N) approach that is based on the hot-spot stress (HSS) calculation is widely used to estimate the fatigue life of a tubular joint. However, the study of a large number of fatigue test results have shown that tubular joints of different geometry or loading type but with similar HSSs often exhibit significantly different numbers of cycles to failure [1]. Such differences are thought to be attributable to changes in crack growth rate that is dependent on the through-the-thickness stress distribution which can be characterized by the degree of bending (DoB) defined as the ratio of bending stress to total external stress.

Typical stress distribution through the chord wall of a tubular joint is depicted in Fig. 2. Since for a deep crack, the weld-toe stress concentration has a relatively little effect on the through-the-thickness stress field [2], the stress distribution across the wall thickness is usually assumed to be a linear combination of membrane and bending stresses. Hence, the DoB can be expressed as:

$$\mathrm{DoB} = \frac{\sigma_B}{\sigma_T} = \frac{\sigma_B}{\sigma_B + \sigma_M} \tag{1}$$

where σ_T is the total stress; and σ_B and σ_M are the bending and membrane stress components, respectively.

The DoB value along the weld toe of a tubular joint, under any specific loading condition, is mainly determined by the joint geometry. To study the behavior of a tubular joint and to easily relate this behavior to the geometrical characteristics of the joint,

a set of dimensionless geometrical parameters has been defined. Fig. 1 depicts a tubular KT-joint with the geometrical parameters τ, γ, β, α, and α_B for chord and brace diameters: D and d, and their corresponding wall thicknesses: T and t, and lengths: L and l. Critical positions along the weld toe of central and outer braces for the calculation of the DoB values in a tubular joint, i.e. saddle, crown, toe, and heel have been shown in Fig. 1.

Since early 1990s, a number of research works has been devoted to the study of the DoB in simple tubular connections such as X- and K-joints. However, for tubular joints having more complex geometry such as KT-joints which are quite common in steel offshore structures, the DoB has not been comprehensively investigated.

Morgan and Lee [3] derived mean and design equations for DoB values at critical positions in axially loaded tubular K-joints. Design equations met all the acceptance criteria recommended by the UK DoE [4]. Chang and Dover [2] carried out a series of systematic thin-shell FE analyses for 330 tubular X- and DT-joints typically found in offshore structures under six different types of loading. A set of parametric equations was developed to calculate the DoB at critical positions. Lee and Bowness [5] proposed an engineering methodology for estimating stress intensity factor (SIF) solutions for semi-elliptical weld-toe cracks in tubular joints. The methodology uses the T-butt solutions proposed previously by the authors in conjunction with the stress concentration factors (SCFs) and the DoB values in uncracked tubular joints. Shen and Choo [6] determined the SIFs for a grouted tubular joint. They found that the fatigue strength of a grouted joint may be lower than that of as-welded joint, because when normalized with the HSS, the shape factor of grouted joint is higher than that of original as-welded joint due to the reduction in the DoB caused by the presence of in-filled grout in the chord. For grouted tubular joints, it is essential to consider the effect of the DoB in practical fatigue assessment using HSS approach. Ahmadi et al. [7] performed a set of parametric stress analyses on 81 K-joint FE models subjected to two different types of IPB loads. Analysis results were used to present general remarks on the effect of geometrical parameters on the DoB values at the toe and heel positions; and a new set of DoB parametric equations was developed. Ahmadi and Asoodeh [8] analyzed 81 K-joint FE models subjected to two types of out-of-plane bending (OPB) loading. Results were used to study the geometrical effects on the DoB at the saddle position; and two new DoB design formulas were proposed. Ahmadi and Asoodeh [9] studied the DoB in uniplanar tubular KT-joints of jacket structures subjected to axial loads. Their study was limited to the central brace DoB values and no design equation was proposed for the DoB along the weld toe of the outer braces. Also, IPB and OPB loadings were not included. Ahmadi and Amini Niaki [10] studied the degree of bending in two-planar tubular DT-joints under axial and bending loads. They developed a set of parametric equations to predict the DoB values at the saddle and crown positions.

In a deterministic fatigue analysis, limiting assumptions should be made on numerous input parameters some of which exhibit considerable scatter. Consequently, deterministic analyses usually result in conservative designs. This fact emphasizes the significance of reliability-based fatigue analysis and design methods in which the key parameters of the problem can be modeled as random variables. The fundamentals of fatigue reliability assessment, if properly applied, can provide immense insight into the fatigue performance and safety of the structural system. Regardless of the method used for the reliability-based fatigue analysis and design of offshore structures, the probabilistic and statistical measures of the DoB are required as input parameters. The DoB shows considerable scatter highlighting the significance of deriving its governing probability distribution function.

Ahmadi and Ghaffari [11] proposed a set of probability density functions for the DoB in tubular X-joints subjected to four types of bending loads including two types of IPB and two types of OPB moment loading. Ahmadi and Ghaffari [12] developed probability distribution models for the DoB and SIF values in axially-loaded tubular K-joints.

Based on the above discussion, it can be concluded that:

1. Despite the comprehensive research carried out on the study of SCFs and SIFs in tubular joints (e.g. [13-24] for SCFs, and [25, 26] for SIFs, among many others), the research works on the DoB in tubular joints are scarce and the studied joint types are limited to simple connections. Although tubular KT-joints are commonly found in steel offshore structures, the DoB in such joints has not been comprehensively investigated.
2. Results of research works reported in the literature are mostly suitable for deterministic analyses; and probabilistic studies are only limited to K- and X-joints. No probabilistic investigation has been carried out on the DoB of KT-joints; and there is no probability density function available for the DoB values to be used in reliability-based fatigue analysis and design of this type of joint.

In the present research, initially, available literature on the DoB was surveyed (Sect. 2). Afterwards, a total of 243 finite element (FE) analyses were carried out on 81 FE models of tubular KT-joints which are among the most common joint types in jacket-type oil/gas production platforms. FE analyses were conducted under three types of in-plane bending (IPB) loads as shown in Fig. 3. Generated FE models were validated

using the existing experimental data, FE results, and parametric equations. Based on a parametric FE investigation, a sample database was created for the DoB (Sect. 3); and density histograms were generated for respective samples (Sect. 4). Thirteen theoretical PDFs were fitted to the developed histograms and the maximum likelihood (ML) method was applied to evaluate the parameters of fitted PDFs (Sect. 5). In each case, the Kolmogorov-Smirnov test was used to assess the goodness of fit (Sect. 6). Finally, a probability distribution model was proposed for the DoB; and after substituting the values of estimated parameters, nine fully defined PDFs were presented for the DoB at the crown, toe, and heel positions of central and outer braces in tubular KT-joints subjected to three types of IPB moment loading (Sect. 7).

2. Preparation of the DoB sample database

2.1. FE modeling procedure

In the present research, FE-based software package ANSYS Ver. 11 was used for the FE modeling and analysis of tubular KT-joints subjected to IPB loadings in order to extract the DoB values for the probabilistic study. This section presents the details of FE modeling and analysis.

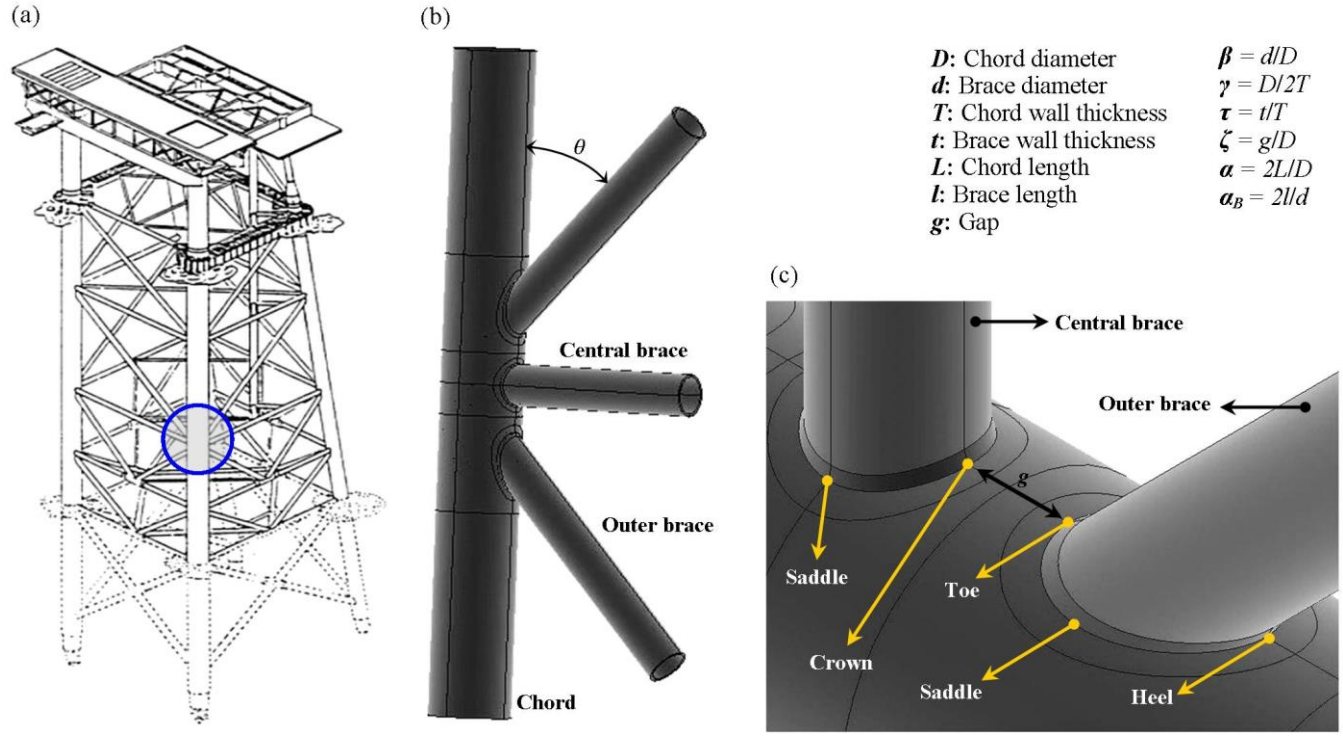

Fig. 1. (a) A tubular KT-joint in a typical offshore jacket structure, (b) Geometrical notation for a tubular KT-joint, (c) Critical positions along the weld toe of central and outer braces.

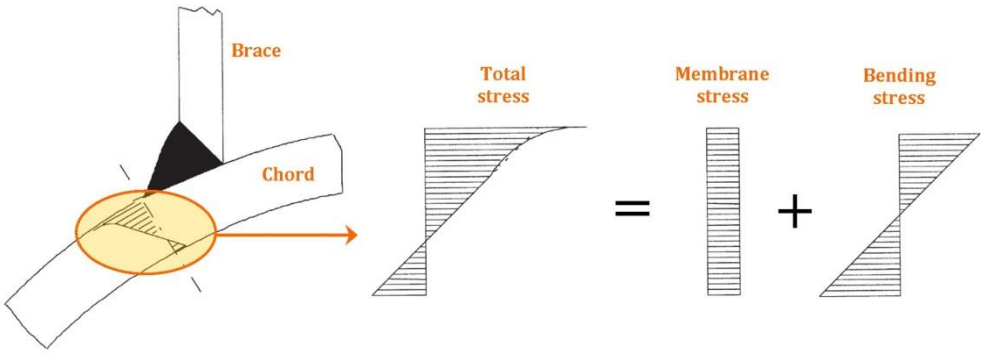

Fig. 2. Through-the-thickness stress distribution in a tubular joint.

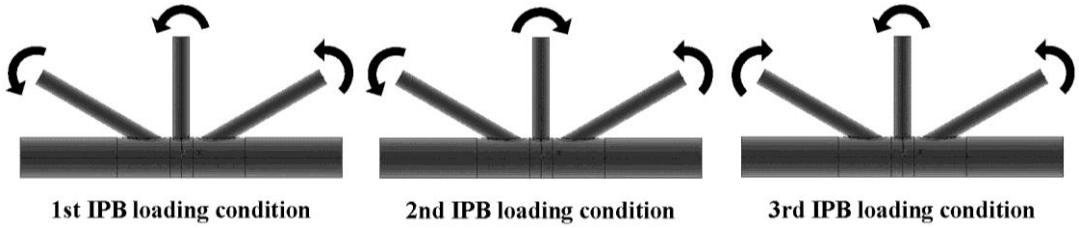

Fig. 3. Three applied IPB moment loading conditions.

2.1.1. Modeling of the weld profile

Accurate modeling of the weld profile is one of the important factors affecting the accuracy of the DoB results. In the present research, the welding size along the brace-to-chord intersection satisfies the AWS D 1.1 [27] specifications. The weld sizes at the crown, saddle, toe, and heel positions can be determined as follows:

$$H_w(\text{mm}) = 0.85t(\text{mm}) + 4.24$$

$$L_w = \frac{t}{2}\left[\frac{135^\circ - \psi\ (\text{deg.})}{45^\circ}\right]$$

$$\psi = \begin{cases} 90^\circ & \text{Crown} \\ 180^\circ - \cos^{-1}\beta\ (\text{deg.}) & \text{Saddle} \\ 180^\circ - \theta\ (\text{deg.}) & \text{Toe} \\ \theta\ (\text{deg.}) & \text{Heel} \end{cases} \quad (2)$$

The parameters of Eq. (2) are defined in Fig. 4. As an example, the weld profiles generated for the central and outer braces of the joint model SKTJ1 (α = 16, α_B = 8, ζ = 0.3, τ = 0.4, β = 0.4, γ = 12, θ = 30˚) are shown in Fig. 5. For details of the weld profile modeling according to AWS D 1.1 [27], the reader is referred to Lie et al. [28] and Ahmadi et al. [29].

2.1.2. Definition of boundary conditions

In view of the fact that the effect of chord end restraints is only significant for joints with α < 8 and high β and γ values, which do not commonly occur in practice [3, 30, 31], both chord ends were assumed to be fixed, with the corresponding nodes restrained.

Under each of the three considered loading conditions, only an appropriate portion of the entire tubular KT-joint is required to be modeled. The reason is the symmetry in geometry, material properties, and chord-end boundary conditions of the joint, as well as loading symmetry/antisymmetry. This allowed us to consider a reduced FE problem instead of the actual one. Thus, the order of the global stiffness matrix and total number of stiffness equations were reduced and computer solution time was substantially decreased. Table 1 and Fig. 6 describe the required portion to be modeled for each load case. Appropriate symmetric/antisymmetric boundary conditions were defined for the nodes located on the symmetry/antisymmetry planes.

2.1.3. Generation of the FE mesh

ANSYS element type SOLID95 was used in the present research to model the chord, braces, and the weld profiles. Using this type of 3-D brick elements, the weld profile can be modeled as a sharp notch. This method will produce more accurate and detailed stress distribution near the intersection in comparison with a shell analysis. The mesh generated for a tubular KT-joint is shown in Fig. 7.

2.1.4. Analysis procedure and extraction of DoB values

To calculate the DoB values in a tubular joint, static analysis of the linearly elastic type is suitable. The Young's modulus and Poisson's ratio were taken to be 207 GPa and 0.3, respectively.

In order to determine the weld-toe DoB values, according to Eq. (1), bending and membrane stress components should be known. These components can be calculated as follows:

$$\sigma_B = \frac{\sigma_O - \sigma_I}{2} \quad (3)$$

$$\sigma_M = \frac{\sigma_O + \sigma_I}{2} \quad (4)$$

where σ_o and σ_I are the hot-spot stresses (HSSs) at the weld toe on the outer and inner surfaces of the chord, respectively.

Eqs. (1), (3), and (4) lead to the following relation for the DoB based on the HSSs:

$$\text{DoB} = \frac{1}{2}\left(1 - \frac{\sigma_I}{\sigma_O}\right) \quad (5)$$

To determine the HSSs, the stress at the weld-toe position should be extracted from the stress field outside the region influenced by the local weld-toe geometry. The location from which the stresses have to be extrapolated, called extrapolation region, depends on the dimensions of the joint and on the position along the intersection. According to the recommendations of IIW-XV-E [32], the first extrapolation point should be at a distance of 0.4T from the weld toe, and the second point must be 1.0T further from the first point (Fig. 8a). The HSS is obtained by the linear extrapolation of the geometric stresses at these two points to the weld toe.

To extract and extrapolate the stresses perpendicular to the weld toe, as shown in Fig. 8a, the region between the weld toe and the second extrapolation point was meshed in such a way that each extrapolation point was placed between two nodes located in its immediate vicinity. These nodes are located on the element-generated lines which are perpendicular to the weld toe ($X_\perp$ direction in Fig. 8b).

2.1.5. Verification of the FE modeling

As far as the authors can tell, there is no experimental data available in the literature on the DoB values in tubular KT-joints. However, previous research works offer some experimental data, FE results, and parametric equations that can be used to validate the FE model developed in the present study.

2.1.5.a. Comparison with experimental data for the HSS

According to Eq. (5), DoB is a function of σ_o and σ_I that are the HSSs at the weld toe on the outer and

inner surfaces of the chord, respectively. Hence, if the proposed FE model could predict the HSS accurately, then undoubtedly it is capable of resulting in accurate DoB values.

To verify the developed FE modeling procedure, a validation FE model was generated and its results were compared with the results of experimental tests carried out by the first author on a KT-joint (Figs. 9 and 10). Details of the test setup and program presented by Ahmadi [33] are not repeated here for the sake of brevity.

Results of verification process are presented in Table 2. It can be seen that there is a good agreement between the results of present FE model and experimental data; and the average difference is about 10%. Hence, developed FE model can be considered to be accurate enough to provide valid results.

2.1.5.b. Comparison with available DoB parametric equations and FE results

A set of FE parametric studies have been conducted by Morgan and Lee [3], Ahmadi et al. [7], and Ahmadi and Asoodeh [8] for the prediction of DoB values in tubular K-joints under the axial, IPB, and OPB loadings, respectively. Results of these studies were used in the present research to validate the developed FE model. In order to do so, three K-joint FE models were generated having typical geometrical characteristics (Table 3) and they were analyzed under the axial, IPB, and OPB loadings shown in Fig. 11. Geometrical properties of the axially-loaded FE model were selected based on the data provided by HSE OTH 354 [34] for a steel specimen tested to determine the SCFs; and geometrical properties of the IPB- and OPB-loaded FE models were selected in accordance with the validity range of the FE study conducted by Ahmadi et al. [7] and Ahmadi and Asoodeh [8].

The method of geometrical modeling (introducing the chord, braces, and weld profiles), the mesh generation procedure (including the selection of element type and size), analysis method, and the method of DoB extraction are identical for the validating models and the KT-joint models used for the parametric study. Hence, the verification of DoB values derived from validating FE models with the results of equations proposed by Morgan and Lee [3], FE results of Ahmadi et al. [7], and FE results of Ahmadi and Asoodeh [8] lends some support to the validity of DoB values derived from the KT-joint FE models.

Results of verification process are presented in Table 4. It can be seen that there is a good agreement among the results of present FE model and equations proposed by Morgan and Lee [3], FE results of Ahmadi et al. [7], and FE results of Ahmadi and Asoodeh [8]. The average difference is less than 10%. Hence, generated FE models can be considered to be accurate enough to provide valid results.

2.2. Details of parametric study

Altogether, 243 stress analyses were carried out on 81 FE models using ANSYS Ver. 11 to investigate the effects of dimensionless geometrical parameters on the DoB values at the crown, toe, and heel positions in tubular KT-joints subjected to three different types of IPB moment loading (Fig. 3).

Different values assigned to the parameters β, γ, τ, and θ have been presented in Table 5. These values cover the practical ranges of the dimensionless parameters typically found in tubular joints of offshore jacket structures.

Where the gap between the braces is not very large, the relative gap ($\zeta = g / D$) has no considerable effect on the stress and strain distribution. The validity range for this statement is $0.2 \leq \zeta \leq 0.6$ [19]. Hence, a typical value of $\zeta = 0.3$ was designated for all joints. Sufficiently long chord greater than six chord diameters (i.e. $\alpha \geq 12$) should be used to ensure that the stresses at the brace/chord intersection are not affected by the chord's boundary conditions [13]. The brace length has no effect on the HSSs when the parameter α_B is greater than a critical value [16]. According to Chang and Dover [35], this critical value is about 6. In the present study, in order to avoid the effect of short brace length, a realistic value of $\alpha_B = 8$ was selected for all joints.

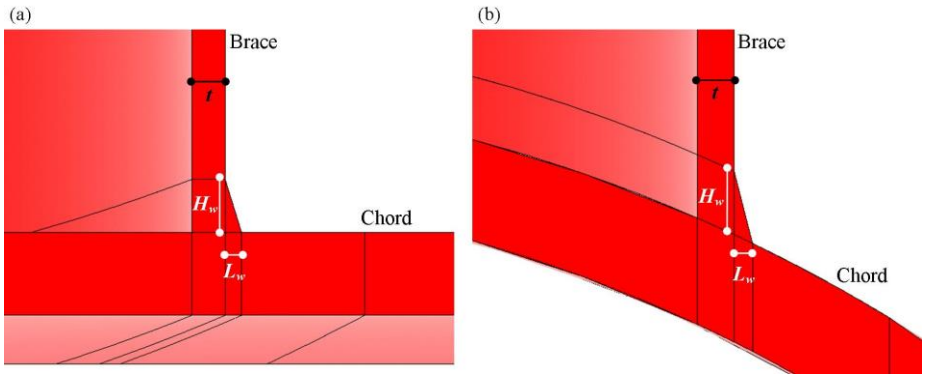

Fig. 4. Weld dimensions: (a) Crown position, (b) Saddle position.

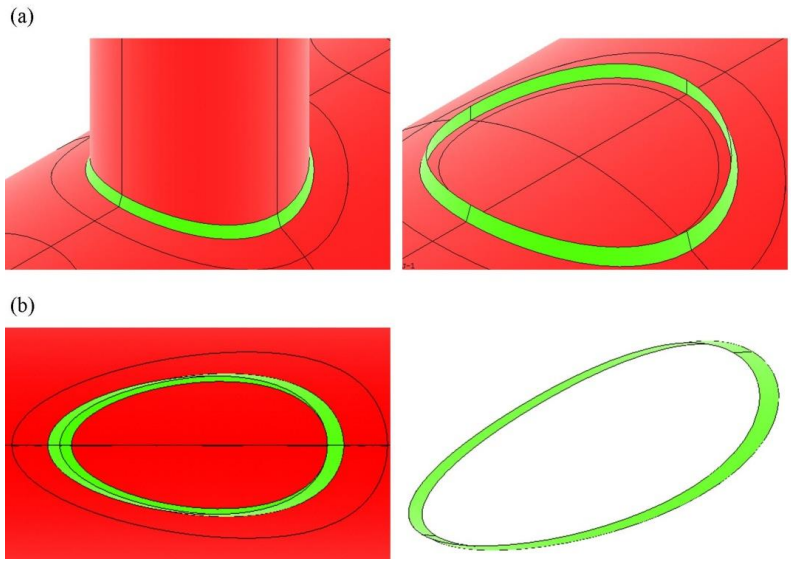

Fig. 5. Simulated weld profile: (a) Central brace, (b) Outer brace.

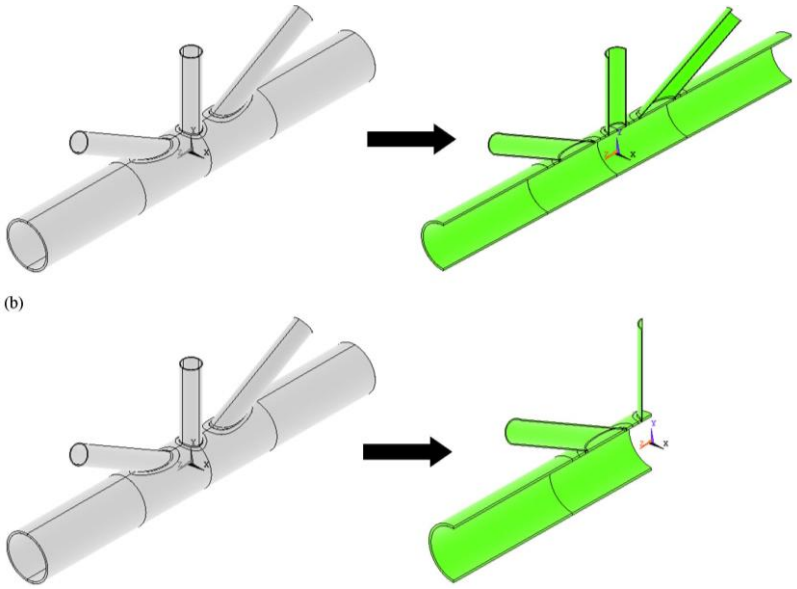

Fig. 6. Appropriate portion of the entire tubular KT-joint required to be modeled for each load case based on Table 1: (a) ½, (b) ¼.

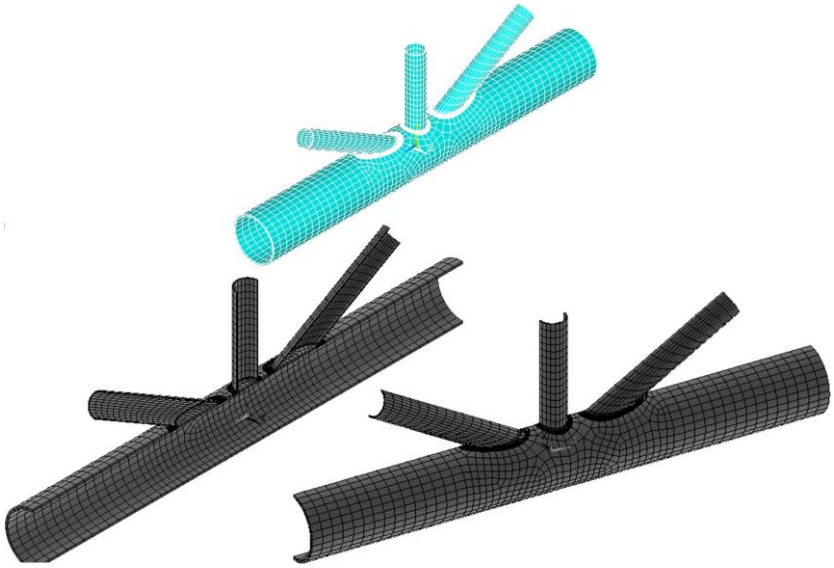

Fig. 7. Generated mesh for a tubular KT-joint using the sub-zone method.

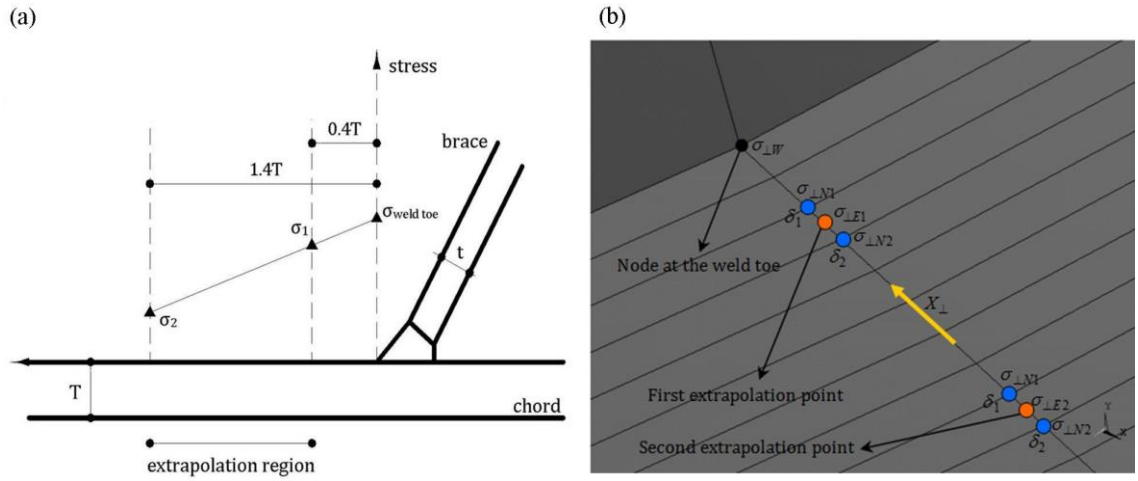

Fig. 8. (a) Extrapolation method recommended by IIW-XV-E [32], (b) Interpolations and extrapolations necessary to compute the DoB value based on the HSSs at the weld toe.

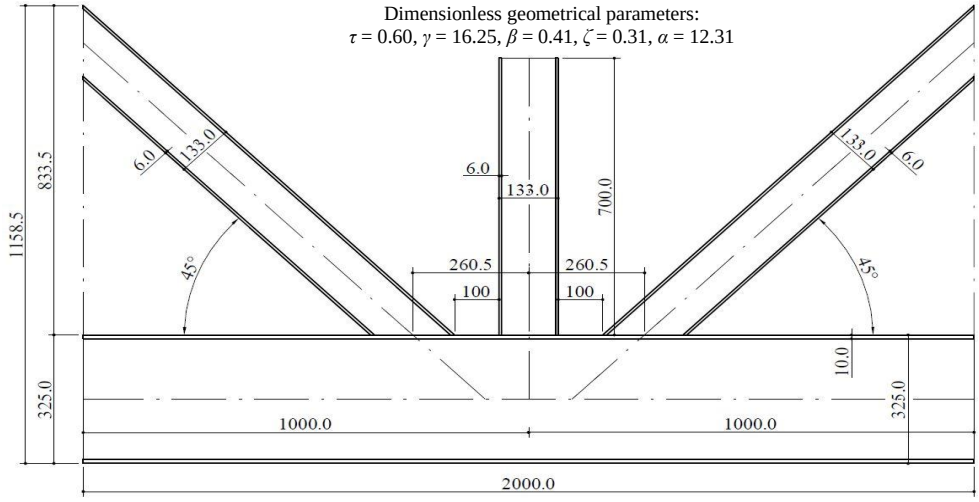

Fig. 9. Geometrical characteristics of tested tubular KT-joint specimen (unit: mm) [33].

Fig. 10. Test setup [33]: (a) View of the test rig and KT-joint specimen, (b) Strain gauges attached along the brace-to-chord intersection, (c) Connecting the strain gauges to the data logger.

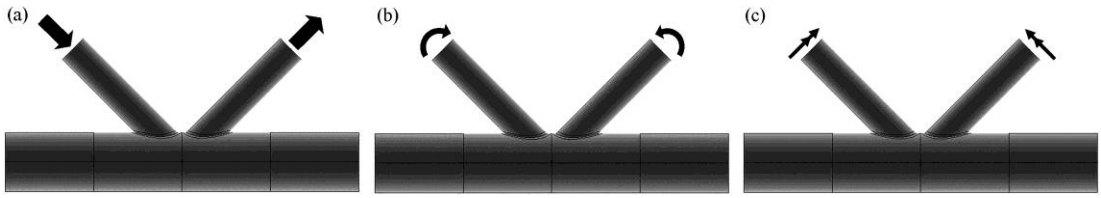

Fig. 11. Load cases for FE model validation: (a) Balanced axial loading studied by Morgan and Lee [3], (b) Balanced IPB loading studied by Ahmadi et al. [7], (c) Balanced OPB loading studied by Ahmadi and Asoodeh [8].

The 81 generated models span the following ranges of geometrical parameters:

$$\begin{aligned} &0.4 \le \beta \le 0.6 \\ &12 \le \gamma \le 24 \\ &0.4 \le \tau \le 1.0 \\ &30^\circ \le \theta \le 60^\circ \end{aligned} \quad (6)$$

2.3. Organization of the DoB samples

The DoB values extracted from the results of 243 FE analyses were organized as nine samples for further statistical and probabilistic analyses. Samples 1−3 included the DoB values at the crown position of the central brace under the 1st–3rd IPB loading conditions, respectively; while samples 4−6 included the DoB values at the toe position of the outer brace under the 1st–3rd IPB loading conditions, respectively; and samples 7−9 included the DoB values at the heel position of the outer brace under the 1st–3rd IPB loading conditions, respectively. Values of the size (n), mean (μ), standard deviation (σ), coefficient of skewness (α_3), and coefficient of kurtosis (α_4) for Samples 1−3 are listed in Table 6 as an example.

The value of α_3 for the crown and heel position DoB samples is positive which means that the probability distribution for these samples is expected to have a longer tail on the right, which is toward increasing values, than on the left. However, the value of α_3 for the toe position DoB samples is negative which means that the probability distribution for these samples is expected to have a longer tail on the left, which is toward decreasing values, than on the right.

Moreover, the value of α_4 for the crown and toe position DoB samples is smaller than three meaning that the probability distribution is expected to be mild-peak (platykurtic) for these samples; while the value of α_4 for the heel position DoB samples is greater than three which means that for these samples, the probability distribution is expected to be sharp-peak (leptokurtic).

3. Probabilistic analysis

3.1. Generation of density histograms based on the Freedman-Diaconis rule

To generate a density histogram, the range of data (R) is divided into a number of classes and the number of occurrences in each class is counted and tabulated. These are called frequencies. Then, the relative frequency of each class can be obtained through dividing its frequency by the sample size. Afterwards, the density is calculated for each class through dividing the relative frequency by the class width. The width of classes is usually made equal to facilitate interpretation. One of the widely accepted rules to determine the number of classes is the Freedman-Diaconis rule [36].

As an example, density histograms of Samples 1−6 are shown in Fig. 12. This figure shows that, as it was expected from the values of α_3 and α_4:

1. The right tail is longer than the left one in the histograms of samples 1−3 and 7−9; while in the histograms of samples 4−6, the left tail is longer.
2. The histograms of samples 1−6 are platykurtic; while the histograms of samples 7−9 are leptokurtic.

3.2. Application of the maximum likelihood method for PDF fitting

Thirteen different PDFs were fitted to the density histograms to assess the degree of fitting of various distributions to the DoB samples. In each case, distribution parameters were estimated using the maximum likelihood (ML) method. Results for Samples 1−3 are given in Table 7 as an example. For more information regarding the definition of distribution parameters, the reader is referred to Kottegoda and Rosso [36].

3.3. Assessment of the goodness-of-fit based on the Kolmogorov-Smirnov test

The Kolmogorov-Smirnov goodness-of-fit test is a nonparametric test that relates to the cumulative distribution function (CDF) of a continuous variable. The test statistic (d_n), in a two-sided test, is the maximum absolute difference (which is usually the vertical distance) between the empirical and hypothetical CDFs.

A large value of this statistic indicates a poor fit. Hence, acceptable values should be known. The critical values $D_{n,\xi}$ for large samples, say $n > 35$, are $(1.3581/\sqrt{n})$ and $(1.6276/\sqrt{n})$ for $\xi = 0.05$ and 0.01, respectively [36] where ξ is the significance level.

As an example, empirical distribution functions for Samples 1–6 have been shown in Fig. 13.

Theoretical continuous CDFs fitted to the empirical distribution functions of Samples 4–9 have been shown in Fig. 14 as an example.

Results of the Kolmogorov-Smirnov test for Sample 1 are given in Table 8 as an example. The Beta,

Lognormal, and Log-logistic distributions had the smallest d_n value for samples 1−3, respectively. The Extreme Value distribution has the smallest d_n for samples 4 and 6; and Generalized Extreme Value distribution has the smallest d_n for samples 5 and 7−9. Hence, they are the best-fitted distributions for the corresponding DoB samples (Fig. 15).

3.4. Proposed probability distribution model for the DoB

The best fitted distributions for the generated DoB samples were introduced in Sect. 6. According to the results of the Kolmogorov-Smirnov test, it can be seen that the best-fitted distributions for the nine studied samples include five different models: Beta, Lognormal, Log-logistic, Extreme Value, and Generalized Extreme Value distributions. The diversity of the best-fitted probability models derived for the studied DoB values may practically result in the confusion and difficulty of their application for the fatigue reliability analysis and design. Hence, reducing the number of distribution types proposed for the DoB values might be a good idea. In order to do so, the top three distribution functions for each DoB sample were identified (Table 9 for Samples 1–3 as an example). The aim was to propose a single probability model to cover all the DoB samples. It should be noted that, for each sample, all of the three mentioned functions have acceptable fit according to the Kolmogorov-Smirnov test.

After surveying the data (presented in Table 9 for Samples 1–3 as an example), the Generalized Extreme Value model is proposed as the governing probability distribution function for the DoB values. The difference between the test statistics of the proposed distribution and the best-fitted one for each sample is presented in Tables 10–12. Using the information presented in these tables, the analyst is able to make a choice, based on the engineering judgment, between the best-fitted and the proposed probability models for each of the studied cases.

The PDF of the Generalized Extreme Value distribution is expressed as [36]:

$$f_X(x) = \left(\frac{1}{\sigma}\right)\exp\left(-\left(1+k\,\frac{(x-\mu)}{\sigma}\right)^{-\frac{1}{k}}\right) \times\left(1+k\,\frac{(x-\mu)}{\sigma}\right)^{-1-\frac{1}{k}} \tag{7}$$

After substituting the values of estimated parameters (for example, from Table 7 for Samples 1–3), following probability density functions are proposed for the DoB values in tubular KT-joints subjected to the three considered IPB load cases defined in Fig. 3:

Crown position of the central brace−1st IPB loading condition:

$$f_X(x) = 36.27144\exp\left[-\left(1-10.35238\,(x-0.87975)\right)^{3.50368}\right]\left[1-10.35238\,(x-0.87975)\right]^{2.50368} \tag{8}$$

Crown position of the central brace−2nd IPB loading condition:

$$f_X(x) = 25.83359\exp\left[-\left(1-7.70786\,(x-0.67778)\right)^{3.35159}\right]\left[1-7.70786\,(x-0.67778)\right]^{2.35159} \tag{9}$$

Crown position of the central brace−3rd IPB loading condition:

$$f_X(x) = 21.33752\exp\left[-\left(1-1.64464\,(x-0.56854)\right)^{12.97399}\right]\left[1-1.64464\,(x-0.56854)\right]^{11.97399} \tag{10}$$

Toe position of the outer brace−1st IPB loading condition:

$$f_X(x) = 21.14500\exp\left[-\left(1-10.90587\,(x-0.78212)\right)^{1.93886}\right]\left[1-10.90587\,(x-0.78212)\right]^{0.93886} \tag{11}$$

Toe position of the outer brace−2nd IPB loading condition:

$$f_X(x) = 14.84726\exp\left[-\left(1-9.23936\,(x-0.68232)\right)^{1.60696}\right]\left[1-9.23936\,(x-0.68232)\right]^{0.60696} \tag{12}$$

Toe position of the outer brace−3rd IPB loading condition:

$$f_X(x) = 14.08514\exp\left[-\left(1-7.90137\,(x-0.64752)\right)^{1.78262}\right]\left[1-7.90137\,(x-0.64752)\right]^{0.78262} \tag{13}$$

Heel position of the outer brace−1st IPB loading condition:

$$f_X(x) = 18.68925\exp\left[-\left(1+2.92638\,(x-0.76812)\right)^{-6.38647}\right]\left[1+2.92638\,(x-0.76812)\right]^{-7.38647} \tag{14}$$

Heel position of the outer brace−2nd IPB loading condition:

$$f_X(x) = 15.50727\exp\left[-\left(1-0.17675\,(x-0.79780)\right)^{87.73700}\right]\left[1-0.17675\,(x-0.79780)\right]^{86.73700} \tag{15}$$

Heel position of the outer brace−3rd IPB loading condition:

$$f_X(x) = 17.14981\exp\left[-\left(1+2.11756\,(x-0.82963)\right)^{-8.09887}\right]\left[1+2.11756\,(x-0.82963)\right]^{-9.09887} \tag{16}$$

where X denotes the DoB as a random variable and x represents its values.
Developed PDFs are shown in Fig. 16 for Samples 1–6 as an example.

4. Conclusions

In the present paper, a total of 243 FE analyses were carried out on 81 models of KT-joints subjected to three types of IPB moment loading. Generated FE models were validated using experimental data, previous FE results, and available parametric equations. FE analysis results were used to develop a set of PDFs for the DoB in IPB-loaded KT-joints. Based on the results of parametric FE study, a sample database was prepared for the DoB values and density histograms were generated for respective samples based on the Freedman-Diaconis rule. Thirteen theoretical PDFs were fitted to the developed histograms and the ML method was applied to evaluate the parameters of fitted PDFs. In each case, the Kolmogorov-Smirnov test was used to evaluate the goodness of fit. Finally, the Generalized Extreme Value model was proposed as the governing probability distribution function for the DoB. After substituting the values of estimated parameters, nine fully defined PDFs were presented for the DoB at the crown, toe, and heel positions of central and outer braces in tubular KT-joints subjected to three types of IPB moment loading.

Acknowledgments

Useful comments of anonymous reviewers on draft version of this paper are highly appreciated.

References

1- Connolly, M.P.M., (1986), *A fracture mechanics approach to the fatigue assessment of tubular welded Y and K-joints*, PhD Thesis, University College London, UK.
2- Chang, E., Dover, W.D., (1999), *Prediction of degree of bending in tubular X and DT joints*, International Journal of Fatigue, Vol. 21 (2), p. 147-161.
3- Morgan, M.R., Lee, M.M.K., (1998), *Prediction of stress concentrations and degrees of bending in axially loaded tubular K-joints*, Journal of Constructional Steel Research, Vol. 45 (1), p. 67-97.
4- UK Department of Energy (DoE), (1995), *Background to new fatigue design guidance for steel joints and connections in offshore structures*, London, UK.
5- Lee, M.M.K., Bowness, D., (2002), *Estimation of stress intensity factor solutions for weld toe cracks in offshore tubular joints*, International Journal of Fatigue, Vol. 24, p. 861-875.
6- Shen, W., Choo, Y.S., (2012), *Stress intensity factor for a tubular T-joint with grouted chord*, Engineering Structures, Vol. 35, p. 37-47.
7- Ahmadi, H., Lotfollahi-Yaghin, M.A., Asoodeh, S., (2015), *Degree of bending (DoB) in tubular K-joints of offshore structures subjected to in-plane bending (IPB) loads: Study of geometrical effects and parametric formulation*, Ocean Engineering, Vol. 102, p. 105-116.
8- Ahmadi, H., Asoodeh, S., (2016), *Parametric study of geometrical effects on the degree of bending (DoB) in offshore tubular K-joints under out-of-plane bending loads*, Applied Ocean Research, Vol. 58, p. 1-10.
9- Ahmadi, H., Asoodeh, S, (2015), *Degree of bending (DoB) in tubular KT-joints of jacket structures subjected to axial loads*, International Journal of Maritime Technology, Vol. 4 (2), p. 65-75.
10- Ahmadi, H., Amini Niaki, M., (2019), *Effects of geometrical parameters on the degree of bending (DoB) in two-planar tubular DT-joints of offshore jacket structures subjected to axial and bending loads*, Marine Structures, Vol. 64 (C), p. 229-245.
11- Ahmadi, H., Ghaffari, A.R., (2015), *Probabilistic assessment of degree of bending (DoB) in tubular X-joints of offshore structures subjected to bending loads*, Advances in Civil Engineering, p. 1-12.
12- Ahmadi, H., Ghaffari, A.R., (2015), *Probabilistic analysis of stress intensity factor (SIF) and degree of bending (DoB) in axially loaded tubular K-joints of offshore structures*, Latin American Journal of Solids and Structures, Vol. 12 (11), p. 2025-2044.
13- Efthymiou, M., (1988), *Development of SCF formulae and generalized influence functions for use in fatigue analysis*, OTJ 88, Surrey, UK.
14- Hellier, A.K., Connolly, M., Dover, W.D., (1990), *Stress concentration factors for tubular Y and T-joints*, International Journal of Fatigue, Vol. 12, p. 13-23.
15- Morgan, M.R., Lee, M.M.K., (1998), *Parametric equations for distributions of stress concentration factors in tubular K-joints under out-of-plane moment loading*, International Journal of Fatigue, Vol. 20, 449-461.
16- Chang, E., Dover, W.D., (1999), *Parametric equations to predict stress distributions along the intersection of tubular X and DT-joints*. International Journal of Fatigue, Vol. 21, p. 619-635.
17- Shao, Y.B., (2007), *Geometrical effect on the stress distribution along weld toe for tubular T- and K-joints under axial loading*, Journal of Constructional Steel Research, Vol. 63, p. 1351-1360.
18- Shao, Y.B., Du, Z.F., Lie, S.T., (2009), *Prediction of hot spot stress distribution for tubular K-joints under basic loadings*, Journal of Constructional Steel Research, Vol. 65, 2011-2026.
19- Lotfollahi-Yaghin, M.A., Ahmadi, H., (2010), *Effect of geometrical parameters on SCF distribution along the weld toe of tubular KT-joints under balanced axial loads*, International Journal of Fatigue, Vol. 32, p. 703-719.

20- Ahmadi, H., Lotfollahi-Yaghin, M.A., Aminfar, M.H., (2011), *Geometrical effect on SCF distribution in uni-planar tubular DKT-joints under axial loads*, Journal of Constructional Steel Research, Vol. 67, p. 1282-1291.

21- Lotfollahi-Yaghin, M.A., Ahmadi, H., (2011), *Geometric stress distribution along the weld toe of the outer brace in two-planar tubular DKT-joints: parametric study and deriving the SCF design equations*, Marine Structures, Vol. 24, p. 239-260.

22- Ahmadi, H., Lotfollahi-Yaghin, M.A., (2012), *Geometrically parametric study of central brace SCFs in offshore three-planar tubular KT-joints*, Journal of Constructional Steel Research, Vol. 71, 149-161.

23- Ahmadi, H., Lotfollahi-Yaghin, M.A., Shao, Y.B., (2013), *Chord-side SCF distribution of central brace in internally ring-stiffened tubular KT-joints: A geometrically parametric study*, Thin-Walled Structures, Vol. 70, p. 93-105.

24- Ahmadi, H., Zavvar, E., (2016), *The effect of multi-planarity on the SCFs in offshore tubular KT-joints subjected to in-plane and out-of-plane bending loads*, Thin-Walled Structures, Vol. 106, p. 148-165.

25- Shao, Y.B., Lie, S.T., (2005), *Parametric equation of stress intensity factor for tubular K-joint under balanced axial loads*, International Journal of Fatigue, Vol. 27, 666-679.

26- Shao, Y.B., (2006), *Analysis of stress intensity factor (SIF) for cracked tubular K-joints subjected to balanced axial load*, Engineering Failure Analysis, Vol. 13, p. 44-64.

27- American Welding Society (AWS), (2002), *Structural welding code: AWS D 1.1*, Miami (FL), US.

28- Lie, S.T., Lee, C.K., Wong, S.M., (2001), *Modeling and mesh generation of weld profile in tubular Y-joint*, Journal of Constructional Steel Research, Vol. 57, p. 547-567.

29- Ahmadi, H., Lotfollahi-Yaghin, M.A., Shao, Y.B., Aminfar M.H., (2012), *Parametric study and formulation of outer-brace geometric stress concentration factors in internally ring-stiffened tubular KT-joints of offshore structures*, Applied Ocean Research, Vol. 38, p. 74-91.

30- Wordsworth, A.C., Smedley, G.P., (1978), *Stress concentrations at unstiffened tubular joints*, Proceedings of the European Offshore Steels Research Seminar, Paper 31, Cambridge, UK.

31- Smedley, P., Fisher, P., (1991), *Stress concentration factors for simple tubular joints*, Proceedings of the International Offshore and Polar Engineering Conference (ISOPE), Edinburgh, p. 475-483.

32- IIW-XV-E, (1999), *Recommended fatigue design procedure for welded hollow section joints, IIW Docs, XV-1035-99/XIII-1804-99*, International Institute of Welding, France.

33- Ahmadi, H., (2012), *Experimental and numerical investigation of the SCF distribution in unstiffened and stiffened uniplanar tubular KT-joints of steel platforms and the extension of numerical study to multi-planar joints*, PhD Thesis, Faculty of Civil Engineering, University of Tabriz, Tabriz, Iran (In Farsi).

34- UK Health and Safety Executive, (1997), *OTH 354: Stress concentration factors for simple tubular joints- assessment of existing and development of new parametric formulae*. Prepared by Lloyd's Register of Shipping, UK.

35- Chang, E., Dover, W.D., (1996), *Stress concentration factor parametric equations for tubular X and DT joints*, International Journal of Fatigue, Vol. 18 (6), p. 363-387.

36- Kottegoda, N.T., Rosso, R., (2008), *Applied statistics for civil and environmental engineers*, 2nd Edition, Blackwell Publishing Ltd, UK.

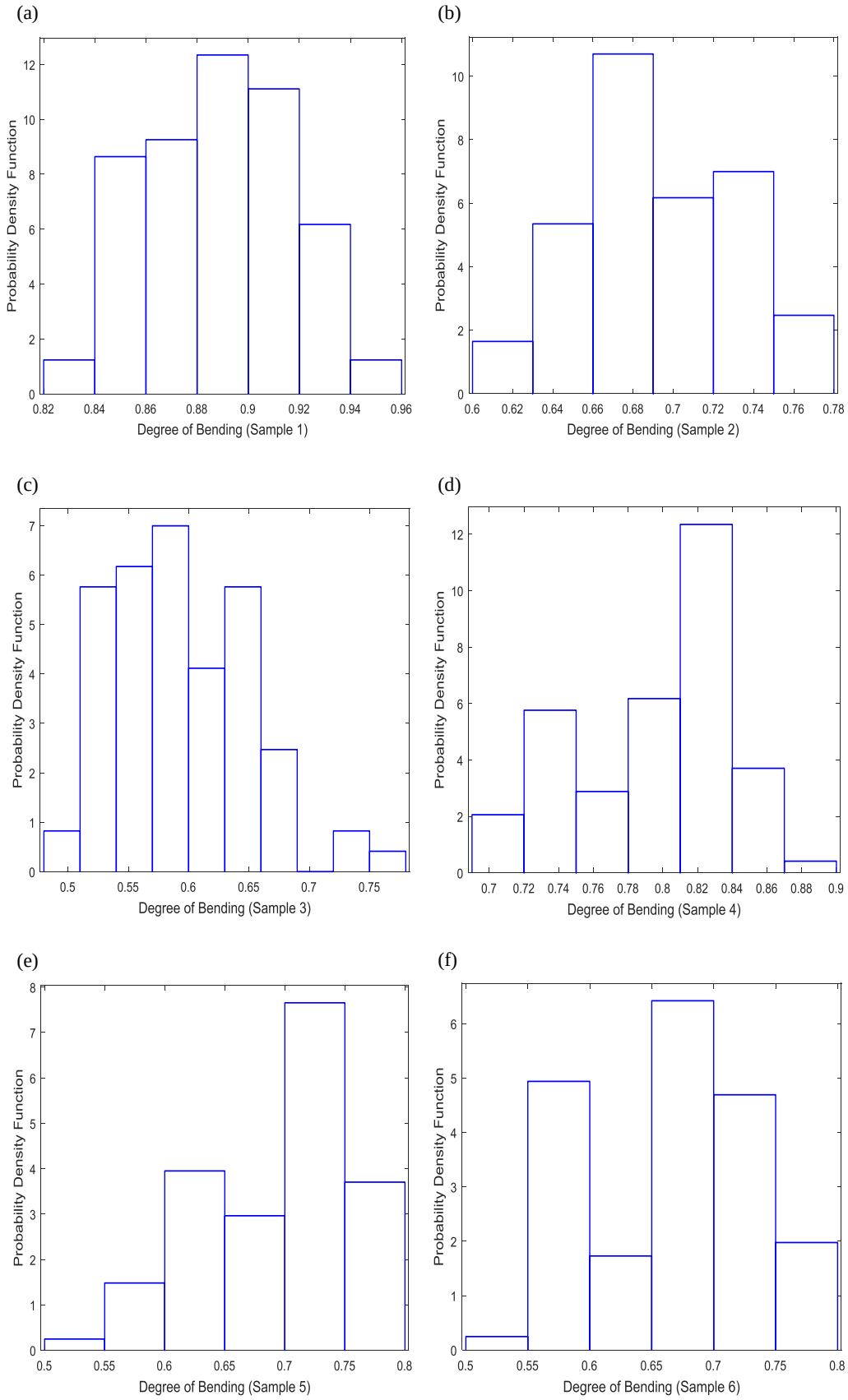

Fig. 12. Density histograms generated for the DoB samples: (a) Sample 1 (Cr, CB, 1st IPB LC), (b) Sample 2 (Cr, CB, 2nd IPB LC), (c) Sample 3 (Cr, CB, 3rd IPB LC), (d) Sample 4 (T, OB, 1st IPB LC), (e) Sample 5 (T, OB, 2nd IPB LC), (f) Sample 6 (T, OB, 3rd IPB LC) [Key– Cr: Crown; T: Toe; CB: Central brace; OB: Outer brace; LC: Loading condition].

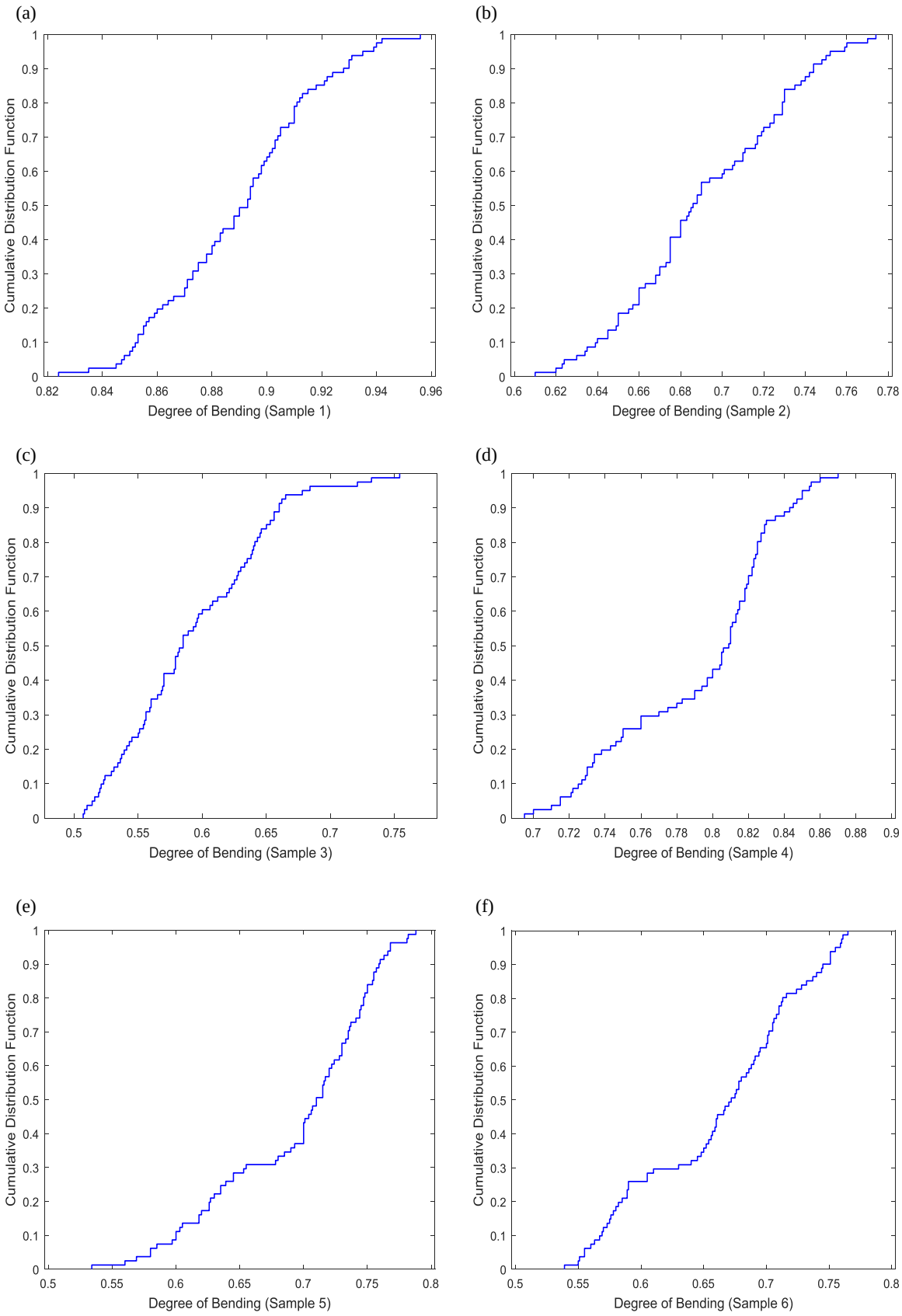

Fig. 13. Empirical cumulative distribution functions for generated DoB samples: (a) Sample 1 (Cr, CB, 1st IPB LC), (b) Sample 2 (Cr, CB, 2nd IPB LC), (c) Sample 3 (Cr, CB, 3rd IPB LC), (d) Sample 4 (T, OB, 1st IPB LC), (e) Sample 5 (T, OB, 2nd IPB LC), (f) Sample 6 (T, OB, 3rd IPB LC) [Key– Cr: Crown; T: Toe; CB: Central brace; OB: Outer brace; LC: Loading condition].

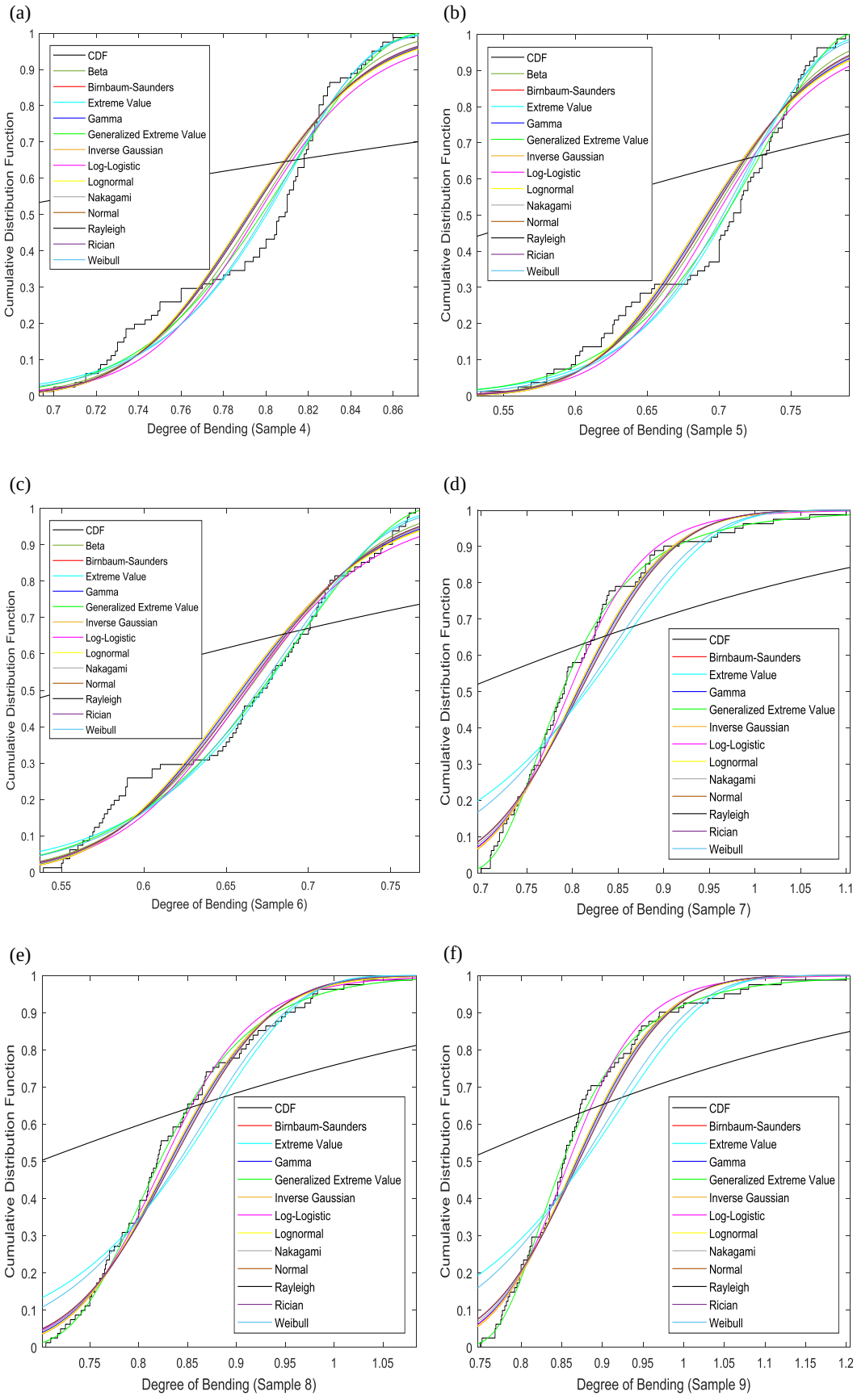

Fig. 14. Theoretical continuous CDFs fitted to the empirical CDFs of generated DoB samples: (a) Sample 1 (Cr, CB, 1st IPB LC), (b) Sample 2 (Cr, CB, 2nd IPB LC), (c) Sample 3 (Cr, CB, 3rd IPB LC), (d) Sample 4 (T, OB, 1st IPB LC), (e) Sample 5 (T, OB, 2nd IPB LC), (f) Sample 6 (T, OB, 3rd IPB LC) [Key– Cr: Crown; T: Toe; CB: Central brace; OB: Outer brace; LC: Loading condition].

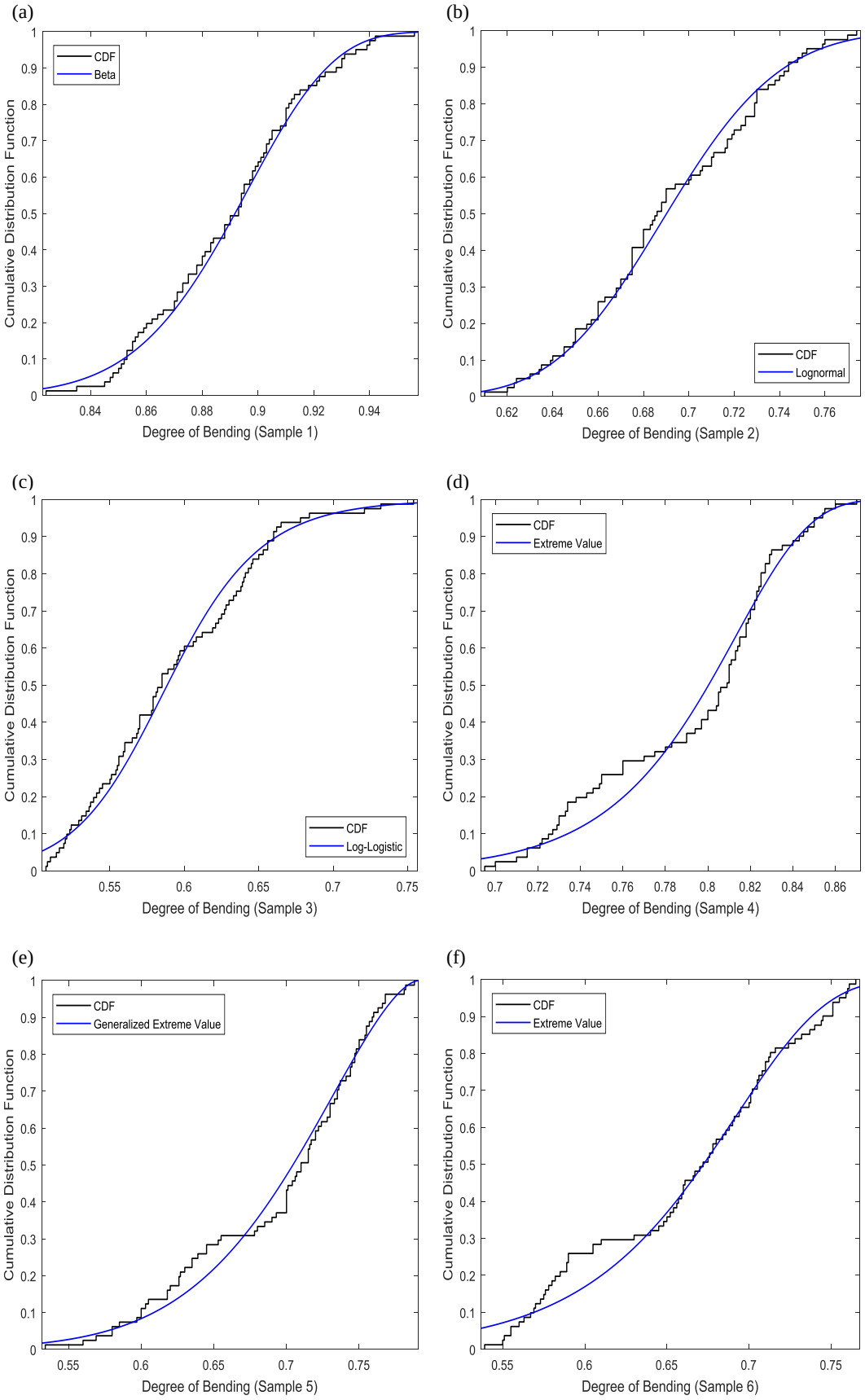

Fig. 15. The best-fitted distributions according to the Kolmogorov-Smirnov test: (a) Sample 1 (Cr, CB, 1st IPB LC), (b) Sample 2 (Cr, CB, 2nd IPB LC), (c) Sample 3 (Cr, CB, 3rd IPB LC), (d) Sample 4 (T, OB, 1st IPB LC), (e) Sample 5 (T, OB, 2nd IPB LC), (f) Sample 6 (T, OB, 3rd IPB LC) [Key– Cr: Crown; T: Toe; CB: Central brace; OB: Outer brace; LC: Loading condition].

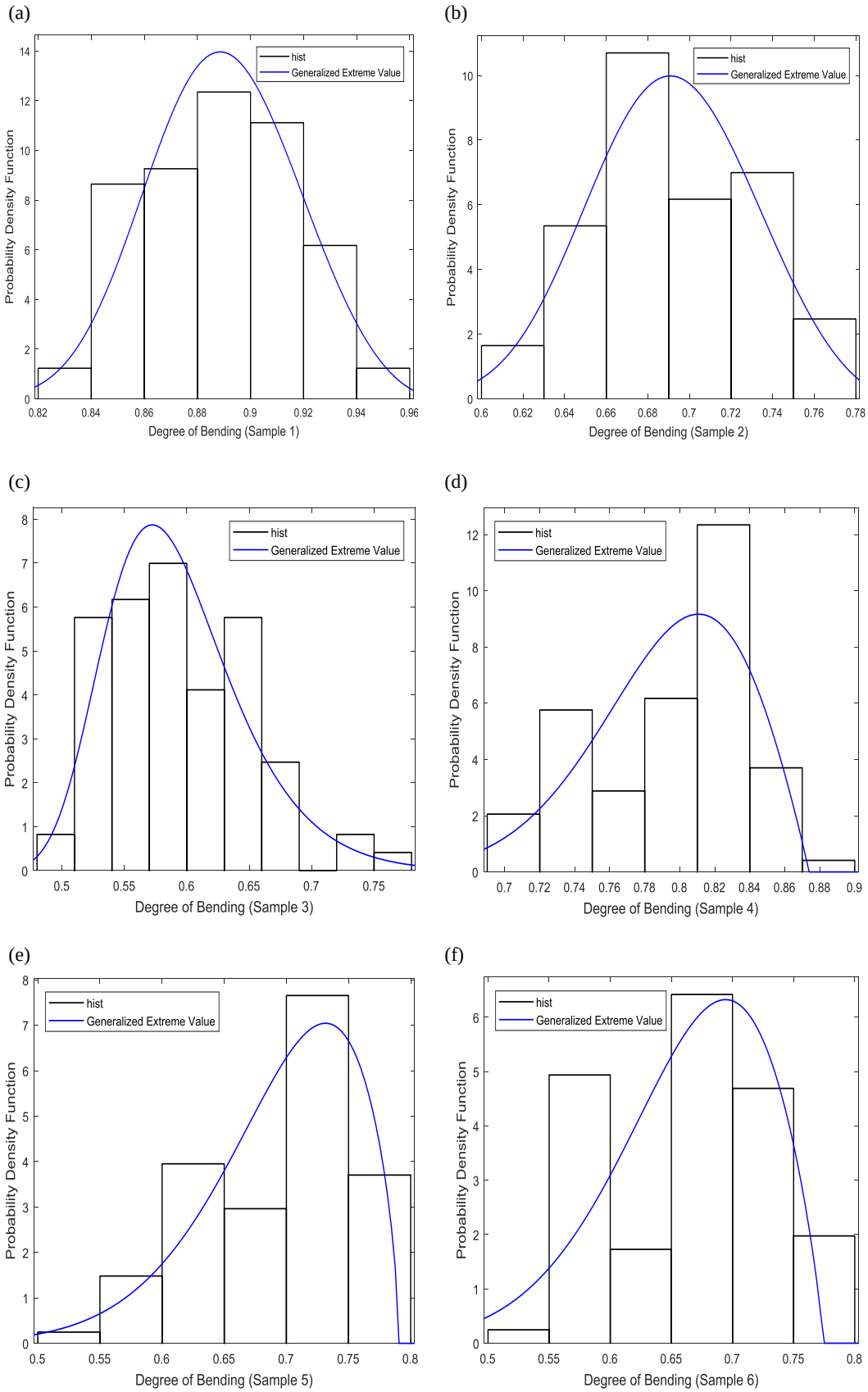

Fig. 16. Proposed PDFs for generated DoB samples: (a) Sample 1 (Cr, CB, 1st IPB LC), (b) Sample 2 (Cr, CB, 2nd IPB LC), (c) Sample 3 (Cr, CB, 3rd IPB LC), (d) Sample 4 (T, OB, 1st IPB LC), (e) Sample 5 (T, OB, 2nd IPB LC), (f) Sample 6 (T, OB, 3rd IPB LC) [Key– Cr: Crown; T: Toe; CB: Central brace; OB: Outer brace; LC: Loading condition].

Table 1. Appropriate portion of an entire tubular KT-joint required to be modeled for each load case.

Load case (Fig. 3)	Required portion to be modeled
1st IPB moment loading condition	¼ (Fig. 6b)
2nd IPB moment loading condition	¼ (Fig. 6b)
3rd IPB moment loading condition	½ (Fig. 6a)

Table 2. Results of FE model verification based on experimental data.

Loading	Position	HSS value of the chord's outer surface σ_O (N/m^2)		Difference
		Present FE model	Experimental test [33]	
Axial	Saddle	5.48e+6	5.89e+6	6.96%
	Crown	2.94e+6	3.38e+6	13.02%

Table 3. Geometrical properties of the tubular K-joint specimen used for the verification of FE models.

Loading	Joint ID	D (mm)	τ	β	γ	α	θ	ζ
Axial	JISSP 3.3 [34]	508	1.0	0.5	20.3	12.6	45˚	0.15
IPB	KJ-1 [7]	500	0.4	0.4	12.0	12.0	30˚	0.15
OPB	KJ-1 [8]	500	0.4	0.4	12.0	12.0	30˚	0.15

Table 4. Results of the FE model verification based on available parametric equations/FE results.

Loading	Position	DoB values		Difference
		Present FE model	Available data	
Axial (Fig. 12a)	Saddle	0.6666	0.5529 (Morgan and Lee [3] Eq. (3d))	20.56%
	Toe	0.8727	0.8989 (Morgan and Lee [3] Eq. (3f))	2.91%
	Heel	0.7728	0.6997 (Morgan and Lee [3] Eq. (3b))	10.45%
IPB (Fig. 12b)	Toe	0.5991	0.5742 (Ahmadi et al. [7] FE model)	4.16%
OPB (Fig. 12c)	Saddle	0.8920	0.8045 (Ahmadi and Asoodeh [8] FE model)	10.87%

Table 5. Values assigned to each dimensionless parameter.

Parameter	Definition	Value(s)
β	d/D	0.4, 0.5, 0.6
γ	$D/2T$	12, 18, 24
τ	t/T	0.4, 0.7, 1.0
θ		30˚, 45˚, 60˚
ζ	g/D	0.3
α	$2L/D$	16
α_B	$2l/d$	8

Table 6. Statistical measures of generated DoB samples at the crown position of the central brace under IPB loadings.

Statistical measure	DoB samples		
	Sample 1	Sample 2	Sample 3
	1st IPB load case	2nd IPB load case	3rd IPB load case
n	81	81	81
μ	0.8895	0.6913	0.5926
σ	0.0279	0.0394	0.0552
α_3	0.0201	0.0788	0.5284
α_4	2.4055	2.1124	2.8107

Table 7. Estimated parameters for PDFs fitted to the density histograms of DoB samples at the crown position of the central brace under the IPB loadings.

Fitted PDF	Parameters	Estimated values		
		Sample 1	Sample 2	Sample 3
		1st IPB load case	2nd IPB load case	3rd IPB load case
Beta	a	106.262	95.1363	46.0466
	b	13.1971	42.4829	31.6323
Birnbaum-Saunders	β_0	0.889062	0.690177	0.590175
	γ_0	0.0311572	0.0566481	0.0911977
Extreme Value	μ	0.903347	0.710948	0.621296
	σ	0.0266994	0.0371451	0.0600721
Gamma	a	1031.04	312.152	119.434
	b	0.000862718	0.00221458	0.004962
Generalized Extreme Value	k	-0.285414	-0.298366	-0.0770773
	σ	0.0275699	0.0387093	0.0468658
	μ	0.879746	0.677775	0.568542
Inverse Gaussian	μ	0.889494	0.691284	0.59263
	λ	916.053	215.248	71.1072
Log-logistic	μ	-0.11727	-0.370982	-0.530274
	σ	0.0182218	0.0336679	0.0536431
Lognormal	μ	-0.117588	-0.370807	-0.527378
	σ	0.0313482	0.0569844	0.0916859
Nakagami	μ	258.046	78.2422	29.7141
	ω	0.791966	0.479405	0.354221
Normal	μ	0.889494	0.691284	0.59263
	σ	0.0278658	0.0393723	0.0552151
Rayleigh	b	0.629272	0.489594	0.420845
Rician	s	0.889062	0.690172	0.590061
	σ	0.0277	0.0391602	0.0549937
Weibull	a	0.902937	0.709917	0.618425
	b	33.8594	19.0386	10.5771

Table 8. Results of the Kolmogorov-Smirnov goodness-of-fit test for DoB sample 1 (Crown position−1st IPB loading).

Fitted distribution	Test statistic (d_n)	Critical value ($D_{n,\xi}$)		Test result	
		ξ = 0.05	ξ = 0.01	ξ = 0.05	ξ = 0.01
Beta	0.046707	0.1509	0.180844444	Accept	Accept
Birnbaum-Saunders	0.054485			Accept	Accept
Extreme Value	0.073507			Accept	Accept
Gamma	0.054384			Accept	Accept
Generalized Extreme Value	0.050741			Accept	Accept
Inverse Gaussian	NaN			-	-
Log-logistic	0.060637			Accept	Accept
Lognormal	0.053002			Accept	Accept
Nakagami	0.054241			Accept	Accept
Normal	0.0526			Accept	Accept
Rayleigh	0.575706			Reject	Reject
Rician	0.054097			Accept	Accept
Weibull	0.067876			Accept	Accept

Table 9. Best-fitted distributions for the DoB samples at the crown position of the central brace based on the results of the Kolmogorov-Smirnov test.

Best-fitted distributions	DoB samples		
	Sample 1 (1st IPB load case)	Sample 2 (2nd IPB load case)	Sample 3 (3rd IPB load case)
#1	Beta	Lognormal	Log-logistic
#2	Generalized Extreme Value	Inverse Gaussian	Generalized Extreme Value
#3	Normal	Birnbaum-Saunders	Lognormal

Table 10. Comparison of the test statistics for the proposed and the best-fitted distributions based on the results of the Kolmogorov-Smirnov test (Crown position of the central brace DoB samples).

	Test statistic		
	Sample 1 (1st IPB load case)	Sample 2 (2nd IPB load case)	Sample 3 (3rd IPB load case)
Best-fitted distribution	0.046707 (Beta)	0.069696 (Lognormal)	0.065531 (Log-logistic)
Proposed distribution	0.050741 (Generalized Extreme Value)	0.080025 (Generalized Extreme Value)	0.068212 (Generalized Extreme Value)
Difference	8.64%	14.82%	4.09%

Table 11. Comparison of the test statistics for the proposed and the best-fitted distributions based on the results of the Kolmogorov-Smirnov test (Toe position of the outer brace DoB samples).

	Test statistic		
	Sample 4 (1st IPB load case)	Sample 5 (2nd IPB load case)	Sample 6 (3rd IPB load case)
Best-fitted distribution	0.106385 (Extreme Value)	0.08399 (Generalized Extreme Value)	0.116099 (Extreme Value)
Proposed distribution	0.110175 (Generalized Extreme Value)	0.08399 (Generalized Extreme Value)	0.116984 (Generalized Extreme Value)
Difference	3.56%	0%	0.76%

Table 12. Comparison of the test statistics for the proposed and the best-fitted distributions based on the results of the Kolmogorov-Smirnov test (Heel position of the outer brace DoB samples).

	Test statistic		
	Sample 7 (1st IPB load case)	Sample 8 (2nd IPB load case)	Sample 9 (3rd IPB load case)
Best-fitted distribution	0.046671 (Generalized Extreme Value)	0.046882 (Generalized Extreme Value)	0.049635 (Generalized Extreme Value)
Proposed distribution	0.046671 (Generalized Extreme Value)	0.046882 (Generalized Extreme Value)	0.049635 (Generalized Extreme Value)
Difference	0%	0%	0%

INTERNATIONAL JOURNAL OF
COASTAL & OFFSHORE ENGINEERING IJCOE Vol.4/No. 2/Summer 2019 (31-39)

Available online at: http://ijcoe.org/browse.php?a_code=A-10-271-2&sid=1&slc_lang=en

Impact of Physical Properties on Distribution of Active Reaction in the Coastal and Offshore Areas of the Southern Caspian Basin

Siamak Jamshidi

Iranian National Institute for Oceanography and Atmospheric Science (INIOAS), Tehran, Iran; jamshidi@inio.ac.ir

ARTICLE INFO

Article History:
Received: 4 Jul. 2019
Accepted: 8 Sep. 2019

Keywords:
Caspian Sea
Seawater properties
Coastal process
Coastal and offshore area
Stability

ABSTRACT

Assessing the impact of physical properties on active reaction changes in the coastal and offshore area is one the most important aspect of marine environment of the Caspian Sea. Therefore, updated techniques and modern instruments have been used in order to evaluating the coastal and offshore area conditions. In the current research, collected data with spatial and temporal variety have been evaluated for investigation on seawater characteristics in the shallow and intermediate layers over the southern Caspian Sea. Some phenomena such as mixing, turbulence, water column stability and stratification are the effective elements on variability of physical and natural structures of the sea. Active reaction and dissolved oxygen as two properties of seawater are very important items for coastal engineering, piping in seabed, breakwaters and port constructions. Thus, in the current study, the above mentioned parameters were assessed over the southern shelf of the Caspian Sea. Vertical and horizontal variations of chemical characteristics such as active reaction of seawater were observed in several stations between coastal and offshore stations across surface, intermediate and deep layers. Results of the field operations showed that the normal values of pH in the study almost varied around 7.9-8 while during some seasons increased ore decreased more than 0.5 units due to human activates.

1. Introduction

The Caspian Sea, located between Europe and Asia continents, is the biggest semi-closed water body in the world. It is introduced by exclusive conditions, contains rich hydrocarbon mines, natural resources [1-4]. During the last decades, the large riverine water discharge containing various urban and industrial pollutants into the Caspian basins was characterized by reduced concentrations of oxygen, changing of active reaction and increased nutrient contents. Generally, enhancement in nutrient amounts due to increase in rivers inflow contents and reduce in severity of winter are main factors for insufficient ventilation of intermediate and deeper layers of the southern basin of the sea. On the other hand due to same reason the levels of active reaction through the water column show high variability in different time and seasons. Therefore, range of active reaction and dissolved oxygen in the seawater of southern basin is going to be inappropriate to the most marine organisms [5]. At the present time the marine environment of the Caspian Sea, especially south coastal and offshore area, is one of the deeply polluted water bodies in the region. The coastal and marine environment along the onshore and offshore areas of the southern border of the Caspian Sea is under stress because of extensive exploitation and discharge of great magnitudes of human wastes [2,6]. The main sources for pollutants entrance to the southern coastal area of the sea are consisted of industrial, agricultural and municipal wastewaters (pesticides and detergents), urban sewage waters, desalination industry project, heavy metals, petroleum products, and nutrients [2,3,6]. The above mentioned pollution is main threat to the environment, biodiversity and population of fish and animals of the sea. It is important to consider that the main flow of pollution approaches via coastal drainage and rivers to the sea [7]. Furthermore, the southern bay, coastal areas and offshore regions also have been contaminated by the anthropogenic sources [8]. In addition to the above mentioned factors, due to the special condition and chemical characteristics of the Caspian Sea water, active reaction value is significantly greater than in the waters of other regions in the World seas and oceans. The major reason for the high values of active reaction associated

to the great contribution of the riverine waters characterized by a high content of anions of weak acids, carbonic acid and pattern of distribution of hydro chemical aspects of the Caspian [5]. According to the physical and chemical conditions of the Caspian Sea, the investigation on seawater properties (such as active reaction…) is one of the most important necessities for safety level of marine environment and ecological characteristics in the southern boundary of the sea [9-10]. Under these conditions, it is vital and necessary to consider the increasingly physical and dynamical aspects of oceanography through the ecological and environmental studies of the sea water [4]. On the other side, field measurements and observations, data gathering and analysis of chemical and physical characteristics represent the interest for oceanography, ocean engineering and marine researches. According to the importance of properties of seawater of the Caspian Sea in the offshore and onshore regions, it is attempted to investigate the distributions of mentioned factors in the southern coastal waters and offshore sampling stations. Based on the fast variability of natural condition of seawater characteristics, and lack of sufficient accurate data and analysis in the literature that give careful information on monthly variations, the current study was programmed and performed. Aim of the research, is evaluation of temporal and spatial variability of active reaction in the Iranian coastal waters and offshore along the Caspian.

2. Methods

2.1Field Operation and Site

Field measurements have been made over the middle part of the southern continental shelf of the Caspian Sea. According to the geomorphologic characteristics, topography, and width of the shelf study area and sampling stations have been selected. The length of the Caspian Sea is about 1030 km between 36ºN and 48ºN and its width is around 200-400 km between 48ºE and 54ºE [11-13]. It is divided into three parts with maximum depths of 1025 m, 788 m and 20 m, respectively and average depth of 210 m [1,13-14]. Surface monitoring in the Caspian Sea showed that the northern part of the sea had largest diversity and productivity [15]. The main sources of freshwater inputs to the Caspian Sea are the Volga, Ural, Emba and Terek Rivers in the north part [16-17]. In the southern part, the total volume inflow of Iranian rivers to the sea is about 4-5%, which Sepidrood River with most contribution is distinguished [13,18]. Due to the isolation of the Caspian Sea from the open seas, its natural structure is under effect of external factors such as discharge of rivers and atmospheric processes. The hydrological structure and circulation of the Caspian Sea water are defined by these factors [19]. The southern coastal area of the Caspian Sea has warm summers and mild winters (warm and humid subtropical climate) [16,20]. Mean temperature in the southern coast of the Caspian Sea was reported about 16ºC, which varies from 4.5ºC in February to 27.5ºC in August [21]. For measuring seawater properties a portable CTD probe (Ocean Seven 316) developed by IDRONAUT was used. The probe was set in Timed Data Acquisition mode with one-second time intervals. Data collection was performed with profiler in free falling mode into the seawater column down to seabed with a time interval of one meter per second. The accuracy of pressure, temperature and conductivity sensors of Ocean Seven 316 probe was 0.05 full-scale, 0.003 ºC and 0.005 mS cm^{-1}, respectively. Dissolved oxygen and active reaction measurements were made using the oxygen sensor and pH meter of probe with the accuracy of 0.1 mg L^{-1}, 1% saturation and 0.01 pH. Dissolved oxygen levels of below 3 mg L^{-1} are stressful to most marine biota. Its levels of at least 5-6 mg L^{-1} are usually required for growth. In the southern basin dissolved oxygen content decreases with depth. Moreover, percentage of saturation reaches to 50% at level of 200 m and less than 10% at 600 m depth [20].

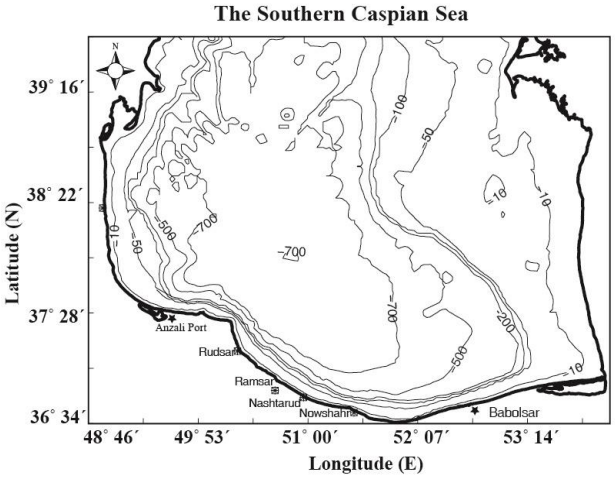

Figure 1. Study area located in the southern baundary of the Caspian Sea

2.1Computation and Modifications

During the sampling, the sensed parameters by CTD probe were calibrated by UNESCO formulas [22-23]. Due to the difference between the compositions of the Caspian Sea from the world ocean waters, some correction coefficients needed to be used. Some of the experimental, empirical and chemical equations were used for calculation of salinity and density of the Caspian Sea water. Millero and Chetirkin, (1980) carried out density laboratory measurements using some samples collected in the near shore surface waters of the southern part [24]. In the current research, the coefficients that were presented by Peeters et al., (2000) on IAEA data (1996) for calibration the salinity and density values is used [25-26].

$$S_{Caspian} = 1.1017 S_{CTD} \quad (1)$$

$$\rho_{Solution}(T,S,p) = \rho_{Sea}(T,0,p) + f(T,p)(\rho_{Sea}(T,S,p) - \rho_{Sea}(T,0,p)) \quad (2)$$

where,

- $\rho_{Sea}(T,S,P)$ is the density of water from UNESCO formulas using in situ temperature, pressure and salinity and $f(T,p)$ is the correction factor [22-23].
- $\rho_{Sea}(T,0,P)$ is the density of the water from UNESCO formulas using in situ temperature and pressure, S = 0 .

In computations presented by Peeters *et al.*, (2000) [25] for the ionic composition of the Caspian Sea and for S = 12.3, T = 25ºC and P = 0 was given by f = 1.0834.

International UNESCO Algorithm using in situ temperature, pressure and salinity, calculated from the following equation [22-23]:

$$\rho(T,S,p) = \frac{\rho(T,S,0)}{1 - \frac{p}{K(T,S,p)}} \quad (3)$$

Where, T is temperature, S is salinity and p is pressure, and K(T,S,p) is the secant Bulk Modulus can be calculated as follows:

$$K(T,S,p) = K(T,S,0) + Ap + Bp^2 \quad (4)$$

$$K(T,S,0) = K_W + (54.6746 - 0.603459T + 1.09987\times10^{-2}T^2 - 6.1670\times10^{-5}T^3)S + (7.944\times10^{-2} + 1.6483\times10^{-2}T - 5.3009\times10^{-4}T^2)S^{\frac{3}{2}} \quad (5)$$

$$A = A_W + (2.2838\times10^{-3} - 1.0981\times10^{-5}T - 1.6078\times10^{-6}T^2)S + 1.91075\times10^{-4}S^{\frac{3}{2}} \quad (6)$$

$$B = B_W + (-9.9348\times10^{-7} + 2.0816\times10^{-8}T + 9.1697\times10^{-10}T^2)S \quad (7)$$

Where K_W, A_W and B_W are the water terms as follows:

$$K_W = 19652.21 + 148.4206T - 2.327105T^2 + 1.360477\times10^{-2}T^3 - 5.155288\times10^{-5}T^4 \quad (8)$$

$$A_W = 3.239908 + 1.43713\times10^{-3}T + 1.16092\times10^{-4}T^2 - 5.77905\times10^{-7}T^3 \quad (9)$$

$$B_W = 8.50935\times10^{-5} - 6.12293\times10^{-6} \times 10^{-8}T^2 \quad (10)$$

Where, $\rho(T,S,0)$ is density of sweater at p=0 calculated from the following equations:

$$\rho(T,S,0) = \rho_W = (8.244493\times10^{-1} - 4.899\times10^{-3}T + 7.6438\times10^{-5}T^2 - 8.2467\times10^{-7}T^3 + 5.3875\times10^{-9}T^4)S + (-5.72466\times10^{-3} + 1.0227\times10^{-4}T - 1.6546\times10^{-6}T^2)S^{\frac{3}{2}} + 4.8314\times10^{-4}S^2 \quad (11)$$

$$\rho_W = 999.842594 + 6.793952\times10^{-2}T - 9.095290\times10^{-3}T^2 + 1.001685\times10^{-4}T^3 - 1.120083\times10^{-5}T^4 + 6.536332\times10^{-9}T^5 \quad (12)$$

In above mentioned equations, T temperature, S salinity, p pressure. For more information see (UNESCO 1981a, 1981b) [22-23]. Density is generally written in terms of Greek lowercase letter sigma-t as follows [27]:

$$\sigma_t = \rho(T,S,p) - 1000 \quad (13)$$

For computation of water column stability the following equations were used. Which N is named Brant-Vaisala Buoyancy Frequency.

$$E = -\frac{1}{\rho}\left(\frac{\partial\rho}{\partial z}\right) - \frac{g}{c^2} \quad (14)$$

$$N = (gE)^{1/2} \quad (15)$$

3. Results and Discussion

3.1 Physical structure

The surface water temperature over the continental shelf reached a maximum of 29ºC in summer and then, in accordance to the reduction of air temperature due to climate changes in the region, it decreased gradually to 20 ºC at the beginning of autumn (October) and 11.5 ºC in the middle of winter. With increasing temperature of surface waters in consequence of enhancement of the air temperature in early spring, vertical gradient of temperature in the water column is increased. Therefore, the thermal stratification of the water column is established through the water column in the spring season. In May, three layers in the water column over the continental shelf including a thin mixed surface layer, thermocline, and deeper water are formed. It is assumed that thermal stratification developed in the summer season and became stable in midsummer (August) [28]. A strong seasonal thermocline with a thickness of about 30 m is located between depths of 20 and 50 m. The 27.5ºC temperature above the thermocline decreases to 10.5ºC below it. In the mixed surface layer, the temperature ranges between 28.5ºC at the water surface to 27.5ºC above the thermocline in a depth of20 m. Below the thermocline, the temperature decreases gradually to 8.5 ºC at 80 m depth and 7 ºC at 160 m depth. In the beginning of autumn (October), the thickness of the thermocline reduced to 15 m and thermocline was located between 45 m and 60 m depths. Below thermocline, deep water is located with 2 degree vertical temperature gradient. The water body on the shelf is mainly located in the surface mixed layer and only a limited area below 60 m depth over the shelf break includes the thermocline layer. A comparison between vertical temperature structures in summer and autumn indicate that, the top level of thermocline has fallen

from 20 m depth to 40 m depth over and outside of the shelf. In autumn, the thickness of the thermocline has decreased substantially in comparison to that in summer (as it is shown in the contour plot of the vertical structure of temperature in transect). In comparison between physical structure between summer (August) and autumn (October), the temperature and thickness of the surface mixed layer in October decreased about 9 ºC and 20 m respectively, indicating the deepening of the surface mixed layer due to seasonal climate changes. Over the continental shelf, the upper layer of the surface water was completely mixed with a temperature of 20-19.5ºC with no horizontal gradient across the continental shelf.

3.2 Stability and Layering of Water Column

Based on the collected data and comparison with other previous studies, thermal stratification of seawater column showed three layers in the water column, in offshore stations, consisting of surface mixed layer, thermocline, and deep water. A sharp seasonal thermocline was visible between 20-50 m depths with around 15 degree which temperature decreasing across it [28]. Below the thermocline layer, water temperature varied between 11ºC and 7ºC around 150 m depth. The highest surface water temperature was observed in summer (around 29ºC) while the lowest surface water temperature was recorded in winter season (around 9ºC). The most variations of seawater parameters were observed through the mixed layer and thermocline. Below the layer of 100 m depth, monthly variations of the seawater characteristics were slight. By comparing vertical profiles, the correlation between variations of temperature and density was clearly seen. Seasonal stratification patterns and variations of thermohaline at the deepest sampling station far from the coasts were clearly observed. The sharpest thermocline was observed in the summer season, it moved down to around 40 m during autumn and after that disappeared in winter [28. The higher seasonal variations of water salinity were detected from the surface to 50 m depth in the spring–autumn periods. Based on the collected data in June showed that the water salinity changes continue from sea surface to lower than 150 m depth. It is assumed that seasonal changes of pycnocline followed the pattern of seasonal variations of thermocline. Forming the pycnocline started from spring season together thermocline in the study area. Pycnocline was in a strong situation in summer located in position of thermocline and deepened to 40 m in autumn. Vertical structures of temperature and density in the times of measurements in June and August were approximately similar. Vertical profile of water temperature in deepest station illustrated that the water temperature in water column in upper layer was approximately uniform. The natural regime of structures of seawater parameters in the Caspian Sea is under effect of external factors such as riverine runoff and atmospheric activity. Study on the mentioned factors shows that they define a rapid and significant variability in the hydrological structure and circulation of the waters of the Caspian Sea relative to the other open seas. Therefore, comprehensive monitoring of the natural environmental conditions of the Caspian Sea and changes in its main parameters is necessary [5].

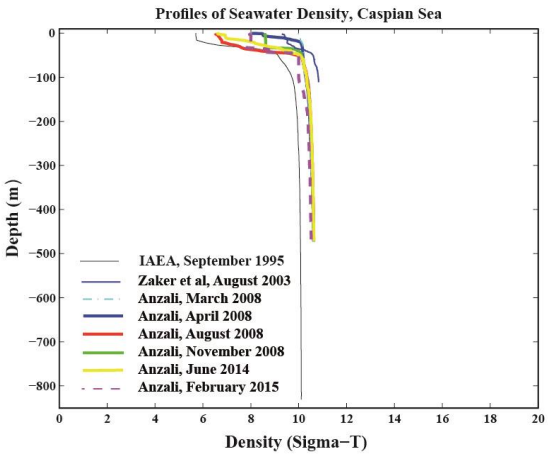

Figure 2. A sample of vertical structure of water density

Structure of the physical properties of the Caspian Sea water is corresponded to the various factors such as atmospheric effects and freshwater discharge in different times. So, it is expected that the vertical structure and stratification of the Caspian Sea water column is different. Vertical structure of temperature in the time of measurements in March and February (winter) shows rapid changes from surface to near bottom layer. The cause of this phenomenon is lower vertical gradient of temperature in water column relative to the other vertical profiles in other seasons. In winter difference in temperature between surface layer and near bottom layer is low. In the other hand, there is no strong thermal stratification in water column and the changes of temperature are rapid. This point is important that, due to increase in speed and severity of wind over the region in winter, kinetic energy and turbulence in water column increase. Thus water column is mixed with rapid temperature profile. Based on the results, the maximum values of stability frequency can be seen in upper layer including surface mixed layer and thermocline (pycnocline) [28]. Oscillation of data in the time of measurements in June was considerable. Maximum value of frequency was observed at the boundary of upper layers in February. Frequency of stability in deep layer was very slight in February. Variations of stability frequency in deep layer in June were more than its variations in February [28].

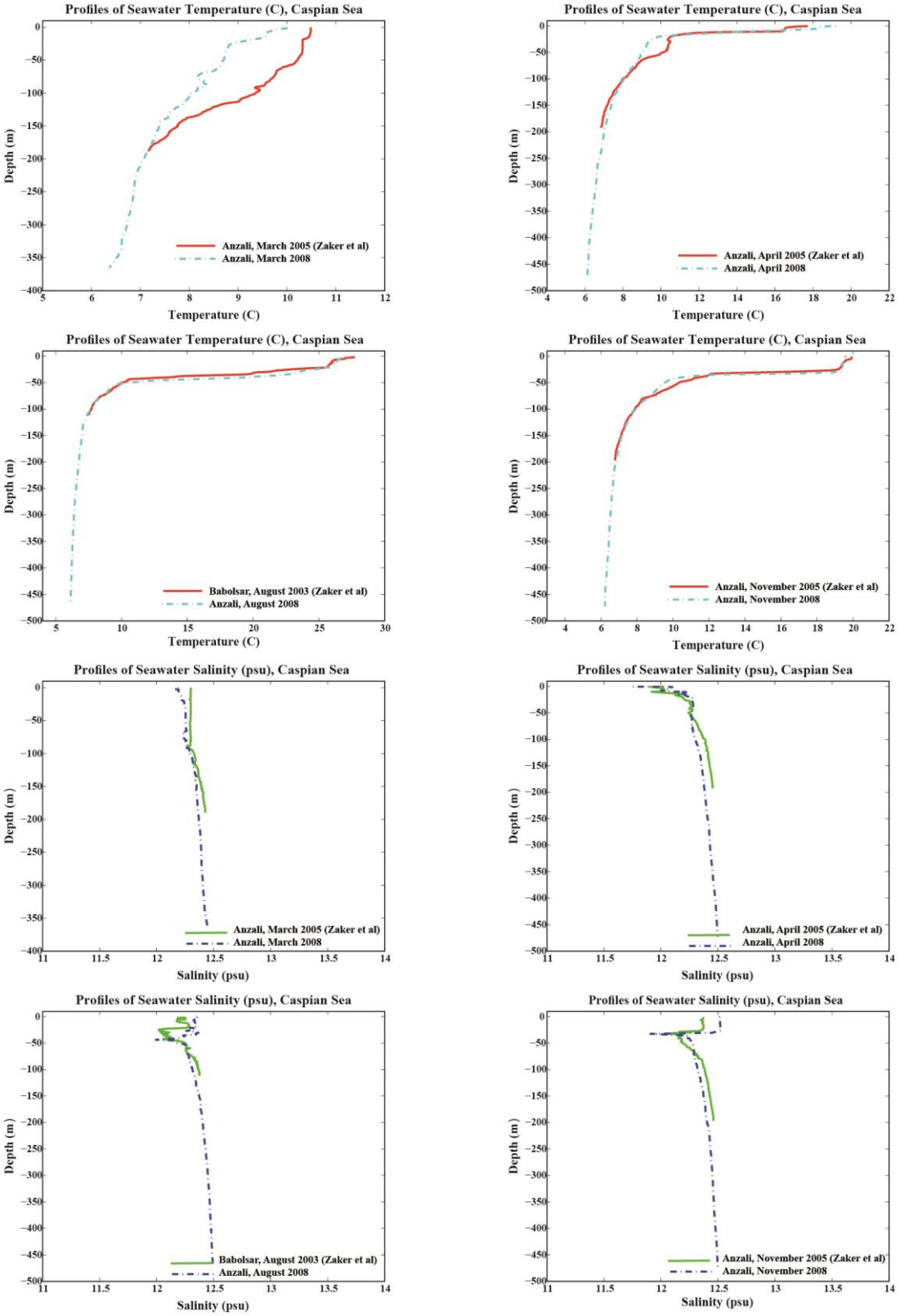

Figure 3. Comparison of physical properties of the Caspian seawater in varoius field operations

3.3. Active Reaction and Oxygen

Variability of seawater properties such as active reaction (pH) and oxygen and saturated values are very important from view point of oceanography. Therefore, it is tried to evaluate the mentioned factors changes in the study area over the continental shelf zone in front of Nowshahr.

Based on some of the previous researches, natural changes in structure of hydrodynamics and hydro physic (thermohaline) in seawater can affects the multi-annual trend of variations in the active reaction amounts. Some parameters such as temperature and turbulence of seawater layers have important role on its vertical structure changeability in the south Caspian Sea.

Variability of pH along a transect perpendicular to the coast line in the study area from March 2014 to February 2015 were evaluated. In late winter (March),

changes of active reaction were detected between 8.2 and 8.6 at the upper layer, which decreased with depth. Amount of active reaction ranged around 8.2 below 30 m depth until depth of 60 m. collected data showed that the value of pH at depth of 110 m was measured around 8. At this time, variations of active reaction from the surface to the bottom were not uniform. Regarding to recorded data in April, vertical and horizontal gradients of active reaction was considerable above 70 m depth. At the sea surface, values changed from 8.2 to 8.4 and reached to 8 near 140 m depth. pH values decreases with increase depth over the southern shelf. Observed values from upper layer in April were relatively less than measured values of pH in late winter (March). In May 2014, vertical structure of active reaction along the survey line showed values of 8.2 to 8.3 over the continental shelf, which the values reached to more than 8.4 amounts toward the deeper stations. Outside the shelf active reaction from 8.2 at surface layer reduced to 8.4 at 90 m depth. Distribution of pH in vertical direction showed a decrease with depth. During measurement in June, values of pH changed between 8.6 and 8.8 along transect, and reached to 8.7 around 120 m depth across intermediate layer. Above 100 m depth, active reaction was uniformly varied (mainly about 8.8) outside the shelf break (off shore stations). In mid-summer (August), collected data by the probe showed that the active reaction ranged around 8.1 across the surface mixed layer and thermocline. Below thermocline, values decrease with depth and reached to 8 at depth of 80m in water column. In September, values at the beginning and middle of transect were around 8.1 over the continental shelf and there was no considerable changes during surface mixed layer. In the time of observation, amount of pH ranged around 8.2 at the end of transect. Over the continental shelf zone, distributions of pH at the sea surface were under effect of mixing. With a comparison, it can be seen that active reaction variations at the surface layers were more than near bottom layers (7.8 at depth of 140 m). It is assumed that, the rivers outflow was one of the most important reasons for changing pH regime in shallow waters stations. Values of active reaction across surface mixed layer in autumn (October) were uniform with a value of 8.1. In deeper layers below surface mixed layer pH of sea water was detected about 8. At the time of measurements, below depth of 50 m depth active reaction decreased with depth and reached 7.9 at depth of 100 m. It is assumed that in the time of measurements in January, human activities such as leakage of waters and other materials from the ships in anchorage area of Nowshahr Port or operation of transfer and discharge the sediments of harbor basin into this area disturbed the natural structure of active reaction in the region. Thus, contours with high values of pH were observed in a distance of 11 km from the beginning of transect. Along transect, amounts of pH were mainly around 10.0 in shallow waters stations and increased to 8.4 over the shelf. Outside the shelf, active reaction measured about 9.3 at surface decreased to 8.7 in deep-water. In mid-winter (February) active reaction was measured 7.8-7.9 over the continental shelf region and out of shelf. At this time of measurements, values were around 8 over the shelf break. Below depth of 50 m active reaction decreased from 7.9 at 70 m level to value of 7.8 below 100 m depth. In February, contour of pH was parallel to sea water level and horizontal gradient of active reaction was very slight.

Based on the Russian research projects in the Caspian Sea, climatic fields of the active reaction in surface layer in winter were about 8.55 and in summer were more than 8.45 near the current study area. In addition, their results of the climatic fields at intermediate layer (100 m level) were about 8.35 and more than 8.275 in aforementioned seasons, respectively. Bruevich for the first time in year of 1937 showed that the levels of pH in the Caspian Sea are further than that in the waters of the World open seas and ocean [29]. The major important reason of the high values of pH was reported in riverine discharge in the north and south parts of the Sea [5]. In the intermediate layer, values of pH were similar to active reaction amounts in late winter (March) and early spring (April). Decrease trend of values in aforementioned seasons continued with depth. In midsummer, amounts of active reaction in the intermediate and deep water layers were less than that in late winter and early spring. In contrast, background values of summertime pH of seawater were lower than winter and spring. This is clearly confirmed by results of [5] in the southern basin of the Caspian Sea. In north of the Caspian Sea values of pH is under effect of rivers discharge while in southward direction increase of pH is caused by the effect of temperature enhance [30]. An analysis on vertical structure of pH in deep water stations in November showed that amounts of pH in mid-autumn was more than that in other seasons both in intermediate and deep layers [30]. By the comparison of the results analysis on data, local issues and human activities varies the natural configuration of active reaction distribution. The rivers discharge, port activities and exchange water between bay and lagoon with the coastal waters can be presented as important sources for entrance the urban and industrial wastes. Therefore the mentioned pollutants inflow to the coastal waters and far from the coast can changes the natural regime of chemical properties including active reaction and environmental parameters of the seawater. It noted to remember that intensive production processes also effect on the pattern of active reaction [5].

Several oceanographic studies based on field measurements have been were carried out in the region [31-33]. The mentioned works were focused

either on changes of seawater properties at the surface or were done at a short duration in of the southern coastal waters of the Caspian Sea. Considering the fast variability of the natural pattern of seawater properties and hydrodynamics of the Caspian, enhanced inflow of pollutants and development of gas and oil industries, comprehensive oceanographic and environmental studies for evaluate the Caspian Sea situation is required [13,6,19].

Analysis of physical properties data showed that the structure of seawater properties in onshore areas and offshore stations was not exactly similar. Over the continental shelf, seawaters were mainly located through the surface mixed and thermocline layers in all seasons. By comparing on the vertical structure of physical characteristics over the continental shelf during various months, it seems that the effect of local and coastal characteristics in shallow waters stations were dominant.

Changes of the salinity near the bottom were less than surface layers. Thermohaline structure in this area was under the effect of air sea interaction factors such as rain and wind. Density variations at the sea surface, was correlated with salinity due to entry of less saline waters in the continental shelf while in lower layers temperature was the effective factor in monthly variations of the density. The forming of the stratification, mixed surface layer developed during March and April. Vertical gradient of salinity during spring was higher than in winter. Results of the comparison between winter time and summer measurements of seawater indicated that the water was both colder and denser in winter than in summer. Salinity in surface mixed layer was observed to be higher than salinity across the thermocline, which could be due to evaporation intensity effect. The average salinity in the surface mixed layer and thermocline was higher than in winter and spring.

An investigation on vertical structure of the salinity showed that its values increased with depth throughout the whole seasons. Seasonal changes of the salinity were limited above the 100 m depth. The density of seawater in offshore area is determined by temperature field (70-80%) as well as the effects of outflow of the freshwater defined by salinity [19].

In the southern coastal waters of the Caspian Sea formation and destruction of seasonal thermocline (and pycnocline in position of thermocline) occurs during the period of early spring to late autumn [28]. Thus, it is expected that during this time the pycnocline prevent the ventilation of the deeper layers [28]. Thus, as a result the concentrations in the near bottom layers reduce. The lowest values of dissolved oxygen concentrations were recorded below 100 m level. Variations of dissolved oxygen concentrations in various times of measurements were minor. In winter due to mixing in water column especially in upper 100 m depth, dissolved oxygen content was uniform, relative to August and November. The maximum vertical gradient of dissolved oxygen concentrations for the entire water column from the sea surface to bottom (12.5 mgL^{-1}) were observed in June. The regime of dissolved oxygen in shallow waters (over the continental shelf) differed from that through intermediate layer. The dissolved oxygen concentrations decreased with depth in the investigated area. This reducing trend is confirmed by the results of previous measurements in the Caspian Sea [20].

Regarding to the previous data collection; distribution of dissolved oxygen along deep water transect in the first month of summer showed a range of variation between 2.5 and 1.5 mgL^{-1}. In the offshore area, concentrations of dissolved oxygen were about 8.5 mg L^{-1} and reached 12.5 mgL^{-1}, below 50 m depth. Below this level, dissolved oxygen gradually reduced with depth and reached 9.5 mgL^{-1} at level of 100 m. In deeper layers (below 100 m depth), dissolved oxygen concentrations in July reached values of 3.5 mgL^{-1} [5,34]. Outside the shelf, values of dissolved oxygen changed between10.5 mgL^{-1} at the sea surface and about 10 mgL^{-1} at 100 m depth. The concentrations of oxygen in lower layers reached to 8.5 mg L^{-1} at 150 m depth. In General, concentrations of dissolved oxygen decreased with depth in offshore area in June and February [34]. As a result of analysis on observed data, saturated oxygen in deep water transects the concentrations in deeper layer and intermediate is insufficient for fish and other marine organisms [5,4].

Based on the results of some of the previous studies in the southern boundary of the Caspian Sea such as Zaker et al., 2007, Zaker 2007, Nezlin 2005 and Nasrollahzadeh et al., 2008, discharge of pollutants consists of urban, industrial and agricultural wastewaters, municipal domestic sewage, pesticides, detergents, and nutrients into the Caspian Sea, treat its marine environment. These materials decrease the biodiversity and natural biological resources in the sea. Increased amounts of phytoplankton in water bodies in reaction to the enhancement of nutrient supply can have severely damaging effects on the marine organisms. It is possible that low values of dissolved oxygen concentration in deeper parts and strong stratification in water column together happening of algal bloom phenomena present dangerous results for Caspian ecosystems. Zaker (2007) expected this phenomenon in previous studies in southern Caspian Sea.

Generally, values of pH in deep water zone in the study area reduced with depth. In a previous research, climatic fields of the active reaction in surface layer in winter about 8.55 and in summer were more than 8.45 near the current study area. In addition, their results of the climatic fields at intermediate layer were about 8.35 and more than 8.275 in aforementioned seasons, respectively. Bruevich in 1937 for the first time

showed that the values of active reaction in Caspian Sea were more than waters of World Ocean. The most important reason of the high values of active reaction was reported in riverine discharge into the Caspian Sea [5]. In intermediate layer values of pH were similar to active reaction amounts in winter (February). Decrease trend of values in aforementioned time continued with depth. In June, amounts of active reaction in the intermediate and deep water layers were more than that in February. In north of the Caspian Sea values of pH is under effect of rivers discharge while in southward direction increase of pH is caused by effect of temperature enhance [5]. Based on analysis additional information of research project performed by Roohi et al., 2008 and Tuzhilkin et al., 2005, local factors and human activities changed the natural structure of active reaction. At the last decades, increasing in the entrance of urban and industrial wastes into the coastal zone changed natural regime and normal mode of chemical properties. It is important that intensive production processes also effect on the structure of pH in the Caspian Sea [5]. Therefore, cooperation and commitment of the all countries to reduction entrance of the pollutants to the sea has high level of importance. So, the Caspian Sea requires to progressive plans and certain measures for improve the water quality and decrease levels of pollution in the marine environment.

5. Conclusions

The impact of physical properties on active reaction changes in the coastal and offshore area was analyzed. The values of active reaction and oxygen are two important chemical factors for quality control of seawater and evaluating the safety level of coastal and open sea areas. The output of the current research gives a preliminary view and basic information on vertical configuration of variability of seawater characteristics in the southern region during the year. By the comparison and analysis the collected data, it can be seen that the characteristics of the Caspian offshore area were different in comparison to the coastal waters. The inter-annual variability of formation and destruction of the thermocline and physical structure of water column affect the distribution of can change active reaction and oxygen in seawater. Moreover, for get a good knowledge of monthly and seasonal variations in levels of active reaction and saturated oxygen understanding and study of physical structure of water temperature is needed as well as current pattern.

To achieve a clean marine and coastal environment and ecosystem, one of the most fundamental actions is to prevent the entrance of urban and village water waste in the rivers and coastal waters. The release of large amounts of industrial, agricultural and urban wastes threats the marine ecosystems in the onshore and offshore region. Also, transferring sediment by the dredger ships from harbor to the offshore area changes the natural pattern of active reaction in water column. If the conditions continue, with elevation of pollutants and nutrient contents in seawater, average of dissolved oxygen concentrations in the deeper layers of the Caspian Sea was reduced. Its consequence is the forming of death area in deeper parts of the water column. Finally, the results indicated the need of serious efforts for reducing entrance of urban and industrial wastes and pollutants into the coastal and offshore areas.

Acknowledgment

The research projects was supported by Iranian National Institute for Oceanography and Atmospheric Science (Project No. 396-012-01-020-05).

6. References

1- Dumont, H.J., (1998), *The Caspian Lake: History, biota, structure, and function*, Limnology and Oceanography, Vol. 43(1), p. 44–52.

2- Zonn, I.S., (2005a), *Environmental Issues of the Caspian*, Caspian Sea Environment. Springer-Verlag, Berlin, Heidelberg, Handbook of Environmental Chemistry. p. 223-242.

3- Zonn, I.S., (2005b), *Economic and International Legal Dimensions*, Caspian Sea Environment. Springer-Verlag, Berlin, Heidelberg, Handbook of Environmental Chemistry. p. 243-256.

4- Kosarev, A.N. and Kostianoy, A.G., (2005), *Introduction*, The Caspian Sea Environment. Springer-Verlag, Berlin, Heidelberg, Handbook of Environmental Chemistry. p. 1-3.

5- Tuzhilkin, V.S., et al., (2005), *Natural chemistry of Caspian Sea waters*, The Caspian Sea environment, Springer-Verlag: Berlin, p. 83-108.

6- Korshenko, A.N. and Gul, A.G., (2005), *Pollution of the Caspian Sea*, The Caspian Sea environment, Springer-Verlag: Berlin, p. 109-142.

7- Aladin, N. and Plotnikov, I., (2004), *The Caspian Sea*, Lake Basin Management Initiative Thematic Paper.

8- Kideys, A.E., et al., (2008), *Increased chlorophyll levels in the Southern Caspian Sea following an invasion of Jellyfish*, Research Letter Ecology, Hindawi Publishing Corporation, p. 1-4.

9- Nezlin, N.P., (2005), *Pattern of seasonal and interannual variability of remote sensed chlorophyll*, The Caspian Sea environment, Springer-Verlag: Berlin, p. 143-157.

10- Zaker, N.H., (2007), *Characteristics and seasonal variations of dissolved oxygen*, International Journal of Environmental Research, Vol. 1(4), p. 296 301.

11- Zenkovich, L.A., (1963), *Biology of the seas of the USSR*, Nauka, Moscow.

12- Klig, R.K. and Myagkov, M.S., (1992), *Change in the water regime of the Caspian Sea*, GeoJournal, Vol. 27(3), p. 299-307.
13- Kosarev, A.N., (2005), *Phsico-Geographical Conditions of the Caspian Sea.* The Caspian Sea Environment. Springer-Verlag, Berlin, Heidelberg, Handbook of Environmental Chemistry. p. 5-31.
14- Giralt, S., et al., (2003), *Cycle water level oscillations of the KaraBogazGol-Caspian Sea system*, Earth and Planetary science letters, Vol. 212, p. 225-239.
15- Kasymov, A. and Rogers, L., (1996), *Ecological description of the southern Caspian Sea in the oil-field region of Guneshly*, Political and Ecological Studies, Vol. 22(3&4), p. 83-93.
16- Rodionov, S.N., (1994), *Global and regional climate interaction: the Caspian Sea experience*, Water Science and Technology Library, Kluwer Academic Publisher, Dordrecht. p. 241.
17- Mamedov, A.V., (1997), *The late pleistocene-holocene history of the Caspian Sea*, Quaternary International, Vol. 41/42, p. 161-166.
18- CEP (Caspian Sea Environmental Programe), (2002), *Transboundary Diagnostic Analysis for the Caspian Sea*, Baku, Azerbaijan, p. 36.
19- Tuzhilkin, V.S. and Kosarev, A.N., (2005), *Thermohaline Structure and General Circulation of the Caspian Sea Waters*, Caspian Sea Environment. Springer-Verlag, Berlin, Heidelberg, Handbook of Environmental Chemistry. p. 33-57.
20-Kosarev, A.N. and Yablonskaya, E.A., (1994), *The Caspian Sea.* SPB, TheHauge. p. 274.
21- Asadullayeva, E. and Alekperov, I., (2007), *Free-living ciliates of the Anzali Wetland of the Caspian Sea*, Turkish Journal of Zoology, Vol. 31, p. 143-149.
22- UNESCO, ICES, SCOR, IAPSO, (1981a), *Background papers and supporting data on the International Equation of state of Sea Water 1980*. UNESCO technical papers in marine science, Vol. 38.
23- UNESCO, ICES, SCOR, IAPSO, (1981b), *Background papers and supporting data on the practical salinity scale 1978*. UNESCO technical papers in marine science, Vol. 37.
24- Millero, F.J. and Chetirkin, P.V., (1980), *The density of the Caspian Sea waters*, Journal of Deep-Sea Research, Vol. 27A, p. 265-271.
25- Peeters, F., et al., (2000), *Analysis of deep-water exchange in the Caspian Sea based on environmental tracers.* Journal of Deep-Sea Research, Vol. (1) 47, p. 621-654.
26- IAEA, (International Atomic Energy Agency), (1996), Research/Training on the Caspian Sea, Data Report 1995, Vienna, p. 95.
27-Knauss, J.A., (1997), *Introduction to Physical Oceanography*, United States of America: wavel and press Inc., Vol. 1, p. 309.
28- Jamshidi, S., (2017), *Assessment of thermal stratification, stability and characteristics of deep water zone of the southern Caspian Sea*, Journal of Ocean Engineering and Science, Vol. 2, p. 203–216.
29-Bruevich, S.V., (1937), *Hydrochemistry of the Middle and South Caspian.* AN SSSR, Moscow (in Russian).
30- Tuzhilkin, V.S. and Kosarev, A.N., (2004), *Long-term variations in the vertical thermohaline structure in deep-water zones of the Caspian Sea*, Water Resources, Vol. 31(4), p. 376-383.
31- Zaker, N.H., et al., (2007), *Physical study of the southern coastal waters of the Caspian Sea, off Babolsar, Mazandaran in Iran*, Journal of Coastal Research, Vol. SI 50, p. 564-569.
32- Nasrollahzadeh, H.S., et al., (2008), *Trophic status of the Iranian Caspian Sea based on water quality parameters and phytoplankton diversity*, Continental Shelf Research, Vol. 28, p. 1153-1165.
33- Roohi, A., et al., (2008), *Impact of a new invasive cctenophore (MnemiopsisLaiyi) on the zooplankton community of the Southern Caspian Sea*, Marine Ecology. Vol. 29, p. 421-434.
34- Jamshidi, S., (2011), *Variability of Dissolved Oxygen and Active Reaction in Deepwater of the Southern Caspian Sea, Near the Iranian Coast*, Polish Journal of Environmental Studies, Vol. 20(5), p. 1167-1180.

INTERNATIONAL JOURNAL OF
COASTAL & OFFSHORE ENGINEERING IJCOE Vol.4/No. 2/Summer 2019 (41-46)

Available online at: http://ijcoe.org/browse.php?a_code=A-10-96-3&sid=1&slc_lang=en

The Tropical Cyclone Tracks and Formation over the Western Indian Ocean, And Impacts on the Iranian Southern Coasts

Mojtaba Zoljoodi[1,2]

[1]*Iranian National Institute for Oceanography and Atmospheric Sciences, Tehran, Iran; zoljoodi@inio.ac.ir*
[2]*Atmospheric Science and Meteorological Research Center*

ARTICLE INFO

Article History:
Received: 21 Jul. 2019
Accepted: 16 Sep. 2019

Keywords:
Tropical Cyclone Tracks
Coastal infrastructures
Mokran region
Cluster analysis
Atmospheric conditions

ABSTRACT

Cyclones are as one of the most dangerous meteorological phenomena of the tropical region that generate strong winds and heavy rainfall, impacting coastal regions. Behavior of tropical cyclone trajectories needs to be better understood in order to find predictable aspects of landfall potentially. This research aims to analyze the cyclone tracks statistically and then study of the associated meteorological effects of Gonu cyclone in June 2007 as an example. Using the cluster analysis (K-mean method) 5 principal clusters have been derived and spatial – temporal studies including the monthly variation of cyclone trajectories and their intensity and frequencies are performed. The 4th cluster indicated more spatial variability and expansion (4º-31ºN and 48.5º-78ºE). The second cluster showed the highest frequency with 349 events as well as the highest maximum intensity and standard deviation of 235.2km/h and 47.96km/h respectively. During 1-7 June 2007, the Gonu super cyclone traversed the Arabian Sea and reached the Iranian southern regions affecting the coastal infrastructures and communities. In this 7-day period the daily composite maps of different atmospheric levels showed that by intensifying of Gonu cyclone the axis of subtropical high pressures in the lower levels moved to the east and in the 500hp level they moved to the northward over the study region.

1. Introduction

Tropical cyclones are low pressure systems that have thunderstorm activity and rotate counterclockwise. Tropical cyclones form over all tropical oceanic areas except the South Atlantic and the Southeast Pacific. A tropical cyclone (TC) is a synoptic-scale to meso-scale low-pressure system over tropical or subtropical waters with organized convection and definite cyclonic surface wind circulation. TCs have significant impacts on the weather and climate of tropical countries (Riehl, 1979). Their frequency and intensity in the North Indian Ocean is very important for the maritime regions of South Asia.

TCs imply significant threat to communities that lie in their paths, so improving our understanding of TC formation, track and intensity is of significant importance. Annually, about 30% of global TCs form in the Southern Hemisphere (Neumann et al. 1993), spanning a large area from the western Indian Ocean to the central Pacific and covering three TC basins: the southwest Indian Ocean (West of 90E), the Australian Region (90–160E) and the South Pacific Ocean (East of 160E). Genesis location of TCs can be linked to the seasonality, sea surface temperature, wind shear, and position of the initial disturbance (Gray 1968; Henderson-Sellers et al. 1998). According to a research developed by Evan and Camargo (2011), November cyclones primarily form during periods when the Bay of Bengal experiences a broad region of high sea level pressure, implying that November storms form in either the Arabian Sea or the Bay of Bengal but not in both during the same year. Additionally, the analysis of changes in a genesis potential index suggests that long-term variability in the potential for a storm to form is dictated by changes in midlevel moisture. Landfall and the intensity of the storm at landfall are also associated with genesis location and track shape (Camargo et al. 2007).Ramsay et al. (2011) performed an investigation on a probabilistic clustering method to describe various aspects of tropical cyclone tracks in the southern hemisphere, they found ENSO has a significant effect on mean genesis location in three clusters with TCs forming further equator-ward during El Nino (La Nina) in addition to large shifts in mean longitude. They found that the Madden Julian Oscillation has a strong influence on TC genesis in all clusters. Cluster analysis provides a way to

objectively classify storms in a given ocean basin into subcategories depending on geographical properties of the storms (e.g., genesis, track location, and shape). Such classification can become useful for building predictive understanding on climatic time scales. The K-means method (MacQueen 1967) is a common clustering method that has been used both with tropical and extra-tropical cyclone tracks.

In the present investigation we have considered initially the TC frequencies in monthly and yearly scales over the western Indian Ocean and the Arabian Sea, and then using the k-means method the TCs have been clustered based on their coordination (x,y) into 5 main groups. They have been analyzed regarding their intensities, and then we studied the associated physical and dynamical parameters in the atmospheric levels during the Gonu super cyclone (1-7 June 2007) over the study region. All TC datasets are gathered from The International Best Track Archive for Climate Stewardship (IBTrACS) in 6-hourly resolution over the study area in 1990-2013.

2. Results

2.1 Statistical Analysis

The tropical cyclone(TC) frequencies showed an annual average of TC events about 44 in the investigated 24-year period (1990-2013), and the maximum and minimum values were 123 in 2004 and 8 in 2000 respectively. The inter-annual (seasonal) distribution of TC frequency confirmed that the tropical storms are active during per and post monsoon periods over the Arabian Sea and Western Indian Ocean (Fig.1). During pre- and post-monsoon periods of May–June and October–November respectively, the equatorial position of the Somali Jet and broad region of positive vorticity values, coupled with warmer regional ocean temperatures provide a larger favorable region for storm development. In winter months because existing of the minimum temperature on the sea surface there is not sufficient condition to storm genesis. Monthly tropical storm duration indicated the maximum values of 14, 11 and 9 days in November 2011, October 1998 and June 2007 respectively. In total, stormy days duration over post-monsoon period could be higher than per-monsoon, as in October and November the two-month average of long term storm duration was about 50 days, while for May and June it is reached about 41 days (Fig.1).

A long term spatial intensity analysis of the TC records illustrated the most severe storms (by 148.16-235.2 km/h)in two tracks with opposite directions over the study area, as the both of them originated from the same position as follows: 15º-20º N and 65º-70º E, and then the storms move on in two separate tracks toward northwest and northeast. In the case of land-falling they may hit the eastern shores of Oman (by the northwestern track) and the northwestern shores of India and southern Pakistani beaches (by the northeastern track). Surrounding the mentioned two main tracks there are the relatively weak storms (by 92.6-148.16 km/h)and also over an area shaped as a triangular among them, with front angle is oriented southwards, and the base line set northward we found a calm region with no storms or disturbances (it is shown with dark line on Fig.2.).

Cluster analysis classified the TC dataset into 5 different groups based on the location variances of each group. The cluster 2indicates the highest TC frequency with 349 events and in the next ranks the clusters 1, 5, 4 and 3 are represented by 265, 190, 145 and 113 events, respectively. In an inter-annual outlook, for all clusters in winter months and partially in summer there is the lowest cyclone frequency, whiles the highest ones are found for cluster 1 at October (88 events), cluster 2 and 4 at May (101 and 36 events), cluster 3 and 5 at November (61 and 77 events). Regarding the monthly median values it is remarkable that for the clusters 1, 3 and 5 the main portion of TC frequency has been happened in autumn season, but for the clusters 2 and 4 they have been distributed equally in the first and second half of year (Table 1).

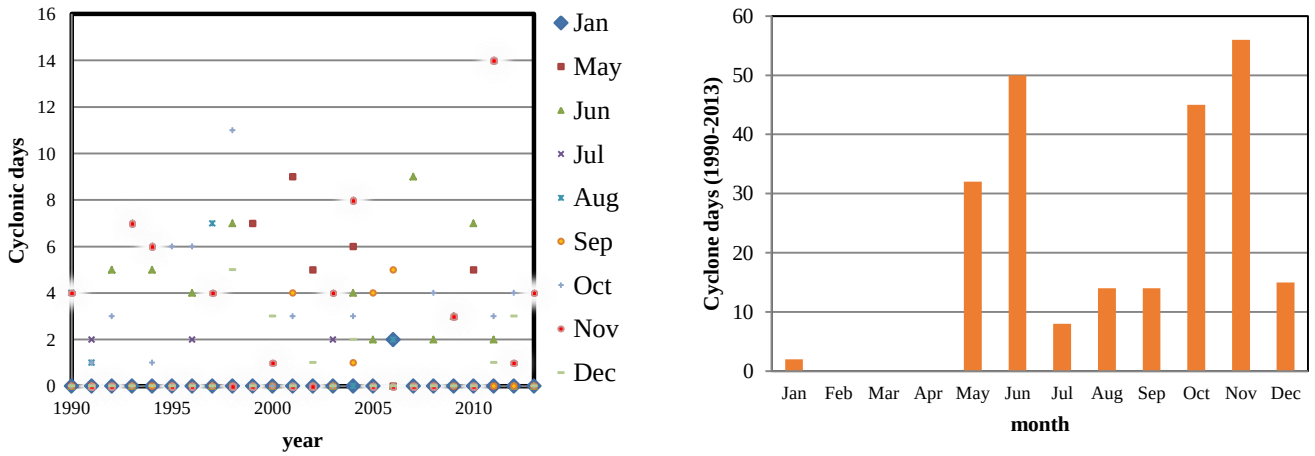

Figure 1. Monthly scatterplotof cyclonic storm days (CS-days=storm duration) over the Arabian Sea for each year in the period 1990–2013 (left panel), and a long term monthly distribution of cyclonic days over the study area (right panel).

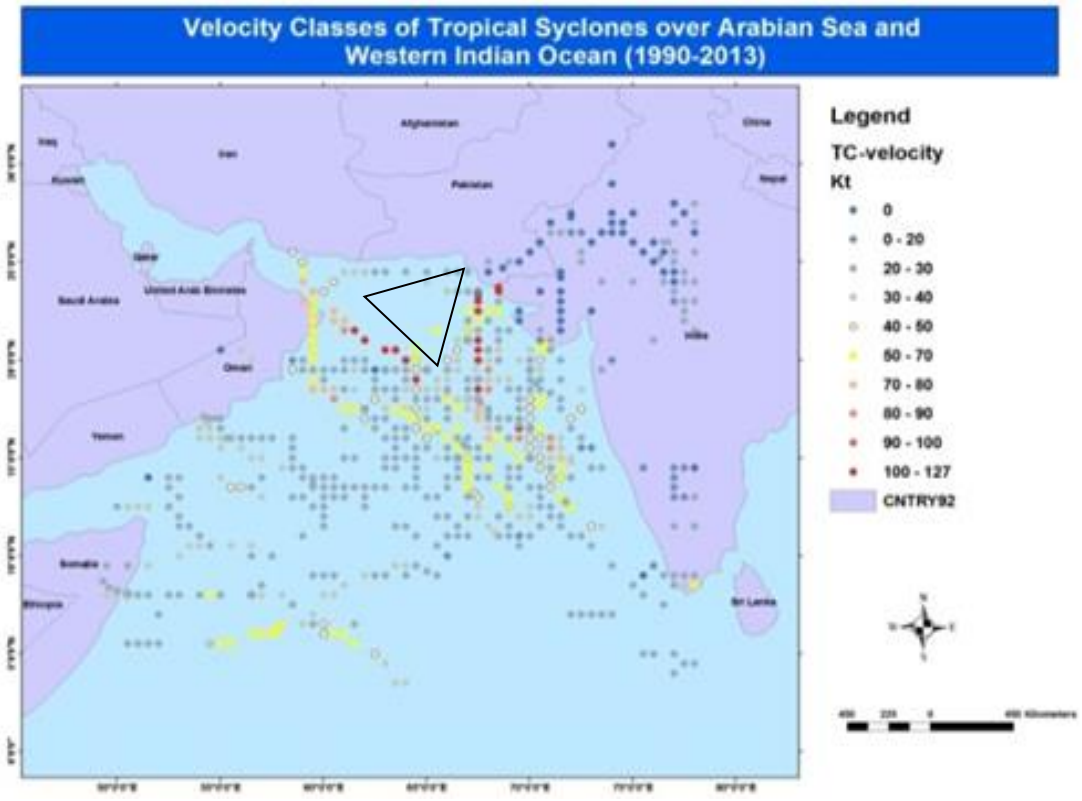

Figure 2. Intensity classifications of the tropical cyclones over the Arabian Sea and Western Indian Ocean through 1990-2013. The area without storm is marked by a triangular on the map.

Table 1. Tropical cyclone frequency, monthly min and max TC events and median for each clusters

Variable / Cluster	Total TC frequency	Monthly min frequency	Monthly max frequency	median
1	265	Jan-Apr (0)	Oct (88)	Oct
2	349	Jan-Apr (0)	May (101)	June
3	113	Jan-Apr&Aug(0)	Nov (61)	Nov
4	145	Feb-Apr&Jul(0)	May (36)	Jul
5	190	Feb-Apr&Jul-Aug (0)	Nov (77)	Oct

Table 2 presents the mean genesis location and the range of those positions along with the variance of TCs based on their x and y for each cluster. The mean values of TC positions show the cluster 4 formed the farthest North and East of all the clusters with the highest variability regarding its ranges of genesis location in both latitude and longitude. The cyclones in cluster 3 are shaped in farthest South and west averagely, along with the highest variability in longitude. The cluster 5 placed in a middle position among these 5 clusters (about 15ºN and 62ºE) with the second highest variability in longitude and latitude after the 4th cluster (Table 2).

The actual output of the K-means clustering is groups of centroid locations and directional variance. Clear separation of the clusters can be seen in the groupings of the centroids and slope and size of the variance ellipses. The clusters1, 2 and 5 sited almost in the central position with the stretched variance ellipses along the longitude, although the second cluster has a more tilted axis. The cluster 4 has the largest rounded ellipse with a positive tilt and the farthest north location. Finally the farthest southern cluster 3 with the variance ellipse elongated along the x axis (Fig.3).

Table 2. Variance and mean values of x and y along with the range of tropical cyclone genesis locations foreach cluster

Variable / Cluster	Variance Lat	Variance Lon	Mean lat	Mean lon	Genesis range lat	Genesis range lon
1	14.66	24.43	16.79	66.94	24.5-3.5	78-51.5
2	14.41	17.85	17.69	67.6	27.5-7	78-54
3	14.58	54.99	11.51	58.35	20.5-5.5	78-49.3
4	57.38	50.17	18.17	69.93	31-4	78-48.5
5	29.89	37.45	15.48	62.62	25.5-5	77.5-50

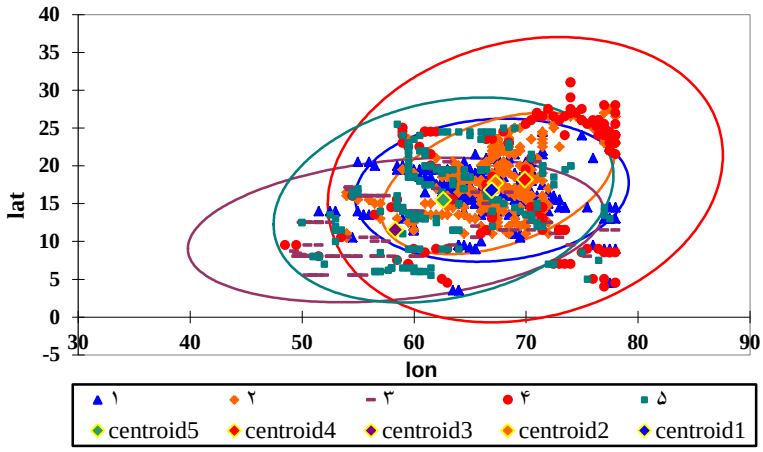

Figure3. Centroid locations (asterisks) for the 5 clusters. Themean centroid value is marked bigger by colored diamond , and the mean variance ellipse with colored lines

2.2 Intensity Variability of the Tropical Cyclones

Intensity analysis of the TCs has been performed using the wind speed data sets for each cluster. All 5 clusters except for the 4th cluster revealed that 50% of the TCs included the intensity more than or equal to55.56km/h, regarding their obtained median values. As the second cluster has the highest storm frequencies, the maximum wind speeds (235.2km/h) as well as the highest standard deviation rank (48km/h) and the highest mean value (72.52km/h) are found in this cluster. Also the skewness test (SKEW) indicated the positive rates which confirm the departure of the TC intensities toward more positive values from the average in the all clusters. The highest SKEW rate (2.95) pertained to the third cluster, as the minimum wind speed (46.3km/h) was the closest to the average value (62.96km/h) in this cluster, while the maximum wind speed is recorded 212.98km/h and so the positive distance from the average value is considered remarkable (Table 3).

2.3 Synoptic Analysis:

In this section we considered the Gonu tropical cyclone which has been happened in 1-7 June 2007 over the study area. To evaluate the physical and dynamical variability of the atmosphere during the Gonu cyclone, the anomalies of sea level pressure, geopotential height, air temperature, relative humidity, vertical velocity and wind vector have been analyzed at different atmospheric levels as follows: The maximum negative anomaly of SLP (sea level pressure) with -4 to -5mb was prevailed over the central Arabian Sea in 3-5 June. The minimum pressure in the eye of cyclone is calculated to be about 898hPa using the images of Metosat satellite. The geopotential height at500hPalevel in 5-6 June showed a -40m anomaly in the east of Oman Gulf and Mokran shores that indicated the northward migration of Subtropical High Pressure (STHP) and on 6 June this anomaly even increased to -60m. The vertical velocity parameter at 500hPa level in 5 June showed the vertical motions anomaly about -0.15hPa/s over the east and southeast of Oman Gulf. In 6-7 June these conditions intensified up to -0.18 and -0.2hPa/s and dominated toward north over the Oman Sea which indicated the severe convective activities. The air temperature at 850hPa atmospheric level illustrated a decrease, as the anomaly values during 4-7 June were about -4 to -8°K over the study region because of a severe condensations in this level and then releasing of latent energy in upper level by temperature increase at 500hPa. By the injection of the moist air from the sea surface to the region in 6 June, the humidity increased by 30% in comparison with the normal period and it extended toward north over the Iranian interior territory. Over the region, the wind velocity increased more than double the normal average. The winds with over 12m/s speed dominated over the southern parts of Oman Sea and the central parts of Arabian Sea in 5 June and gradually moved up towards the north parts of Oman sea and Iranian shores by decreasing the wind speed around 7-8m/s in 8 June, and consequently the huge waves attacked the shoreline and the wave heights in some cases were reported to be more than5-6 meters (Fig.4).

Table 3. Statistical characteristics of the tropical cyclones intensity for 5 clusters over the Arabian Sea during 1980-2013.

Variable / Cluster	Total frequency	Minimum intensity (km/h)	Maximum intensity	Median Intensity	Mean intensity	SKEW	Standard deviation of intensity
1	265	0	194.46	55.56	67.39	1.44	35.68
2	349	0	235.2	55.56	72.52	1.43	48
3	113	46.3	212.98	55.56	64.39	2.95	22.94
4	145	0	188.9	46.3	52.89	0.58	34.8
5	190	0	212.98	55.56	67.87	1.69	34.7

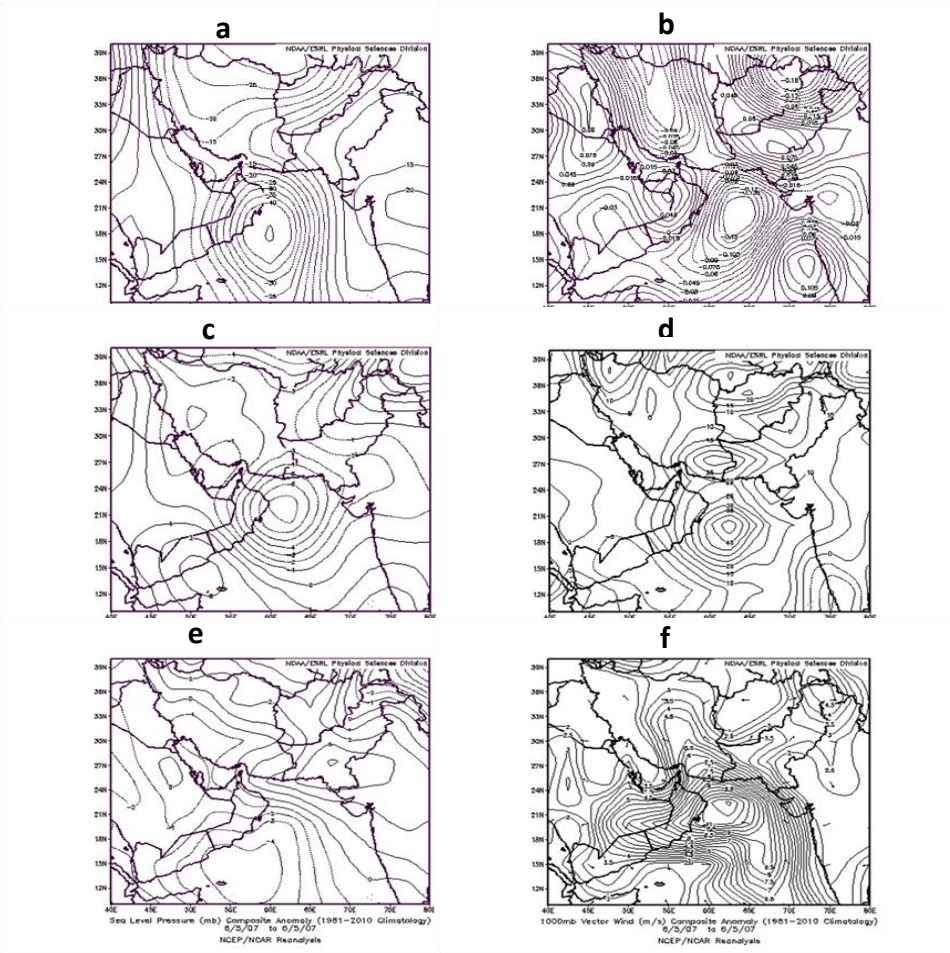

Figure 4. Daily composite anomaly maps (1981-2010), the example for June 5, 2007. a) 500mb geopotential height, b) 500mb vertical wind speed, c) 850mb air temperature, d) 850mb relative humidity, e) sea level pressure, f) 1000mb wind speed.

3. Conclusion

In June 5-7, 2007 satellite images showed some major changes in geomorphology over the southern Iranian coasts, and damages on infrastructures around the shores, e.g., road and electricity networks, jetty structures, and cargo ship sinking.

A long term statistical analysis illustrated that the TC frequency has been raised through a 7-year period of 1998-2004 (max 123 events in 2004) over the study area. In an inter-annual outlook the tropical cyclones were considerably frequentative during per and post monsoon months, as the equatorial position of the Somali Jet and broad region of positive vorticity values that are coupled with warmer regional ocean temperatures provide a larger favorable region for storm development over the Arabian Sea. Spatially the TC records illustrated that the most severe storms (by 148.16-235.2km/h) were found in two tracks with opposite directions, as the both of them originated from the same position as follows, 15º-20º N and 65º-70º E and then the storms moved on in two separate tracks toward northwest and northeast of the Arabian Sea. The K-means cluster method classified the TC records into 5 groups revealing that for the clusters 1, 3 and 5 the main portion of TC frequency has been happened in autumn season, but for the clusters 2 and 4 they have been distributed equally in the first and second half of year. The variance ellipses showed the clusters 1, 2 and 5 were placed over a central position of the study area with the stretched variance ellipses along the longitude axis mostly. The cluster 4 has been considered the largest rounded ellipse and the farthest northern position. While the farthest southern cluster 3 with the variance ellipse elongated along the longitude axis. All 5 clusters except for the cluster 4 confirmed that 50% of the TCs had the intensity more than or equal to 55.56 km/h. The skewness test illustrated a tendency of TC intensities toward more positive values from the average in the all clusters. The results of synoptic analysis by the daily composite maps inJune 1-7, 2007 illustrated that by intensifying the Gonu storm, the axis of subtropical high pressures in the lower levels of atmosphere moved toward the east, and in the mid levels of atmosphere it moved toward the north. This replacement provided the suitable conditions to form an intense convection and tropical cyclone.

4. References

1. Camargo S. J. , A. W. Robertson, S. J. Gaffney, P. Smyth, and M. Ghil, (2007), *Cluster analysis of tropical cyclone tracks. Part I: General properties*.J. Climate,20,3635–3653.

2. Gray, W. M., (1968), *Global view of the origin of tropical disturbances and storms.* Mon. Wea. Rev., 96, 669–697.
3. Evan T. A. and Camargo S. J., (2011), *A Climatology of Arabian Sea Cyclonic Storms.*, Journal of Climate, Volume 4, DOI: 10.1175/2010JCLI3611.1.
4. Henderson-Sellers, A., et al., (1998), *Tropical cyclones and global climate change: A post-IPCC assessment.* Bull. Amer. Meteor. Soc., 79, 19–38.
5. MacQueen, J., (1967), *Some methods for classification and analysis of multivariate observations.* Proc. Fifth Berkeley Symp. On Mathematical Statistics and Probability, Berkeley, CA, University of California, 281–297.
6. Neumann, C. J., B. R. Jarvinen, C. J. McAdie, and J. D. Elms, (1993), *Tropical Cyclones of the North Atlantic Ocean 1871–1992.*, National Climate Data Center–National Hurricane Center, 193 pp.
7. Ramsay. H.A., Suzana J. Camargo and Daehyun Kim (2011), *Cluster analysis of tropical cyclone tracks in the Southern Hemisphere.*,ClimDyn (2012) 39:897–917. DOI 10.1007/s00382-011-1225-8.
8. Riehl. H., (1979),*Climate and weather in the tropics* ,Academic Press, London, No. of pages: 611. ISBN 0.12.588180.0.

INTERNATIONAL JOURNAL OF
COASTAL & OFFSHORE ENGINEERING
IJCOE Vol.4/No. 2/Summer 2019 (47-54)

Available online at: www. Ijcoe.org

Evaluation of Cross-Shore Profile Behavior in Medium-Term Timescales Using XBeach: A Case Study of Zarabad Fishery Harbor, Iran

Ali Shams Derakhshan[1], Mahdi Adjami[2*], Seyed Ahmad Neshaei[3]

[1] *MSc Student, Faculty of Civil Engineering, Shahrood University of Technology, Shahrood, Iran; ali_shdr@yahoo.com*
[2*] *Assistant Professor, Faculty of Civil Engineering, Shahrood University of Technology, Shahrood, Iran; adjami@modares.ac.ir*
[3] *Associate Professor, Department of Civil Engineering, Faculty of Engineering, University of Guilan, Rasht, Iran; maln@guilan.ac.ir*

ARTICLE INFO

Article History:
Received: 20 May. 2019
Accepted: 05 Sep. 2019

Keywords:
XBeach model
Cross-shore profiles
Sand accretion and erosion
Beach sedimentation
Bed level change

ABSTRACT

Among the numerous problems that decrease the capability of a harbor in the country, seasonal sedimentation is identified as a major problem for many fishery harbors. In 2007, Zarabad Fishery Harbor conditions were also identified as critical due to the large volume of sand accumulation and consequent closure of its entrance. Numerical modeling of coastal bed level change was implemented to provide insight into the typical response of the Zarabad beach to regular wave attacks, and to obtain an operational and validated model for the site. Advanced numerical models employed to predict coastal evolution at a variety of time and spatial scales usually include many free parameters that require calibration to the available field data. The XBeach numerical model was selected for its capacity to accurately model hydrodynamic and morphological processes over a two-dimensional domain. It comprises about 250 model settings that approximately 150 of these settings relate to physical and numerical Behavior and the other 100 are case-specific parameters. In this research, 11 parameters are adopted to optimize the model prediction efficiency for Zarabad Fishery Harbor area. For calibration and validation stages, two cross-shore profiles and two medium-term time periods are selected. The model showed great promise in predicting the evolution of cross-shore profiles under water, but as expected, the dry part results showed major errors. XBeach proved to be an operational tool to predict cross-shore profiles in the area, in such timescales. Although, more tests are needed to utilize the model in longer time periods with regard to the duration of simulations.

1. Introduction

As the effect of medium to long term morphological change to coastal sustainability is increasingly recognized, developing methodologies that support predictions over such time scales has become a major concern. Connected to this is the growing prevalence of process-based morphodynamic modeling. These two factors have resulted in a requirement for the application of process-based models to be extended, to allow the assessment of beach change beyond short term time scales [1].

Shore-normal beach profiles are essential for quantifying processes in the coastal zone and for developing the basis for designing coastal structures such as groins, jetties, revetments, and seawalls. The entire range of a standard beach profile captures the active region of coastal processes, starting with the landward bluff or dune and continuing to the point where sediment displacement caused by waves is negligible [2].

Many models which use process-based methods (UNIBEST - TC [3], CROSSMOR2000 [4] and SBEACH [5]) have been available for some time to model cross-shore beach behavior. Van Rijn et al. (2003) present a thorough review of the capacities of these methods to predict cross-shore profile evolution [6]. XBeach is a two-dimensional model for wave propagation, long waves and mean flow, sediment transport and morphological changes of the nearshore area, beaches, dunes, and backbarrier during storms.

XBeach concurrently solves the time-dependent short wave action balance, the roller energy equations, the nonlinear shallow water equations of mass and momentum, sediment transport formulations and bed update on the scale of wave groups [7].

Seasonal sedimentation is known as a major problem for many fishery harbor among the numerous problems that reduce the efficiency of harbor in the country. Out of all fishery harbor, conditions of Zarabad Fishery Harbor were identified as critical in 2007 due to the extensive volume of sand accumulation and consequent closure of its entrance.

The construction of Zarabad Fishery Harbor was completed in 2006 (Figure 1). The Harbor is located at Sistan and Balouchestan Province, Iran (25˚23́N 59˚36́W), which is under constant attacks of south and southwest waves during monsoon season and Shamal winds/waves in winter. As a result of the insufficient reservoir behind the main breakwater to block the high rate of westward Longshore Sediment Transport (LST), a significant volume of sedimentation was observed at the Harbor entrance in a short interval after construction. The large sedimentation forced the authorities to organize a regular monitoring plan of periodic hydrography surveys from 2006 to 2008. A long groin, started at the turning point of the main breakwater, was later constructed to improve the reservoir capacity and to stop the sediment bypassing (Figure 1) [8].

This paper presents the application and validation of XBeach in a specific setting for a medium-term morphological assessing by applying the model to Zarabad Fishery Harbor.

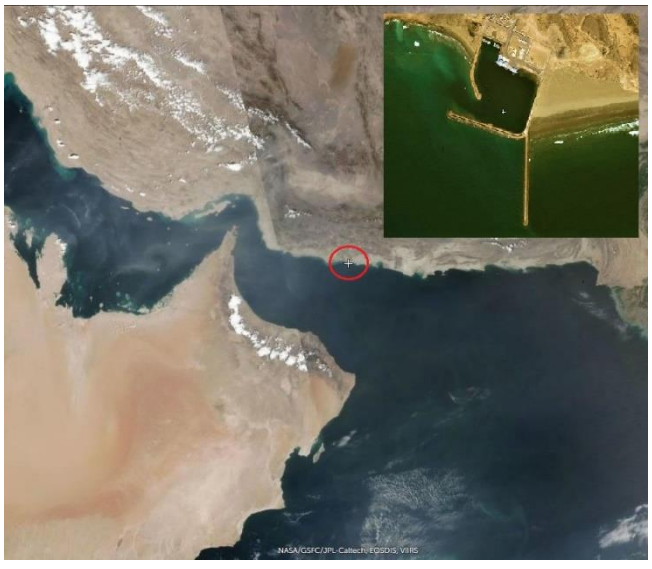

Figure 1. Location of study area and port location

2. Model Description

Originally, XBeach has been developed to model the nearshore responses under storm conditions. It is a 2DH (depth-averaged) model that solves coupled short wave energy, flow and infragravity wave propagation, sediment transport and bed level changes. XBeach simultaneously solves the time-dependent short wave action balance, the roller energy equation, the nonlinear shallow water equation of mass momentum, sediment transport formulation and bed update on the scale of wave groups. The wave action and roller energy are employed to compute the radiation stresses. Depth-averaged shallow water equations are used to compute the mean flow. Sediment transport rates are calculated by using advection-diffusion equations [9]. Further, the equilibrium sediment concentration is calculated with the Soulsby-Van Rijn formulation [10]. Application of XBeach has been given successful results for the dune erosions under storm and hurricane conditions with verifications. By using the existing modeling capabilities of XBeach (e.g. modeling of physical processes and using advanced options such as "hard structure"), nearshore coastal processes around a Harbor structure are reproduced to explain the sand accretion and erosion patterns of beach nearshore profile in this study.

2.1. Main Equations

A summary of most important equations which has been used in XBeach model is described in the following sections:

2.1.1. Wave Action Equation

In XBeach, the wave force is defined by a time-dependent version of the wave action balance equation in the shallow water momentum equation. The balance of the wave action is shown as follows (Eq. (1)) [11]:

$$\frac{\partial A}{\partial t}+\frac{\partial c_{gx}A}{\partial x}+\frac{\partial c_{gy}A}{\partial y}+\frac{\partial c_{\theta}A}{\partial \theta} = -\frac{D_w+D_f+D_v}{\sigma} \quad (1)$$

Where, wave action is defined as:

$$A(x,y,t,\theta)=\frac{S_w(x,y,t,\theta)}{\sigma(x,y,t)} \quad (2)$$

Where θ represents the angle of incidence with respect to the x-axis, S_w represents the wave energy density in each directional bin and σ the intrinsic wave frequency. The intrinsic frequency σ and group velocity c_g is obtained from the linear dispersion relation. D_w, D_f and D_v are dissipation terms for waves, bottom friction, and vegetation, respectively. The intrinsic frequency is for instance obtained with [11]:

$$\sigma=\sqrt{gk\tanh kh} \quad (3)$$

The wave action propagation speeds in x, y, and directional space are given by:

$$c_{gx}(x,y,t,\theta) = c_g \cos(\theta)$$
$$c_{gy}(x,y,t,\theta) = c_g \sin(\theta)$$
$$c_\theta(x,y,t,\theta) = \frac{\sigma}{\sinh 2kh}\left(\frac{\partial h}{\partial x}\sin\theta - \frac{\partial h}{\partial y}\cos\theta\right) \quad (4)$$

Where h represents the local water depth and k the wave number. The intrinsic frequency of the wave σ is determined without the interaction of the wave current (keyword: wci=1), meaning that it is equal to the absolute radial frequency, ω [11].

2.1.2. Roller Energy Equation

In the XBeach model, roller energy is coupled with the wave action equation, where wave energy dissipation is taken as a source term for the equation of roller energy balance. The roller energy balance is shown as follows (Eq. (5)):

$$\frac{\partial E_r}{\partial t} + \frac{\partial E_r c\cos\theta}{\partial x} + \frac{\partial E_r c\sin\theta}{\partial y} = D_w - D_r \quad (5)$$

Where E_r is representing roller energy in each directional bin. The speed of propagation of roller energy is given by c. The total dissipation of wave energy and the dissipation of roller energy are represented by D_w and D_r respectively [11].

2.1.3. Shallow water equations

Shallow water equations are employed to calculate mean flow in XBeach. The depth-averaged Generalized Lagrangian Mean (GLM) formulation is used to include the wave-induced mass-flux and the return flow. In that context, the momentum and continuity equations are formulated in terms of the Lagrangian velocity (u^L), which is defined as the distance, a water particle travels in one wave period, divided by that period. The resulting GLM momentum equations are presented by the following equations [12]:

$$\frac{\partial u^L}{\partial t} + u^L\frac{\partial u^L}{\partial x} + v^L\frac{\partial u^L}{\partial y} - f\,v^L - \nu_h\left(\frac{\partial^2 u^L}{\partial x^2} + \frac{\partial^2 u^L}{\partial y^2}\right) =$$
$$\frac{\tau_{sx}}{\rho h} - \frac{\tau^E_{bx}}{\rho h} - g\frac{\partial \eta}{\partial x} + \frac{F_x}{\rho h} - \frac{F_{v,x}}{\rho h}$$
$$\frac{\partial v^L}{\partial t} + u^L\frac{\partial v^L}{\partial x} + v^L\frac{\partial v^L}{\partial y} + f\,u^L - \nu_h\left(\frac{\partial^2 v^L}{\partial x^2} + \frac{\partial^2 v^L}{\partial y^2}\right) = \quad (6)$$
$$\frac{\tau_{sy}}{\rho h} - \frac{\tau^E_{by}}{\rho h} - g\frac{\partial \eta}{\partial y} + \frac{F_y}{\rho h} - \frac{F_{v,y}}{\rho h}$$
$$\frac{\partial \eta}{\partial t} + \frac{\partial h u^L}{\partial x} + \frac{\partial h v^L}{\partial y} = 0$$

where τ_{sx} and τ_{sy} are the wind shear stresses, τ_{bx} and τ_{by} are the bed shear stresses, η is the water level, F_x and F_y are the wave-induced stresses, $F_{v,x}$, and $F_{v,y}$ are the stresses induced by vegetation, ν_h is the horizontal viscosity and f is the Coriolis coefficient [11].

2.2. Boundary conditions

2.2.1. Wave Boundary Conditions

Based on the given values of Hrms (root mean square wave height), Tm01 (spectral period), wave direction and directional distribution power, we used stationary wave boundary conditions (instat=0), as it is suggested to be used in mild conditions. The surf beat effects, resulted from extreme storm conditions are assumed to be negligible in this study. Since infragravity motions (where 30 < wave period < 300 sec) do not play an influential role, the "instat=0" option was implemented to solve the stationary problem directly using forward marching technique. Wave data were extracted at a depth of 20 m near the harbor area where XBeach grid y-axis is located. Boundaries, which are perpendicular to the coastline, are known as lateral boundaries. For the stationary wave mode Neumann boundaries are the only option. It allows a correct representation of the wave propagation near the lateral boundaries, without the usual shadow zones in e.g. SWAN. By neglecting the longshore gradients, the model automatically computes a consistent 1D solution [11]. However, in order to minimize the undesirable effects of lateral boundaries, these boundaries have been set far enough from the area of interest (i.e. fishery Harbor). In this sense, their influence is assumed to be insignificant for the study area.

2.2.2. Flow Boundary Conditions

An offshore or lateral boundary is typically an artificial boundary which has no physical significance. On the offshore boundary wave and flow conditions are imposed. In the domain, waves and currents will be generated which need to pass through the offshore boundary to the deep sea with minimal reflection. One way to do this is to impose a weakly reflective-type boundary condition (absorbing-generating)(keyword: front). With option front = abs2d (default value) the formulation by Van Dongeren and Svendsen (1997) is activated which allows for obliquely-incident and obliquely-reflected waves to pass through the boundary [11]. Lateral boundaries are placed away from the area of interest to minimize the influence of boundaries on the results. For this purpose, Neumann boundaries (no - gradient) were activated as lateral boundaries, by setting options "left = neumann" and "right = neumann"

2.3. Model input and output data

The surveys taken after 2006 are used as bathymetry input and wave condition series provided by Wave Watch III is used as wave condition input in this study. Furthermore, the nearest accessible tide station (Chabahar station) is used as a single tide location (tideloc = 1) input.

The output is bed level change which is presented as two cross-shore profiles selected to evaluate the model (Figure 2).

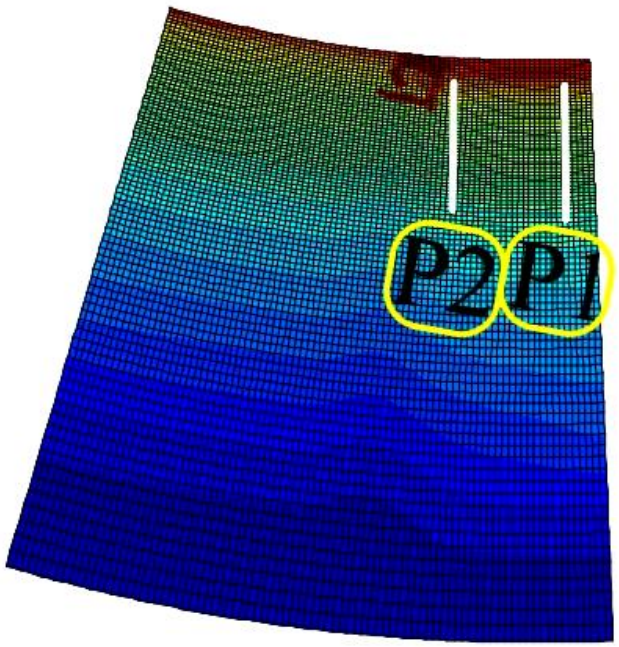

Figure 2. Model grid and cross-shore profiles selected for evaluation in this study

2.2. Model Calibration and Validation

Two time periods (2006.02.20 to 2006.09.23 and 2007.02.20 to 2006.10.23) are selected for calibrating and validating the model, respectively. Furthermore, two cross-shore profiles (p1 and p2) are selected for this purpose. Evaluating the results is done by employing the Brier Skill Score (BSS) and also visual observation.

BSS represents how well the model predicts the bathymetry compared with the initial bathymetry. The following classification was given for the BSS by Van Rijn et al. (2003) [13]:

Table 1. Classification of Brier Skill Score by Van Rijn et al. (2003).

Score	Classification
<0	Bad
0-0.3	Poor
0.3-0.6	Reasonable
06-0.8	Good
0.8-1.0	Excellent

Nine specific XBeach parameters (i.e. fw, cf, gammax, beta, wetslp, alpha, facSk, facAs, and gamma) have a major influence on the model results. These parameters are also optimized for the Dutch coast for 1D storm models and are referred to as WTI settings [14]. With regard to the literature review, these parameters plus hmin and dryslp are employed to optimize the model in this study.

3. Results

Numerous simulations have been performed to optimize all parameters for Zarabad Fishery Harbor. All simulation settings are selected as extended as defined in the model manual to cover the whole range possible. After optimizing each parameter individually, a simulation including all optimizations has performed to reach the final calibration. Table 2 presents a summary of parameter optimization including BSS for each case. BSS is divided by shoreline into 2 parts (i.e. wetBSS and dryBSS) to avoid the XBeach typical lack of accuracy in predicting dune evolution.

According to Table 2, default values are selected for 3 parameters (i.e. fw, dryslp and facAs), beta and optimization showed the best BSS in wet and dry part, respectively.

Table 2. Parameters selected for model optimization and resulted Brier Skill Scores

Parameter	Definition	Range	Default	Selected	P2		P1	
					WetBSS	DryBSS	WetBSS	DryBSS
fw	Short wave friction coefficient	0.0~1.0	0.00	0.00	0.487	-0.064	0.851	-0.203
cf	Dimensionless friction coefficient flow	3.5e-05~0.9	0.003	0.0025	0.502	-0.073	0.854	-0.072
gammax	Maximum wave height to water depth	0.4~5.0	2.000	2.2	0.496	-0.032	0.851	-0.053
beta	Breaker slope coefficient	0.05~0.3	0.100	0.06	0.515	-0.919	0.862	-0.145
wetslp	Critical avalanching slope under water	0.1~1.0	0.300	0.26	0.487	-0.065	0.851	-0.199
dryslp	Critical avalanching slope above water	0.1~2.0	1.0	1.0	0.487	-0.064	0.851	-0.203
alpha	Wave dissipation coefficient	0.5~2.0	1.000	1.25	0.500	-0.062	0.850	-0.0826
facSk	Skewness factor	0.0~1.0	0.100	0.35	0.488	-0.071	0.853	-0.194
facAs	Asymmetry factor	0.0~1.0	0.100	0.1	0.487	-0.064	0.851	-0.203
gamma	Breaker parameter for Baldock	0.4~0.9	0.550	0.8	0.491	-0.081	0.852	-0.197
hmin	Threshold water depth above which Stokes drift is included	0.001~1.0	0.2	0.5	0.488	-0.057	0.856	-0.062

Overall calibration result (first period) is shown as cross-shore profiles in Figure 3. Setting resulted from calibration is used in the validation step (second period) to ensure model proficiency. The results show "Good" and "Excellent" accuracy for the wet part of the Profile 1 since the model's BSS is close to 1, according to Van Rijn et al. 2003 (Table 1). Nevertheless, for Profile 2, since dominated longshore flow is westward in this study, the results are simply "Reasonable" due to neglecting longshore sediment transport in storm condition by XBeach.

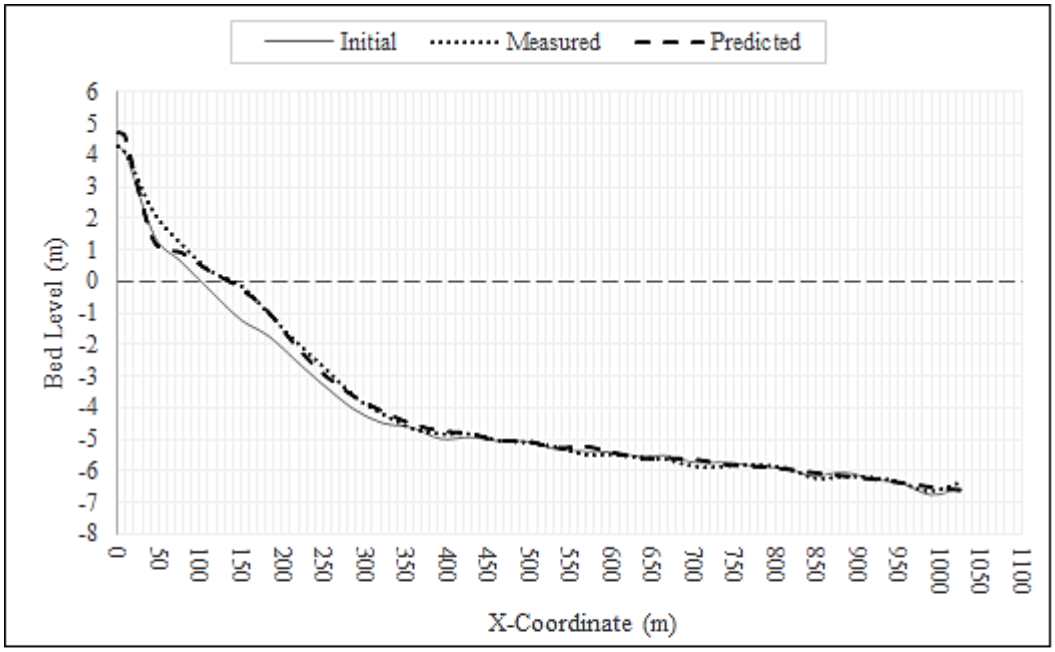

(a)

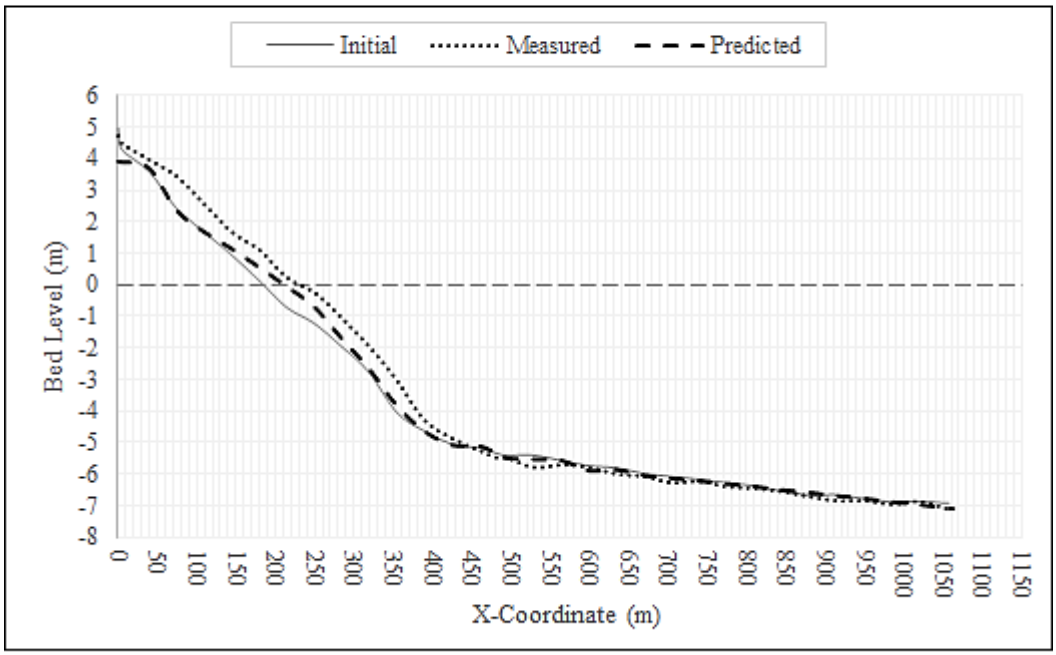

(b)

Figure 3. Profile 1 (a) and Profile 2 (b) bed level change in calibration step (2006.02.20 to 2006.09.23)

Figure 4 shows how well the calibrated model performs in a simulation of about 8 months (254 days) compared to the corresponding bathymetric surveys conducted at the beginning and end of the modeling timespan (validation step).

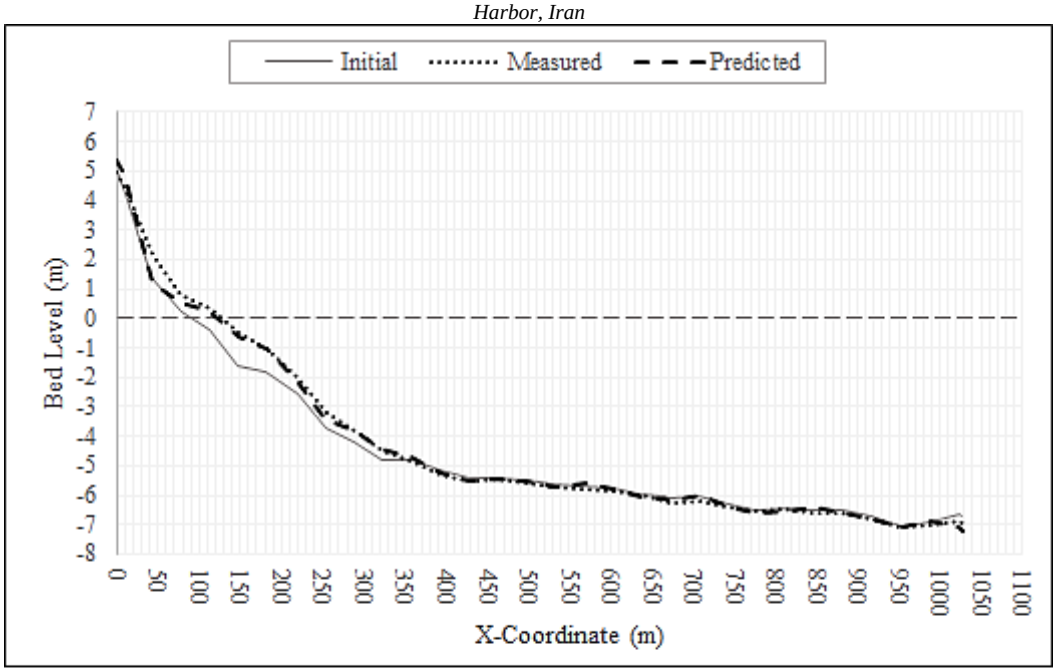

(a)

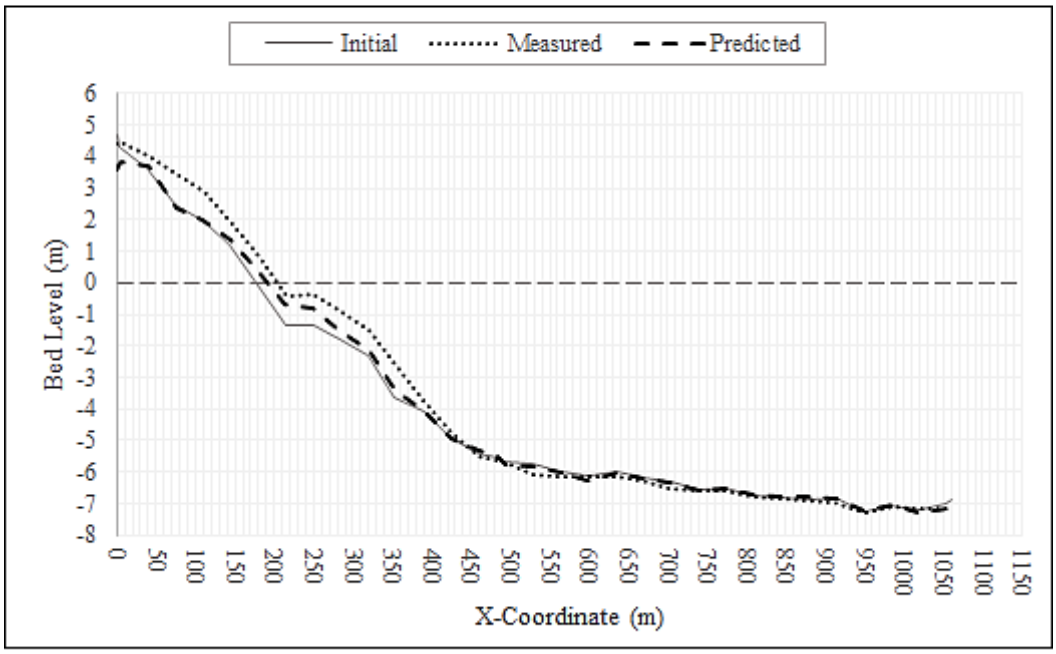

(b)

Figure 4. Profile 1 (a) and Profile 2 (b) bed level change in validation step (2007.02.20 to 2007.10.23)

Validation step showed similar results to calibration step as it was expected. Final results of both steps are summarized in Table 3.

Table 3. Overall result of Validation and Calibration steps

		Calibration	Validation
P1	**WetBSS**	0.877	0.863
	DryBSS	-0.063	-0.019
P2	**WetBSS**	0.533	0.461
	DryBSS	-0.052	-0.037

5. Conclusions

The XBeach model was tested for two periods in order to calibrate and validate the model for Zarabad fishery Harbor area. Eleven Parameters were selected with regard to the literature reviews to calibrate the model, accurately.

In the calibration and the validation phase, the threshold depth of sediment movement (depth of closure) was recognized to be about -7m. Though, both phases showed significantly excessive dry shoreface erosion.

Under water, both phases showed less sediment accumulation than is recognized in the surveys. In both steps, Profile 2, which is close to the main breakwater and in downstream of main longshore flow, shows less accuracy; However, it can be because of shortage of selected area in longshore direction that

influence the extent of longshore sediment transport. Also, the model showed significant uncertainty in downstream of longshore sediment flow.

Generally, the model showed great promise in predicting the overall shape of cross-shore profiles under water; however, it showed significant errors in dry part of cross section. According to the results presented in this study, XBeach can be used for predicting the morphological changes in Zarabad Fishery Harbor area with "Reasonable" to "Good" Brier Skill Score. Furthermore, It is necessary to test the model in long-term periods to be more operational.

8. References

1- Pender, D., & Karunarathna, H. (2013). *A statistical-process based approach for modelling beach profile variability*. Coastal Engineering, 81, 19-29.

2- Albert, K. M. (2017). *Modeling Morphological Change on Western Kenai Peninsula Beaches* (Doctoral dissertation, University of Alaska Anchorage).

3- Reniers, A. J. H. M., Roelvink, J. A., & Walstra, D. J. R. (1995). *Validation study of UNIBEST-TC model*. Report H2130, Delft Hydraulics, Delft, The Netherlands.

4- Van Rijn, L. C., & Wijnberg, K. M. (1996). *One-dimensional modelling of individual waves and wave-induced longshore currents in the surf zone*. Coastal Engineering, 28(1-4), 121-145.

5- Larson, M., & Kraus, N. C. (1989). *SBEACH: numerical model for simulating storm-induced beach change. Report 1. Empirical foundation and model development* (No. CERC-TR-89-9). Coastal Engineering research center Vicksburg Ms.

6- Van Rijn, L. C., Walstra, D. J. R., Grasmeijer, B., Sutherland, J., Pan, S., & Sierra, J. P. (2003). *The predictability of cross-shore bed evolution of sandy beaches at the time scale of storms and seasons using process-based profile models*. Coastal Engineering, 47(3), 295-327.

7- Roelvink, D., Reniers, A., Van Dongeren, A. P., de Vries, J. V. T., McCall, R., & Lescinski, J. (2009). *Modelling storm impacts on beaches, dunes and barrier islands*. Coastal engineering, 56(11-12), 1133-1152.

8- Tabasi, M., Soltanpour, M., & Ravindra, M. P. *Study And Modeling Of Cross-Shore Sediment Transport At Zarabad Fishery Port*.

9- Galapatti, R, and Vreugdenhil, CB (1985). *A depth integrated model for suspended transport, Report 83-7, Communications on Hydraulics*, Department of Civil Engineering, Delft University of Technology.

10- Soulsby, R. (1997). *Dynamics of marine sands: a manual for practical applications*. Thomas Telford.

11- Roelvink, D., Van Dongeren, A., McCall, R., Hoonhout, B., van Rooijen, A., van Geer, P. ... & Quataert, E. (2015). *XBeach Technical Reference: Kingsday Release. Model Description and Reference Guide to Functionalities*. Delft-The Netherlands.

12- Andrews, D., & McIntyre, M. E. (1978). *An exact theory of nonlinear waves on a Lagrangian-mean flow*. Journal of fluid Mechanics, 89(4), 609-646.

13- Van Rijn, L. C., Walstra, D. J. R., Grasmeijer, B., Sutherland, J., Pan, S., & Sierra, J. P. (2003). *The predictability of cross-shore bed evolution of sandy beaches at the time scale of storms and seasons using process-based profile models*. Coastal Engineering, 47(3), 295-327.

14- Van Geer, P., den Bieman, J., Hoonhout, B., & Boers, M. (2015). *XBeach 1D–Probabilistic model: ADIS, Settings, Model uncertainty and Graphical User Interface*. Tec. Rep 1209436-002-HYE, 1.

INTERNATIONAL JOURNAL OF
COASTAL & OFFSHORE ENGINEERING
IJCOE Vol.4/No. 2/Summer 2019 (55-63)

Available online at: www. Ijcoe.org

Capacity Evaluation of Ressalat Jacket of Persian Gulf Considering Proper Finite Element Modeling of Tubular Members

Mohammad Hadi Erfani [1] , Mohammad Reza Tabeshpour [2*], Hasan Sayyaadi [3]

[1] Ph.D. Student, Department of Mechanical Engineering, Sharif University of Technology; Erfani_mh@mech.sharif.edu*
[2] Associate Professor, Department of Mechanical Engineering, Sharif University of Technology; Tabeshpour@sharif.edu
[3] Professor, Department of Mechanical Engineering, Sharif University of Technology; Sayyaadi@sharif.edu

ARTICLE INFO

Article History:
Received: 11 May. 2019
Accepted: 10 Sep. 2019

Keywords:
Local Buckling
Pushover Analysis
Jacket Type Offshore Platforms
Compressive Behavior
ISO Equation

ABSTRACT

The capacity curve obtained from the pushover analysis of jacket-type offshore platforms gives their structural performance levels, ultimate capacity and ductility. Accurate estimation of structural capacity curve is of great importance. Accurate modeling of the global and local buckling of compression tubular members in a correct form is an effective part of studying the behavior of offshore jackets under all various types of loading conditions at any given time of their life. Modeling of compressive braces by shell or solid elements when the imperfections are applied leads to deformations due to local buckling based on buckling modes. This paper aims to achieve more accurate compressive behavior of compression members. The ABAQUS finite element software has been used for this purpose. Regarding to the results achieved from investigation of buckling in tubular members proper elements have been introduced to investigate the global and local buckling phenomena. Then pushovers results of Ressalat jacket with conventional modeling versus more accurate modeling proposed in this paper for compressive members have been compared as a case study. According to the results applying improper mesh size for compressive members can under-predict the ductility by 33% and under-estimate the lateral loading capacity up to 8%. Finally, ISO equations and Marshall strut theory have been applied to investigate critical buckling load and post-buckling response of tubular braces. The innovation of this paper is investigating the interaction of global and local buckling in the braces of jacket with 1-Dimentional elements using ISO equations and buckling envelope derived from the solid element results, which results in low computational costs.

1. Introduction

Critical buckling loads can be calculated for tubular members using empirical equations. These equations are presented by design codes such as API RP-2A WSD and API RP 2A-LRFD (recommended practice for planning, designing, and constructing fixed offshore platforms), ISO 19902 and NORSOK N-004 to achieve load and resistance design factors. All of these codes have been checked in order to assure that design loads do not meet critical buckling loads in normal and extreme operational conditions. Also both global elastic buckling and inelastic buckling are covered by design codes where prevent local buckling in walls of tubular members by decreasing the loads. Even to ensure that applied loads do not exceed the critical buckling loads in normal operations, these codes explain structural configuration of members.

Some members compress higher than their buckling limit under extreme load conditions such as ductility level earthquake (DLE[1]) and the results of this case on the behavior of the structure also need to be examined. It is possible that the structures are designed in such a way that local buckling occurs in some members under extreme loads. Subsequently, in the process of analysis, it is checked that the level of structural failure remains within acceptable limits. In this analysis, the actual response of the structure is obtained. For this purpose load factors and capacity factors are equal to 1. It is important that local buckling of members and their post-buckling behavior are detected, correctly. So that

[1] Ductility Level Earthquake

the load transfer to adjacent elements is not underestimated. Nonlinear finite element models with 1-D beam elements are usually used to analysis the collapse of jacket structures. But the beam elements do not consider the local buckling response and local deformation of walls of members. Local buckling often occurs in members with low ratio of diameter to thickness ratio (D/t). As the diameter to thickness ratio increases, local buckling is postponed to global buckling, and this event leads to a further drop in post-buckling capacity in comparison with the value that predicted by using the beam element. Also, models with beam elements cannot directly consider radial and circumferential imperfections due to fabrication tolerances which reduce load carrying capacity.

When shell elements are used to model thin-walled tubular members, the model elements is capable of considering global and local buckling at shell walls simultaneously.

The following is an overview of the researches that has been conducted to investigate the buckling of the tubular members. Karamanos and Tassoulas [1] derived curves concerning the capacity of tubular members using a nonlinear FE technique under the combination of external pressure and bending. Sadowski and Rotter [2] investigated the structural behavior of tubular columns under buckling phenomenon considering shell elements. Bardi and Kyriakides [3,4] studied the plastic buckling range of thick cylindrical shells. They focused on circular stainless steel tubes in both experimental and analytical phases. Yasseri and Skinner [5] in 2006 studied the global and local buckling of and their interaction for tubular members under concentrated force and moment. They classified the compressive members based on the diameter to thickness ratio (D/t) and the ratio of length to gyration radius (L/r). They proposed the suggested API curve of elastic and non-elastic buckling based on the slenderness. They also studied the effects of the imperfection of compressive members. The modified properties of steel material which can be used for beam elements to achieve the same response of shell elements have been also presented in that report. Wenjing and Hoogenboom [6] in 2011 checked the buckling of the frame members when the buckling length has been set manually. Based on their estimation, 5 to 10% of the man-hours in structural analysis of removal projects has been spent on checking and correcting buckling lengths. Using another method is available that does not require determining buckling lengths. In the study, the NORSOK standard for tubular steel frame structures has been used to derive this method. They concluded that this method can be successfully applied. In this paper, for a 2-D frame of a typical jacket platform, the global and local buckling of models developed by using shell or beam elements are compared. Also, the responses of beam elements that can consider the effects of local buckling are obtained. For this purpose, the Marshall strut theory in the ABAQUS finite element software suite is used.

2. Analytical models

Two types of second-order shell and beam elements have been used to develop the models. Frame elements have been used to reflect the effect of local buckling that it can be formed well in the walls of tubular parts ,modeled by shell elements, because of local deformations. The most important difference of beam elements compared to frame elements, is that frame elements use ISO 19902 buckling equations in addition to the beam elements equations. Also, in terms of numerical modeling, the number of frame elements is limited to one mesh element in length. After the buckling happens, the response of standard frame element is switched to the buckling strut response and is never switched back again. If the buckling strut response is requested for the element from the first step of the analysis, the member will be changed to a simply-supported member, so that the member cannot resists against bending moments. The proper meshing of elements in a model provides optimum precision. When a fine-meshed shell model is used, local buckling occurs earlier than beam models and also does not reach the same post-buckling strength in the load-displacement graph. But frame elements correct this deficiency of beam elements and also reduce the computational costs.

A primary imperfection equal to 0.1% of member length has been applied to the compressive members of shell and beam elements to consider the buckling phenomena. It is necessary first to obtain probable buckling modes by calculating the eigenvalues of the model, in order to determine the locations of imperfe-ctions. The models with frame elements do not require applying the imperfection; these types of elements consider both elastic and inelastic buckling.

The mesh size is almost the same at both models of shell elements and beam-frame elements, So that the results are better comparable. Of course, it should be noted that frame elements only have a single mesh along its length.

3. Analysis method

The static Riks analysis method has been used in ABAQUS software because the other analysis methods become unstable under a sudden reduction in stiffness due to buckling. In the Riks procedure, deformations and loads are considered simultaneous-ly. This means that the magnitude of the load is taken as a variable and the arc length method, in a static equilibrium in the load-displacement space, is used to obtain the solution [7]. So, the ABAQUS program is able to discover the post-buckling response of the model by reducing the applied load and solving the load-displacement equation.

The models of beam and shell elements with and without imperfection are analyzed by this method. And the buckling and post-buckling responses of both element types are compared.

4. Loading

The purpose of this paper is to estimate the pushover curve of the structure by enforcing lateral displacement and extracting the base shear. This lateral displacement can be imposed on solitary node placed on highest deck of jacket or distributed to all nodes at different levels of the platform along the height. In each case the reaction forces at the level of the fixed supports at the bottom of piles, which is the base shear and equal to the total load applied to the platform, have been calculated. Therefore, the approach of displacement-control has been adopted in this paper. So, ductile behavior of structure can be observed correctly in load-displacement curve obtained from pushover analysis. Fig. 1 illustrates two distributions of lateral displacement applied in this paper.

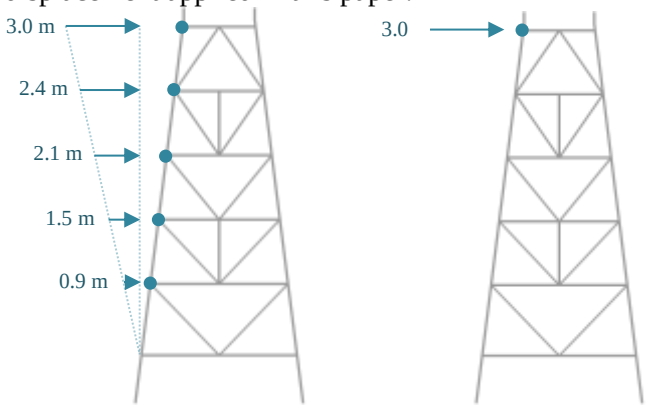

Figure 1. Two types of distribution of lateral displacement applied in FE models

5. Material properties

Almost all the elements have been defined by yield stress of 355 MPa and ultimate strength of 535 MPa at a plastic strain of 0.144. The narrowing test of the coupon bar under axial load is used to obtain true stresses. The values of true stresses and logarithmic strains are calculated from the nominal experimental values using the following equations.

$$\sigma_{true} = \sigma_{nom}(1 + \varepsilon_{nom}) \quad (1)$$

$$\varepsilon_{ln}{}^{pl} = \ln(1 + \varepsilon_{nom}) - \sigma_{nom}/E \quad (2)$$

6. Buckling prediction, analytical equations

This part describes the ISO equation in detail, but the differences of the approach of other standards have been explained [8]. All four codes (API RP-2A WSD, API RP 2A-LRFD, ISO 19902 and NORSOK N-004) provide sets of formulations for each load type acting alone or in combination. The ISO equation is used with a high accuracy to predict the onset of buckling in slender members with pipe-like cross-sections. All quantities with dimensions have dimensions of stress.

$$\frac{\gamma_{R.c}\sigma_c}{f_c} + \frac{\gamma_{R.b}}{f_b}\left[\left(\frac{C_{m.y}\sigma_{b.y}}{1-\sigma_c/f_{e.y}}\right)^2 + \left(\frac{C_{m.z}\sigma_{b.z}}{1-\sigma_c/f_{e.z}}\right)^2\right]^{0.5} \leq 1.0$$

and (3)

$$\frac{\gamma_{R.c}\sigma_c}{f_{yc}} + \frac{\gamma_{R.b}\sqrt{\sigma_{b.y}^2 + \sigma_{b.z}^2}}{f_b} \leq 1.0$$

Here, f_c is the characteristic axial compressive stress, f_b is the characteristic bending stress, c_{m1} and c_{m2} are reduction factors corresponding to the cross-section directions 1 and 2, and F_{e1} and F_{e2} are the Euler buckling stresses corresponding to the 1 and 2 directions.

$$I_{11} = I_{22} = \frac{\pi}{64}(D^4 - (D - 2\,t)^4) \quad (4)$$

$$Z_e = \frac{\pi}{64}(D^4 - (D - 2\,t)^4)/\left(\frac{D}{2}\right) \quad (5)$$

$$Z_p = (D^3 - (D - 2\,t)^3)/6 \quad (6)$$

$$r = \sqrt{I_{22}/A} = \frac{1}{4}\sqrt{(D^2 - (D - 2\,t)^2)} \quad (7)$$

Local buckling check in ISO and NORSOK is based on material as well as geometric properties of members whereas in API WSD and API LRFD it depends on only geometry parameters. Therefore, the terms of the ISO equation are calculated as follows:

$$f_c = P/A \quad (8)$$

$$f_{bi} = M_i/Z_e \quad (9)$$

$$F_{yc} = f_y \quad \text{for} \quad \frac{f_y}{F_e} \leq 0.17$$

$$F_{yc} = \left(c_2 - c_3\frac{f_y}{F_e}\right)f_y \quad \text{for} \quad \frac{f_y}{F_e} \leq 1.911 \quad (10)$$

$$F_{yc} = F_e \quad \text{for} \quad \frac{f_y}{F_e} > 1.911$$

$$c_2 = 1.04654873 \quad \& \quad c_3 = 0.27381606 \quad (11)$$

$$F_e = 2CE\left(\frac{t}{D}\right) \quad \& \quad C = 0.3 \quad (12)$$

Where, F_{yc} is the local buckling strength and for $\frac{f_y}{F_e} > 1.911$ the F_{yc} is equal to the elastic local buckling strength (F_e). There is only a slight difference in limitation between ISO and the NORSOK code but both of them have the same approach. API WSD and LRFD codes distinguish between elastic and inelastic buckling stresses. The inelastic local buckling stress formula proposed by API WSD and LRFD codes is as follows:

$$F_{yc} = f_y \quad \text{for} \quad \frac{D}{t} \leq 60$$

$$F_{yc} = \left(1.64 - 0.23\left(D/t\right)^{1/4}\right)f_y \leq F_e \quad (13)$$

$$\text{for} \quad 60 < \frac{D}{t} < 300;\ t \geq 6\,mm$$

In the above local buckling equations, ISO and NORSOK codes limit D/t to a maximum of only 120, whereas the API increase the upper limit of D/t ratio to 300 meaning that NORSOK is significantly more conservative.

$$F_c = [1 - 0.278\lambda^2]F_{yc} \quad \text{for} \quad \lambda \leq 1.34 \quad (14)$$

$$F_c = \frac{c_1}{\lambda^2}F_{yc} \quad \text{for} \quad \lambda > 1.34$$

$$\lambda = \max(\lambda_1, \lambda_2) \quad \& \quad c_1 = 0.89282978 \quad (15)$$

$$\lambda_i = \frac{k_i L_i}{\pi r}\sqrt{\frac{F_{yc}}{E}} \quad (16)$$

Where, F_c is the representative axial compressive strength, in stress units; λ is the column slenderness parameter. The two API LRFD and NORSOK codes recommend formulae similar to ISO form but employ different coefficients. The overall column buckling formula in API WSD uses the AISC formulation, while API LRFD, ISO and NORSOK are limit state design (LSD) or LRFD based. The NORSOK recommended equation gives lower capacity than API LRFD and ISO. Unlike the other three standards, NORSOK code assumes that the platform is manned even during extreme environmental events, so in calculation of both local and overall buckling strength, NORSOK is more conservative. The API WSD formula in accordance with AISC is as follows:

$$F_c = \frac{\left[\left(1-\left(Kl/r\right)^2\right)/\left(2C_c^2\right)\right]}{5/3+3\left(Kl/r\right)/(8C_c)-\left(Kl/r\right)^3/(8C_c^3)} f_y \quad \text{for } \frac{Kl}{r} < C_c \quad (17)$$

$$F_c = 12\pi^2 E/\left[23\left(Kl/r\right)^2\right] \quad \text{for } Kl/r > C_c$$

$$C_c = \left(2\pi^2 E/f_y\right)^{1/2} \quad (18)$$

$$F_b = \left(Z_p/Z_e\right)f_y \quad \text{for } \frac{f_y D}{Et} \le 0.0517$$

$$F_b = \left(c_4 - 2.58\left(\frac{f_y D}{Et}\right)\right)\left(Z_p/Z_e\right)f_y \quad \text{for } 0.0517 < \frac{f_y D}{Et} \le 0.1034 \quad (19)$$

$$F_b = \left(c_5 - 0.76\left(\frac{f_y D}{Et}\right)\right)\left(Z_p/Z_e\right)f_y \quad \text{for } 0.1034 < \frac{f_y D}{Et} \le 120\frac{f_y}{E}$$

$$c_4 = 1.133386 \quad \& \quad c_5 = 0.945198 \quad (20)$$

Where, F_b is the bending strength. The formulae from all four codes are the same but the API WSD has different coefficients. According to above equations, elastic section modulus, plastic section modulus and yield strength can be seen in formulae because LSD and LRFD approaches consider full plasticity and yielding in the section, whereas because of WSD methodology which limits the stress to a fraction of the yield, only the yield strength exist in API WSD equations.

Also in evaluation of bending capacity NORSOK is more conservative than three others.

$$F_{ei} = \frac{F_{yc}}{\lambda_i^2} \quad (21)$$

Where, C_{m1} and C_{m2} are reduction factors corresponding to the cross-section directions 1 and 2. These factors are functions of the end moments, compressive stress and Euler buckling stresses with the default values of 0.85. By satisfying the following condition:

$$I(f_c, f_{b1}, f_{b2}) = 1.0 \quad (22)$$

Standard frame element response is switched to the buckling strut response and is never switched back again. The ISO equation yields the critical load, P_{cr}, which is defined as $f_c A$. When the axial forces are negligible and the bending moments have large values, another inequality is also used. This additional control is called the strength equation and is as follows:

$$S = \frac{f_c}{F_{yc}} + \frac{1}{F_b}\sqrt{f_{b1}^2 + f_{b2}^2} \quad (23)$$

The API WSD, ISO and NORSOK codes formulae have the same linear form with some partial differences, while API LRFD recommends a cosine form equation.

Both the following equations must be satisfied (I=1.0 and S≤1.0) to switch to the buckling strut behavior for a frame element.

I=1.0 (24)

S≤1.0 (25)

If the buckling strut response is requested for the element from the first step of the analysis, the member will be changed to a simply-supported member and the bending moments cannot be supported by the member. In this state, the ISO equation turns into the following simple equation.

$$P_{cr} = F_c A \quad and \quad f_c < F_c \quad (26)$$

6.1. Marshall Strut Envelope

The Marshall strut envelope defines the post-buckling damaged elasticity model and the hysteretic loop response [9]. To define the Marshall strut envelope, the value of P_{cr} and the following seven constants are needed:

ξ: is the coefficient defining $P_y = \xi\sigma^0 A$ ($\xi = 0.95$)

γ: is the isotropic hardening slope coefficient (0.02),

α_0: is the coefficient defining= $\alpha_0 + \alpha_1 \frac{L}{D}$

α_1: is the coefficient defining= $\alpha_0 + \alpha_1 \frac{L}{D}$, ($\alpha_0 = 0.03$) , ($\alpha_1 = 0.004$)

κ: is the force coefficient (0.28),

β: is the slope coefficient (0.02), and

ζ: is the force coefficient ($\min\left(1.0\,, 5.8\left(\frac{t}{D}\right)^{0.7}/\xi\right)$).

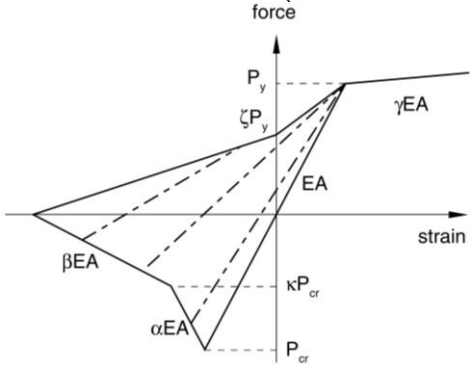

Figure 2. Marshall strut theory buckling envelope

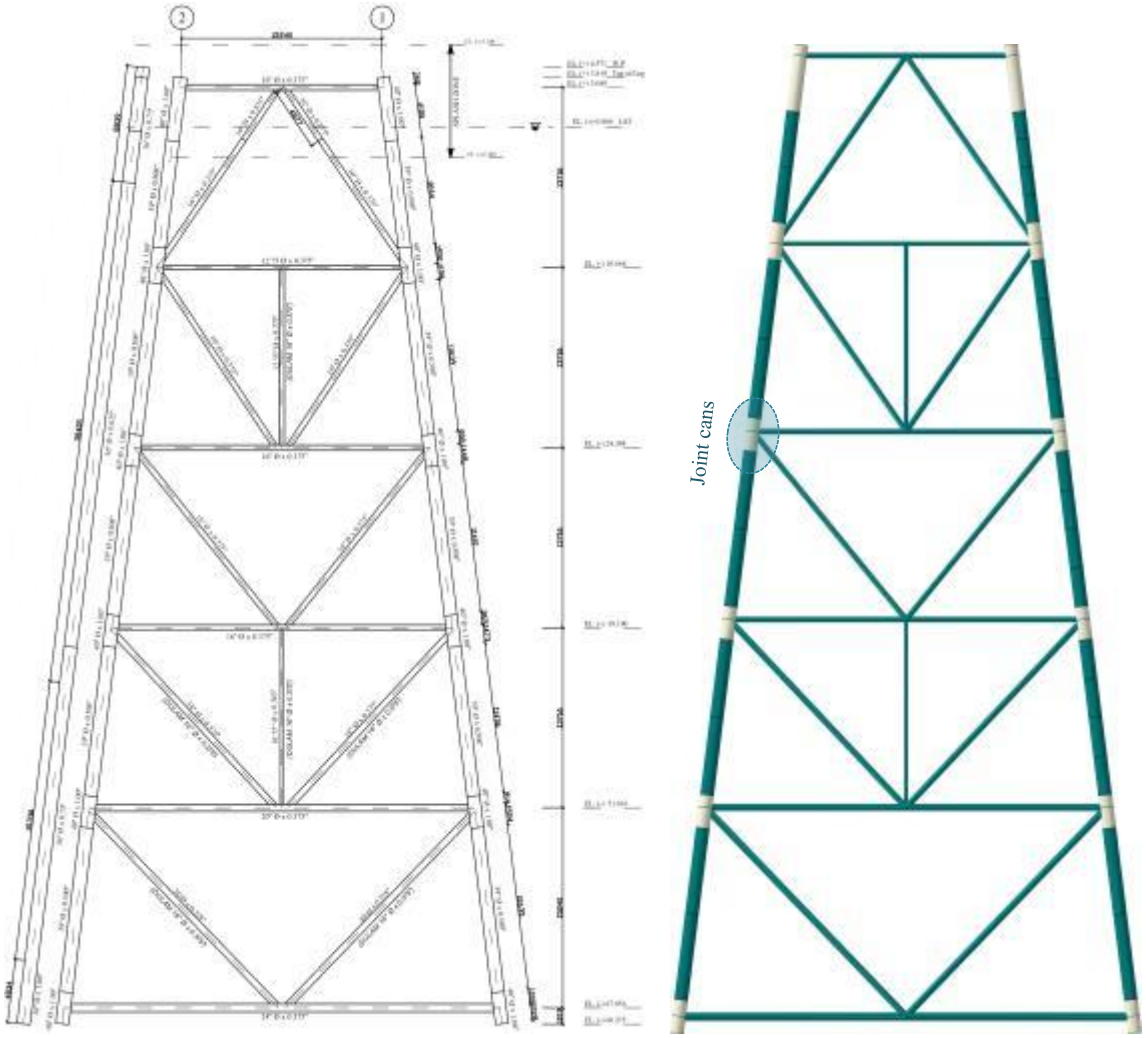

Figure 3. Schematic geometry of one row of Ressalat jacket and FE model

The values in parentheses are the default values supplied by ABAQUS, and the value of P_{cr} is found from the ISO equation as explained above. The Marshall envelope governs the compressive and tensile response of the strut as shown in Fig. 2. The dotted lines in the interior of the envelope indicate the damaged-elastic modulus defining the loading-unloading force versus strain path [10].

7. Modeling

A 3-Dimensional model of one frame of a four-leg Ressalat jacket platform of Persian Gulf has been performed. The schematic geometry and dimensions of the platform are shown in Fig. 3. All of the joint cans and the principal details have been taken into account in FE modeling.

Regarding to aspect ratios of sections used in the model, the maximum and minimum L/r ratio of the compressive braces are 126.01 and 118.63, respectively.

In this paper, the FE modeling of jacket is categorized into three main steps. On the first step, the jacket has been modeled using common two-node linear beam elements and 3D shell element both of which have been meshed with the common and traditional mesh size. The mesh size selected in this step is extensively applied in FE modeling of wide range of papers. Afterwards, in the second step the shell elements with optimized mesh size based on the previous studies of the authors [11,12,13,14], were replaced with the compressive braces of the platform. The mesh sizes applied in the second step can properly predict the buckling occurrence and post-buckling strength of braces. Changes in the structural behavior of the jacket have been considered at this step and represent below. Finally, in the third step all the braces have been replaced by two-node frame elements. The buckling behavior of each frame element has been achieved according to buckling behavior of respective brace model with 3D shell elements and Marshal strut envelope. Applying two-node frame elements conducts the models toward reducing the run time and costs of analysis. Pushover analysis has been executed as an approach to distinguish variations of results in different steps. The main deck has been simulated on the upper end of the piles in the form of a rigid connection between pile heads. Two concentrated masses have been applied on pile heads. Each of them has been assumed equal to 25% of the total mass of the platform deck, i.e. 2500 tones.

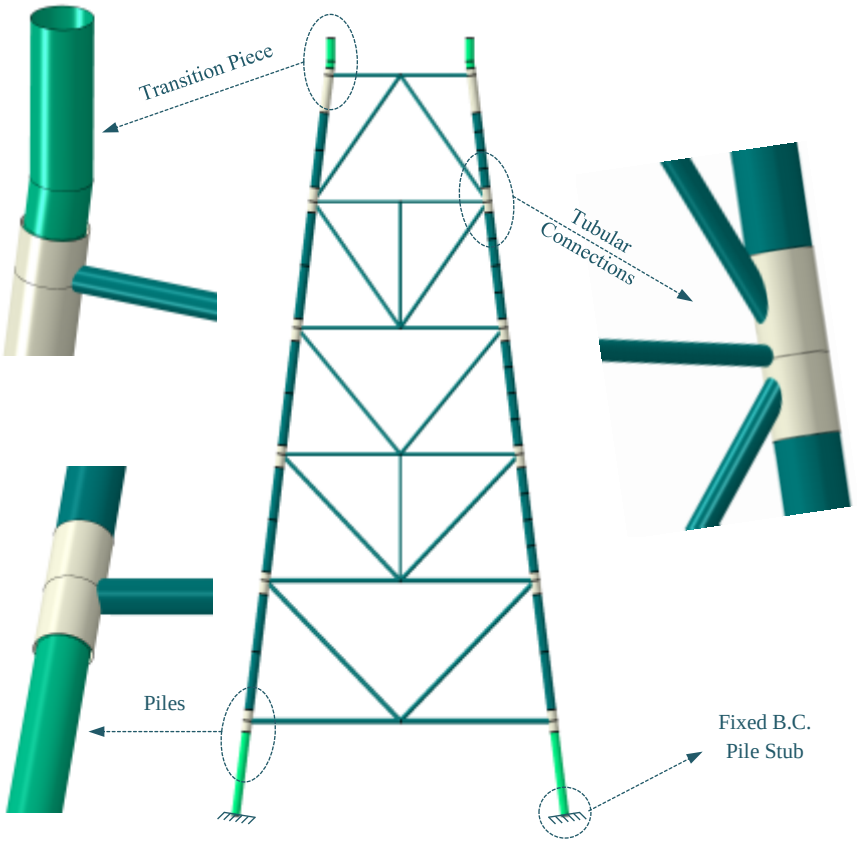

Figure 4. Model view of shell elements include global geometry of model, geometry of piles driven into legs, geometry of transition piece, and the geometry of one tubular connection

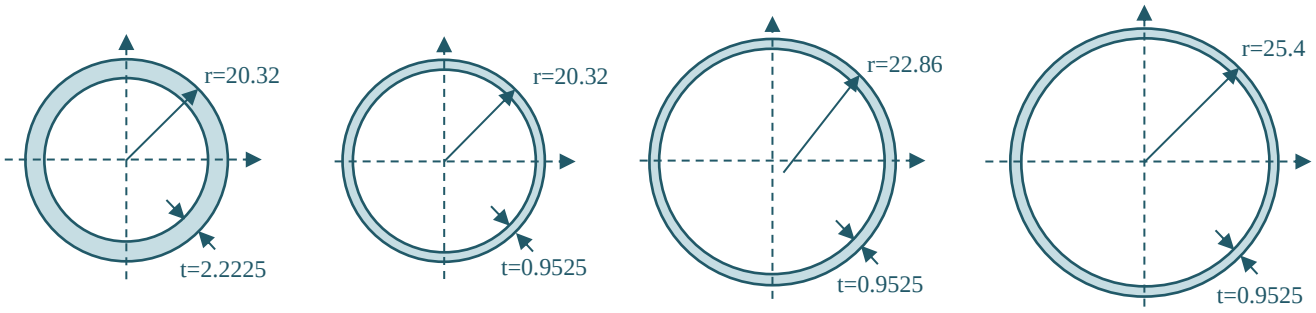

Figure 5. Geometry of all types of the frame elements cross-sections. All quantities have dimensions of cm.

Jackets and piles have been modeled separately and the cylindrical connection has been defined between them so that the piles can drive freely into the legs in rotational and translational degrees of freedom. In all the models, the pile stub technique has been used and the fixed end point of the piles has been set at a depth equal to 10 times its diameter. Fig. 4 shows the geometry modeled with shell elements.

The schematic view of all types of cross-section geometries defined for frame elements have been shown in Fig. 5.

8. Results

The critical buckling loads obtained from the numerical models with frame elements have been compared with the results of the ISO equation. Eventually, the most differences in all cases have been limited to 2 percent.

Failure due to elastic buckling of the member occurs prior to material yielding by increasing the length to radius of gyration ratio (L/r) in long members ($L/r > 100$). In long members the critical buckling force can be predicted by the Euler formula [15]:

$$P_{cr} = \frac{n\pi^2 EI}{Le^2} \quad (27)$$

For tubular members with intermediate length ($40 \leq L/r \leq 100$), the material reaches its limit of proportionality at the outer fiber of the member leading to a reduction in stiffness and kneeling of the section. So, the Euler formula overestimates critical buckling force. Fig. 6 displays a comparison between the typical elastic and inelastic buckling shapes. Also this figure demonstrates the variation of critical buckling load versus column slenderness parameter, λ.

In short braces ($L/r < 40$), the section may meets the yielding before occurrence of buckling.

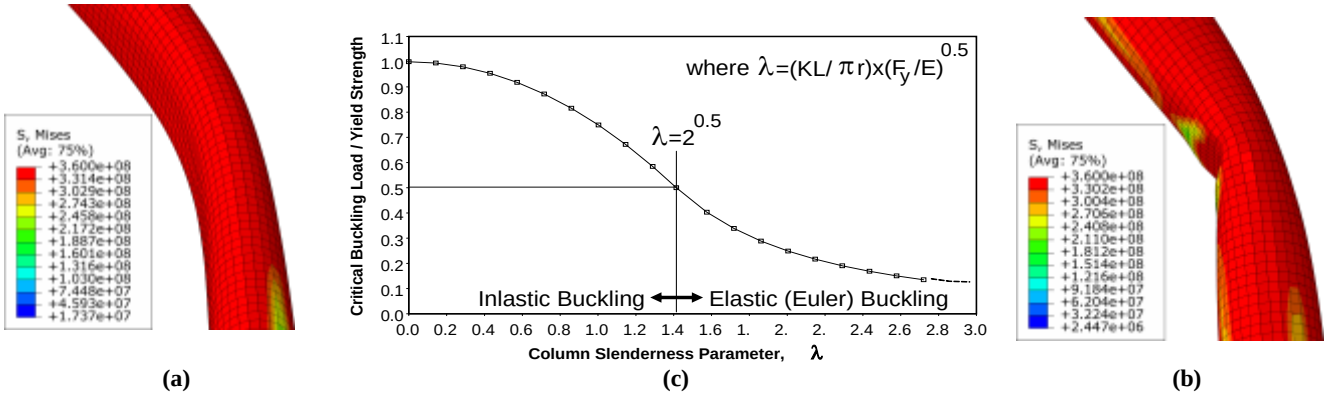

Figure 6. A sample of comparison between elastic and inelastic buckling shape; (a) Elastic buckling (long braces) (b) Inelastic buckling/kneeling (intermediate/short braces) (c) The critical buckling load versus column slenderness parameter

In these members the buckling shape will be similar to the elements with moderate length. However, in short members a larger area around the buckled section meets the yield level.

By increasing the D/t ratio the flexural stiffness of shell wall decreases with a power of 3 [5]. After occurrence of the buckling, the shell walls start to swing and ultimately the member bends. Local flexural moments due to deformation of the shell wall quickly result a local plastic zone. Finally, the local buckling which reduces the capacity of member leads to global buckling.

Increasing the L/r ratio results in further plastic zone and fewer critical buckling load. The enlarged plastic area causes a sudden collapse if the local buckling occurs in this state [5].

Fig. 7 and Fig. 8 present the results of the pushover analysis performed on the three separate steps explained before. In Fig. 7 the distribution of lateral displacement which defined in FE model is triangular and has ascending order in height with a maximum displacement of 3 m in the main deck. While Fig. 8 illustrates the results of pushover analyzes with a point-centered lateral displacement of 3 m at the level of main deck. Both of distributions are in accordance with pictures shown in Fig. 1.

The order of buckling occurrence in braces is displayed in the Fig. 7. The buckling of the compressive brace positioned at the lowest level of the jacket causes immediate drop and severe loses of global capacity throughout the structure. The buckling of this brace has not been observed when proper mesh has been assigned to all braces. Therefore, a sharp drop in pushover capacity curve has not occurred in models with proper mesh and models contain frame elements. According to the Fig. 7 applying improper mesh size for compressive members can under-predict the ductility by 33% and under-estimate the lateral loading capacity up to 8%. Each of the braces in model with typical and inappropriate mesh, buckled earlier than model with proper mesh.

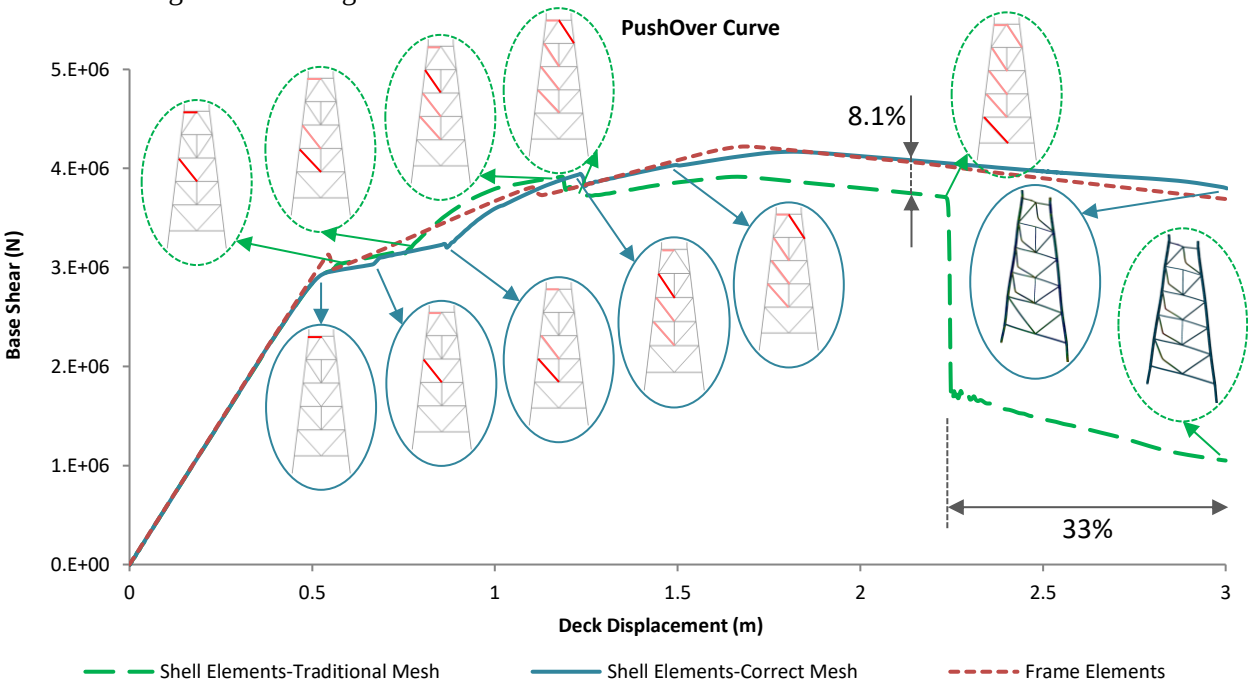

Figure 7. Results of pushover analysis of models with frame and shell elements for push distribution type 1

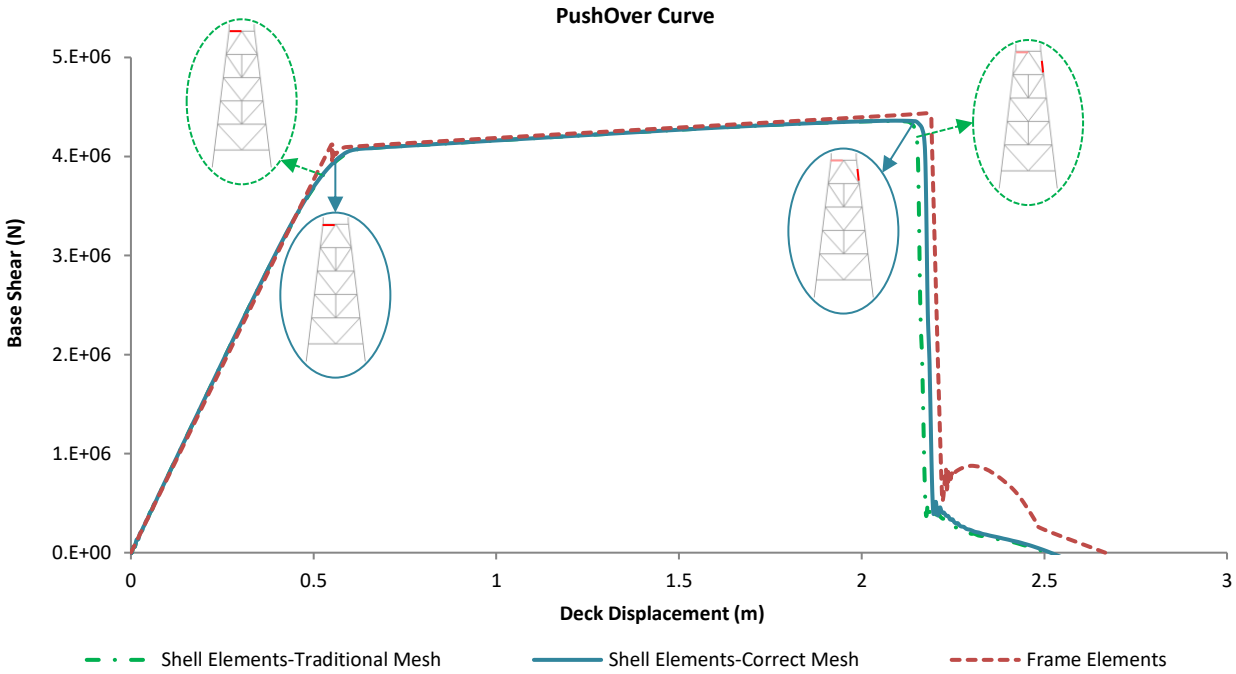

Figure 8. Results of pushover analysis of models with frame and shell elements for push distribution type 2

As seen in Fig. 8 the point-centered lateral push of jacket, did not actuate the compressive capacity of braces and no buckling can be seen in the braces of jacket. Finally, only damage occurrence in the pile at top level causes immediate resistance loss and global collapse of the structural. Also at this distribution the frame elements can properly consider the buckling capacity of braces due to investigation of the effects of local buckling along with global buckling. Besides that utilization of frame element can significantly decreases the time and cost of analysis and modeling.

9. Conclusions

It is proved that the frame elements consider interaction of local and global buckling using ISO equation and Marshall's buckling theory that is described in detail in the paper. However based on the results obtained from the models, it is possible that frame elements do not provide accurate prediction of buckling and post-buckling behavior of structures by incorrect estimation of various parameters of Marshal's curve. It should be noted that the use of frame elements greatly reduces the analysis costs than those using shell elements. On the other side, applying proper mesh in structural FE modeling of jackets with 3D shell or solid elements will affect the accuracy of the estimation of capacity curve including two important items of ultimate lateral bearing and ductility and finally the structural performance levels derived from this curve. Number of mesh elements on section and the ratio of element size along the member length to section are two fundamental parameters in modeling of compressive members with 3D shell elements. Improper determination of these values for braces of jacket could under-predict the ductility by 33% and under-estimate the lateral loading capacity up to 8%. But due to damage occurrence in piles, the behaviors of jackets with different mesh size are almost the same when the lateral push of the structure concentrated on the level of main deck.

List of Symbols

D	outer diameter
t	wall thickness of pipe
P	axial force
σ^0	yield stress
E	Young's modulus of elasticity
A	cross-sectional area
Z_e	elastic section modulus
k_1, k_2	effective length factors in the 1 and 2 directions
Z_p	plastic section modulus
L_1, L_2	unbraced lengths for the 1 and 2 directions
r	radius of gyration
I_{11}, I_{22}	bending moment of inertia in 1 and 2 directions

10. References

1- Karamanos, S.A., Tassoulas, J.L., (1996), *Tubular members II: local buckling and experimental verification*, Journal of engineering mechanics, 122(1), p. 72-78.

2- Sadowski, A.J., Rotter, J.M., (2013), *solid or shell finite elements to model thick cylindrical tubes and shells under global bending*, International journal of mechanical sciences, 74, pp.143-153.

3- Bardi, F.C., Kyriakides, S., (2006), *Plastic buckling of circular tubes under axial compression—part I:*

experiments, International journal of mechanical sciences, 48(8), pp.830-841.

4- Bardi, F.C., Kyriakides, S., Yun, H.D., (2006), *Plastic buckling of circular tubes under axial compression—part II: analysis*, International journal of mechanical sciences, 48(8), pp.842-854.

5- Yasseri, S., Skinner, K., Styles, D., (2006), *Post buckling response study for high D/t tubular members*, Technical report.

6- Xia, W. and Hoogenboom, P.C.J., (2011), *Buckling analysis of offshore jackets in removal operations*, ASME 2011 30th International Conference on Ocean, Offshore and Arctic Engineering (pp. 449-454), American Society of Mechanical Engineers.

7- Fernando, P., Rodrigues, N., Jacob, BP., (2005), *Collapse analysis of steel jacket structures for offshore oil exploitation*, Journal of constructional steel research, 61.

8- (2007), *ISO 19902*, International Standard: Petroleum and natural gas industries-fixed steel offshore structures, First edition.

9- Marshall, P.W., (1992), *Design of welded tubular connections, basis and use of AWS code provisions*, Elsevier.

10- Simulia, D.S. (Dassault Systèmes), (2012), *Abaqus 6.12 documentation*, Providence, Rhode Island, US, 261.

11- Tabeshpour, M.R., Erfani, M.H., Sayyadi, H., (2016), *Study on ultimate capacity of offshore jacket platforms by using beam elements, considering the effects of global and local buckling of the elements*, 18th international conference of marine industries (MIC2016), Kish Island.

12- Tabeshpour, M.R., Erfani, M.H. and Sayyaadi, H., (2019), *Challenges in calculation of critical buckling load of tubular members of jacket platforms in finite element modeling*, Journal of marine science and technology, pp.1-21.

13- Tabeshpour, M.R., Erfani, M.H. and Sayyadi, H., (2019), *Study on ultimate capacity of offshore jacket platforms considering the effects of general and local buckling of the elements*, Advances in Solid and Fluid Mechanics., 1(1), pp.9-17.

14- Tabeshpour, M.R., Erfani, M.H. and Sayyadi, H., (2018), *Investigation of uncertainties in buckling and post-buckling behavior of typical braces of offshore jacket platforms by using solid elements in ABAQUS*, 20th international conference of marine industries (MIC2018), Tehran.

15- Su, R.K. and Wang, L., (2015), *Flexural and axial strengthening of preloaded concrete columns under large eccentric loads by flat and precambered steel plates*, Structure and infrastructure engineering, 11(8), pp.1083-1101.